






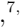



A Wideband Chemical Survey of Massive Star-forming Regions at Subarcsecond Resolution with the Submillimeter Array

CHARLES J. LAW ^{1,*} QIZHOU ZHANG ² ARIELLE C. FROMMER ² KARIN I. ÖBERG ²
ROBERTO GALVÁN-MADRID ³ ERIC KETO² HAUYU BAOBAB LIU ^{4,5} PAUL T. P. HO ⁶
ANDRÉS F. IZQUIERDO ^{7,8,9,*} AND L. ILSEDORE CLEEVES ¹

¹*Department of Astronomy, University of Virginia, Charlottesville, VA 22904, USA*

²*Center for Astrophysics | Harvard & Smithsonian, 60 Garden St., Cambridge, MA 02138, USA*

³*Instituto de Radioastronomía y Astrofísica, Universidad Nacional Autónoma de México, Morelia, Michoacán 58089, México*

⁴*Department of Physics, National Sun Yat-Sen University, No. 70, Lien-Hai Road, Kaohsiung City 80424, Taiwan, R.O.C.*

⁵*Center of Astronomy and Gravitation, National Taiwan Normal University, Taipei 116, Taiwan*

⁶*Institute of Astronomy and Astrophysics, Academia Sinica, 11F of Astronomy–Mathematics Building, AS/NTU No. 1, Sec. 4, Roosevelt Rd., Taipei 10617, Taiwan, R.O.C.*

⁷*European Southern Observatory, Karl-Schwarzschild-Straße 2, 85748 Garching bei München, Germany*

⁸*Leiden Observatory, Leiden University, 2300 RA Leiden, The Netherlands*

⁹*Department of Astronomy, University of Florida, Gainesville, FL 32611, USA*

ABSTRACT

Massive star-forming regions exhibit a rich chemistry with complex gas distributions, especially on small scales. While surveys have yielded constraints on typical gas conditions, they often have coarse spatial resolution and limited bandwidths. Thus, to establish an interpretative framework for these efforts, detailed observations that simultaneously provide high sensitivity, spatial resolution, and large bandwidths for a subset of diverse sources are needed. Here, we present wideband (≈ 32 GHz) Submillimeter Array observations of four high-mass star-forming regions (G28.20-0.05, G20.08-0.14 N, G35.58-0.03, W33 Main) at subarcsecond resolution, where we detect and spatially-resolve 100s of lines from over 60 molecules, including many complex organic molecules (COMs). The chemical richness of our sample is consistent with an evolutionary sequence from the line-rich hot cores and HC H II regions of G28.20-0.05 and G20.08-0.14 N to the more chemically-modest UC H II regions in G35.58-0.03, followed by the molecule-poor H II region W33 Main. We detect lines across a range of excitation conditions ($E_u \approx 20$ to $\gtrsim 800$ K) and from numerous isotopologues, which enables robust estimates of gas properties. We derive nearly constant COM column density ratios that agree with literature values in other low- and high-mass protostellar cores, supporting the idea that COM abundances are set during the pre-stellar phase. In all regions, we identify spatial offsets among different molecular families, due to a combination of source physical structure and chemistry. In particular, we find potential evidence of carbon grain sublimation in G28.20-0.05 and identify an elemental oxygen gradient and rich sulfur-chemistry in G35.58-0.03. Overall, these results demonstrate that the SMA’s wide bandwidth is a powerful tool to untangle the complex molecular gas structures associated with massive star formation.

Keywords: Young stellar objects (1834) — Star forming regions (1565) — Interstellar molecules (849)
— High angular resolution (2167) — Complex organic molecules (2256)

1. INTRODUCTION

The formation of massive stars ($>8 M_\odot$) remains poorly understood due, in large part, to a variety of observational challenges, including their relative rarity, obscured nature, high gas optical depths, fast evolutionary

Corresponding author: Charles J. Law
cjl8rd@virginia.edu

* NASA Hubble Fellowship Program Sagan Fellow

timescales, and large distances (several to tens of kpcs) compared to their low-mass counterparts (e.g., [Beuther et al. 2007](#); [Tan et al. 2014](#); [Motte et al. 2018](#)). Classically, a massive young stellar object (MYSO) is formed via gravitational collapse, which is then followed by the appearance of a compact, dense, and hot molecular core (HMC) (e.g., [Kurtz et al. 2000](#)). These cores then continue to evolve into hypercompact (HC) H II regions with electron densities of $\sim 10^6 \text{ cm}^{-3}$ and sizes of $< 0.05 \text{ pc}$ (e.g., [Hoare et al. 2007](#)) and then into ultracompact (UC) H II regions with electron densities of $\sim 10^4 \text{ cm}^{-3}$ and sizes of $\sim 0.1 \text{ pc}$ as the UV radiation from the massive central star breaks out into the nearby environment. Ultimately, continued expansion will result in a fully-fledged H II region, before the surrounding material is destroyed or dispersed by powerful stellar winds (e.g., [Kurtz et al. 2000](#); [Churchwell 2002](#)). However, in reality, the separation of these stages is not distinct and instead, several of these phases often exist at the same time within one region as multiple massive young stars are being formed in close proximity (e.g., [Motte et al. 2022](#)).

The emergence of young H II regions is marked by bright infrared emission (e.g., [Csengeri et al. 2017](#)), a variety of molecular masers (e.g., [Genzel & Downes 1977](#); [Menten 1991](#); [Argon et al. 2000](#)), and broad (FWHM $\gtrsim 40 \text{ km s}^{-1}$) radio recombination lines (RRLs) from ionized gas (e.g., [Sewilo et al. 2004](#); [Keto et al. 2008](#); [Sewilo et al. 2011](#)). Hot cores trace individual massive protostars or low-order multiples and are identified via emission from complex organic molecules (COMs), which are either direct products of sublimated ice grain mantles or formed via gas-phase reactions (e.g., [Herbst & van Dishoeck 2009](#)). Given the multi-component and hierarchical nature of most massive star formation, warm (few 100 K) molecular gas and hot ($\sim 10^4 \text{ K}$) ionized gas co-exist in relatively small regions. This often results in dynamical interactions between the two, e.g., in the form of smaller-scale outflows in ionized gas driving larger-scale molecular outflows. On the smallest scales, observational evidence now exists that massive protostars host Keplerian accretion disks in either molecular (e.g., [Ilee et al. 2018](#); [Sanna et al. 2019](#); [Lu et al. 2022](#)) or ionized gas ([Maud et al. 2018](#); [Jiménez-Serra et al. 2020](#); [Galván-Madrid et al. 2023](#)) depending on the mass of the central object.

The chemical complexity associated with massive star-forming regions thus provides an opportunity to directly trace the underlying physical gas conditions. However, this, in turn, requires: high angular resolution to localize distinct but contemporaneous evolutionary phases within a single star-forming region; fine velocity resolu-

tion to separate multiple gas kinematic components; and sufficiently large bandwidth to cover multiple molecular tracers and transitions across a wide range of excitation conditions to constrain gas physical conditions. Due to high gas densities, many commonly-observed dense gas tracers are optically thick, and it is thus also vital to simultaneously observe multiple isotopologues.

Only with such observations is it possible to confront a variety of outstanding questions, namely, what is the origin and frequency of spatial offsets between molecules of different chemical families (e.g., [Blake et al. 1987](#); [Wyrowski et al. 1999](#); [Allen et al. 2017](#); [Tercero et al. 2018](#); [Busch et al. 2022](#); [Mininni et al. 2023](#))? What types of molecules serve as the best tracers for gas physical conditions, e.g., UV fields, temperature, density, the presence of shocks (e.g., [van Gelder et al. 2022](#); [Brouillet et al. 2022](#))? How are hot cores related to the HC and UC H II region evolutionary phases and how does the presence of nearby H II regions influence hot core chemistry, e.g., via external heating (e.g., [Blake et al. 1996](#); [Zapata et al. 2011](#); [Wilkins et al. 2022](#))? Which types of COM chemistry are driven by ice sublimation versus gas-phase formation (e.g., [Garrod et al. 2008](#); [Codella et al. 2017](#); [van 't Hoff et al. 2020](#)); and how should recent observations of constant COM abundance ratios across a wide range of sources from pre-stellar cores to high-mass protostars be interpreted, e.g., is pre-stellar ice chemistry largely dominant in COM production ([Scibelli et al. 2021](#); [Nazari et al. 2022](#); [Chen et al. 2023](#))?

With these questions in mind, we present initial results from a wideband chemical survey of four massive star-forming regions at subarcsecond resolution with the Submillimeter Array (SMA). Overall, we detect and spatially-resolve 100s of lines from over 60 molecules, including multiple COMs and isotopologues. In Section 2, we briefly describe the properties of the four star-forming regions that comprise our survey and summarize the SMA observations in Section 3. In Section 4, we present our results, including line detection statistics, maps of molecular gas morphologies, and derived gas properties. In Section 5, we discuss the origins of the observed emission, including spatial variations of gas conditions, COM abundance ratios, and how our sources compare to other low- and high-mass protostars. We summarize our conclusions in Section 6.

2. SOURCE DESCRIPTION

Our survey targeted four massive star-forming regions within $\approx 12 \text{ kpc}$ with significant reservoirs of molecular gas and bolometric luminosities of a few-to-several times $10^5 L_{\odot}$. Our sources also span a range of evolutionary stages from young hot cores and HC H II regions to

more evolved H II regions. Table 1 provides a summary of source properties. Below, we briefly describe each of the sources:

G28.20-0.05 (hereafter ‘G28’): G28 is an HC H II at a distance of 5.7 kpc (Fish et al. 2003; Law et al. 2022) surrounded by an infalling molecular gas torus with a central ionized core and an expanding shell of molecular gas driven by a wide-angle outflow (Sollins et al. 2005a; Klaassen et al. 2009, 2011). Recent high-resolution ALMA observations show that G28 takes the form of a ring of ionized gas with a radius of ≈ 2000 au, while H30 α kinematics indicate the presence of a rotating, ionized disk wind launched by the central massive protostar (Law et al. 2022). This ionized disk wind is driving a larger-scale molecular outflow observed in SiO emission along the NE-SW direction out to a distance of ~ 0.2 pc (Gorai et al. 2024). G28 appears to be forming in an isolated environment with no additional protostellar cores identified in its vicinity (~ 0.1 to 0.4 pc) (Law et al. 2022). G28 has also been detected in several RRLs with broad line widths (Sewilo et al. 2004; Keto et al. 2008; Sewilo et al. 2008) and in multiple molecular masers (Menten 1991; Han et al. 1998; Argon et al. 2000), indicating its relative youth. A variety of hot-core-tracing molecules were observed toward G28 in early SMA observations (Qin et al. 2008), and the presence of complex molecular gas distributions, including emission from COMs, was confirmed in subsequent ALMA observations (Gorai et al. 2024). In particular, Gorai et al. (2024) identified at least two distinct hot molecular cores (HMC1, HMC2) with high gas densities ($n_{\text{H}} \sim 10^9 \text{ cm}^{-3}$) and inferred excitation temperatures of ≈ 270 -300 K. HMC1 is located along the millimeter continuum ring and is thought to be closest in projection to the protostar, while HMC2, located on the other side of the ring, instead traces an externally-heated concentration of molecular gas (Gorai et al. 2024).

G20.08-0.14 N (hereafter ‘G20’): G20 is a proto-OB-cluster at a distance of 12.3 kpc (Fish et al. 2003; Anderson & Bania 2009) comprising one UC H II and two HC H II regions first identified in cm observations (Wood & Churchwell 1989). Molecular masers (Ho et al. 1983; Hofner & Churchwell 1996; Walsh et al. 1998) and broad-line RRLs (Garay et al. 1985; Sewilo et al. 2004) have been detected toward G20. These UC H II and HC H II regions are surrounded by dense molecular gas (Plume et al. 1992; Galván-Madrid et al. 2009) and are embedded within a rotating and contracting molecular cloud (e.g., Klaassen & Wilson 2007). A hierarchical accretion flow that extends from parsec-scales down onto the individual UC H II and HC H II regions has also been identified (Galván-Madrid et al. 2009). Emission

from several hot core molecules is present in the brightest of these H II regions (region ‘A’ in Galván-Madrid et al. 2009) and likely traces photoevaporation at the inner edge of a rotationally-flattened molecular accretion flow (Galván-Madrid et al. 2009; Xu & Wang 2013). There is also evidence of a collimated SiO outflow along the north-east to south-west direction that is centered at this bright H II region (Xu & Wang 2013). No molecular line emission was detected around the other two H II regions (regions ‘B’ and ‘C’ in Galván-Madrid et al. 2009).

G35.58-0.03 (hereafter ‘G35’): G35 is a high-mass star-forming region at a distance of 10.2 kpc (Fish et al. 2003; Watson et al. 2003) that consists of two closely separated ($\sim 1''$) UC H II regions, the western G35.578-0.030 and eastern G35.578-0.031, identified in cm observations (Kurtz et al. 1994). For simplicity, we subsequently refer to these UC H II regions as ‘G35 West’ and ‘G35 East’, respectively. Water and OH masers have been detected in G35 (Forster & Caswell 1989; De Buizer et al. 2005; Fish et al. 2005) along with emission from broad-line RRLs (Zhang et al. 2014). There is a thick dust and infalling gas envelope surrounding the central UC H II regions in G35 (Kurtz et al. 1999; Zhang et al. 2014). Previous H30 α observations also indicate the presence of an ionized outflow, which, in turn, is driving a collimated, bipolar molecular outflow along the east-west direction. The mass-loss rate associated with this outflow is nearly an order of magnitude less than that of the infall rate, which implies that the mass of the central proto-O-star is still increasing (Zhang et al. 2014). Previous SMA observations, which did not resolve the two central UC H II regions, detected several hot-core-tracing molecules in G35 (Zhang et al. 2014).

W33 Main (hereafter ‘W33’; also G012.81-0.19): W33 Main is one of three molecular clumps in the larger W33 complex (e.g., Schuller et al. 2009; Immer et al. 2014; Lin et al. 2016), which was first discovered as a thermal radio source (Westerhout 1958) and is located at a distance of 2.4 kpc in the Scutum spiral arm of the Galaxy (Immer et al. 2013). Water, methanol, and ammonia masers have been detected in W33 Main (e.g., Genzel & Downes 1977; Menten et al. 1986; Haschick et al. 1990; Immer et al. 2013; Tursun et al. 2022) along with bright infrared emission (e.g., Dyck & Simon 1977; Molinari et al. 2010), indicating the presence of a cluster of proto-OB stars. Several star clusters are located near W33 Main (Morales et al. 2013) and it is the only source in the W33 complex to show strong radio continuum (Haschick & Ho 1983; Hoare et al. 2012; Khan et al. 2022), which indicates that it is an evolved H II region. Sub-millimeter observations revealed a compact continuum source (Contreras et al. 2013), which was later re-

solved into a U-shaped feature (‘W33 Main-Central’ in Immer et al. 2014) along with several additional nearby cores (Immer et al. 2014; Armante et al. 2024). Emission from SiO and H3O α is only detected toward W33 Main, but none is observed from complex molecules, unlike other nearby regions within the W33 region (Immer et al. 2014). This relative lack of emission from hot-core-tracing molecules is likely due to their destruction close to the central heating source(s) in W33 Main (Immer et al. 2014).

3. OBSERVATIONS

We observed each of the four massive star-forming regions with the SMA¹ (Ho et al. 2004) using both the compact (COM) and very extended (VEX) array configurations between 12 March 2019 and 27 August 2019. The COM observations had typical baselines of ≈ 70 m, while the VEX configuration had baselines of ≈ 500 m. For those sources in the COM configuration observed on the same night, observing time was split equally between them. Table 2 shows a summary of the observations, including observing dates, SMA configuration, number of available antennas, and PWV.

All observations used both the 230 GHz and 345 GHz receivers with the SWARM correlator, which at the time, provided a total frequency coverage of 32 GHz. The two sidebands of the lower frequency receiver covered 208.948–216.910 GHz and 224.944–232.907 GHz, while the higher frequency receiver was tuned to cover 332.908–340.870 GHz and 348.906–356.868 GHz. The native spectral resolution of the observations was 140 kHz (≈ 0.12 – 0.20 km s⁻¹), but to reduce data volume, we binned by a factor of four for initial calibration and reduction, followed by a further smoothing to a uniform velocity resolution of 1.12 km s⁻¹ during imaging.

We calibrated the SMA data using the MIR software package². Passband calibrations were performed using observations of the bright quasars 3C279 or 3C84. Depending on the source and observation, gain calibration was achieved using one or more of the following quasars 1743-038, 1751+096, and nrao530, while flux calibrators included Callisto, Ganymede, Neptune, and Titan. Table 2 shows a detailed listing of all calibrators.

The calibrated visibilities were then exported into CASA v6.3 (McMullin et al. 2007; CASA Team et al. 2022) for continuum subtraction and imaging. For all sources, line-free channels were manually identified and we subtracted the continuum using the `uvcontsub` task with a first-order polynomial. We then used the `tclean` task with a Briggs weighting of `robust=0.5` to generate images. Each 8 GHz spectral window was imaged individually. Images were generated with channel spacings of 1.12 km s⁻¹ to maximize SNR but ensure line profiles were sufficiently well-resolved. All images were made using the ‘multi-scale’ deconvolver with pixel scales of [0,8,24,40,100,300] and were CLEANed down to a 3σ level, where σ was measured over five line-free channels of the dirty image. We also made 230 GHz and 345 GHz continuum images with the full bandwidth of the observations after flagging channels containing line emission using the same CLEANing parameters. Table 3 lists image cube properties for each source per sideband, including the synthesized beam size and measured RMS noise.

Due to the range of on-source observing times, number of available antennas, weather conditions, and observed frequencies, image cubes exhibited a range of properties. Synthesized beam sizes range from $0''.5$ to over $2''$, which corresponds to physical scales of ≈ 2000 – 3000 au in G28, ≈ 5000 – 6000 au in W33, and $\approx 10,000$ – $20,000$ au in G20 and G35. The line RMS noise values are between 23 mJy beam⁻¹ and 455 mJy beam⁻¹. In particular, the high frequency image cubes of G20 have considerably coarser beam sizes than those of the lower frequencies, since several antennas associated with the 345 GHz receiver were flagged during calibration due to unstable phases during the VEX observations. W33 suffers from spatial filtering even in the combined COM+VEX data due its close distance and the extended nature of its emission ($\gtrsim 10''$) (e.g., Immer et al. 2014). It is also the southernmost source in our sample, which resulted in an elongated beam shape. While we initially explored a range of `robust` values and *uv*-tapers in the CLEANing of W33 image cubes, we did not find any significant differences in either the line detection statistics or emission morphology. Thus, for consistency, we decided to adopt the same imaging parameters as for the other sources and instead smoothed all line image cubes of W33 using `imsmooth` with a circular beam of $2''$ to boost low SNR line detections. The continuum images and continuum-subtracted line emission image cubes as well as the calibrated measurement sets for all sources are publicly available on Zenodo doi: 10.5281/zenodo.13342640.

¹ The Submillimeter Array is a joint project between the Smithsonian Astrophysical Observatory and the Academia Sinica Institute of Astronomy and Astrophysics and is funded by the Smithsonian Institution and the Academia Sinica.

² <https://lweb.cfa.harvard.edu/~cqi/mircook.html>

Table 1. Source Properties

Source	dist.	D_{GC}	v_{sys}	L_{bol}	M_*	$M_{env,gas}$	Region
	(kpc)	(kpc)	(km s^{-1})	(L_{\odot})	(M_{\odot})	(M_{\odot})	Type
G28.20-0.05	$5.7^{+0.5}_{-0.8}$ [1]	4.6 [1]	95.4 [2]	1.4×10^5 [3]	40 [3]	25 [4]	HC H II+HMC [4,5]
G20.08-0.14 N	$12.3^{+0.7}_{-1.2}$ [1]	5.3 [1]	42.0 [6]	6.6×10^5 [6,7]	34 [6]	35–95 [6]	UC+HC H II [7]
G35.58-0.03	$10.2^{+0.6}_{-0.6}$ [8]	6.0 [9]	52.5 [8]	$2.9\text{--}8.4 \times 10^5$ [10]	24–64 [10]	277–441 [10]	UC H II [9]
W33 Main	$2.4^{+0.17}_{-0.15}$ [11]	5.4 [11]	34.1 [11]	4.5×10^5 [12]	189 [13]	3965 [12]	H II [14]

NOTE—References are: 1. Fish et al. (2003); 2. Qin et al. (2008); 3. Law et al. (2022); 4. Gorai et al. (2024); 5. Walsh et al. (2003); 6. Galván-Madrid et al. (2009); 7. Wood & Churchwell (1989); 8. Watson et al. (2003); 9. Kurtz et al. (1994); 10. Liu et al. (2019a); 11. Immer et al. (2013); 12. Immer et al. (2014); 13. Beilis et al. (2022); 14. Haschick & Ho (1983).

Distances were derived from H I and H₂CO absorption studies in all sources except W33, which instead was computed via trigonometric parallaxes of water masers. Systemic velocities were measured using observed molecular lines. For all regions, bolometric luminosities were inferred from SED modeling, as were stellar masses with the exception of W33, where M_* was derived via detailed 3D hydrodynamic and line profile simulations of [Ne II] emission line data. Envelope masses were estimated from the dust emission in each region by assuming a gas-to-dust ratio of 100, with the exception of G35, where the reported $M_{env,gas}$ values correspond to the range predicted by the five best-fit radiative transfer SED models.

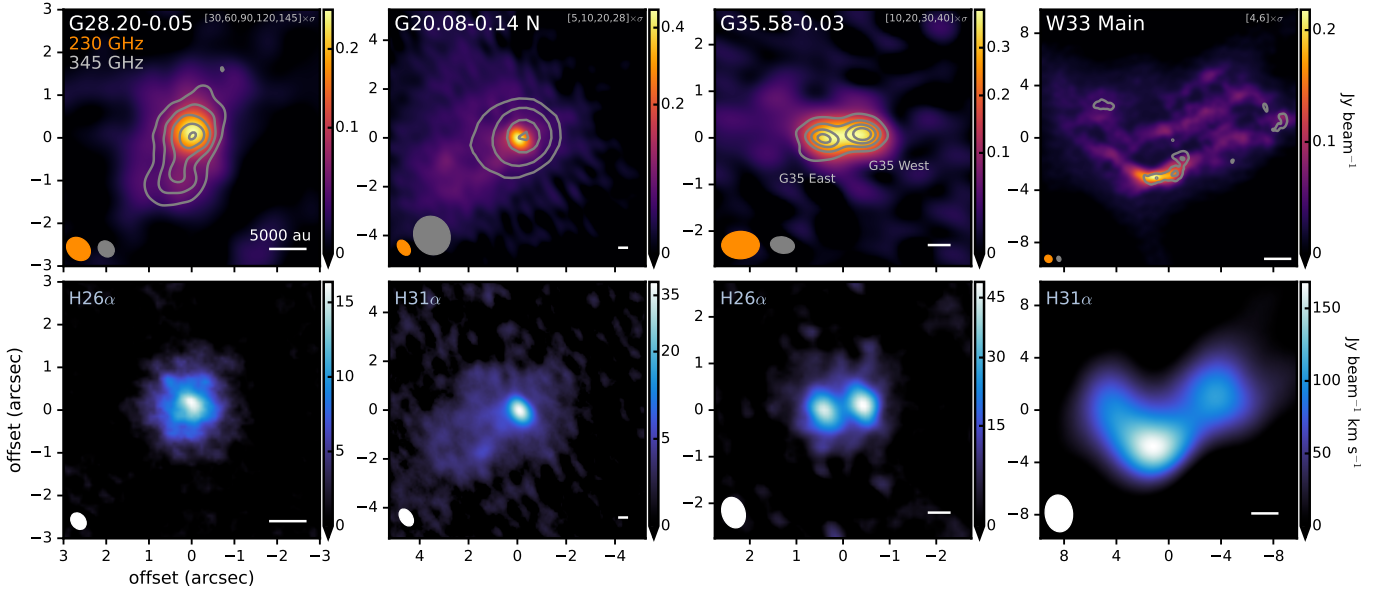


Figure 1. Gallery of continuum images (*top row*) and RRL integrated-intensity maps (*bottom row*) for the SMA sample. Colorscale shows the 230 GHz continuum and gray contours show the 345 GHz continuum. The synthesized beam and a scale bar indicating 5000 au is shown in the lower left and right corner, respectively, of each panel.

4. RESULTS

4.1. Continuum and RRL Morphology

All of our sources show strong emission from multiple RRLs, including H α , H β , and H γ , while lines of H δ and He α were detected in at least two sources. These

RRLs trace ionized gas and thus, the spatial distribution of RRL emission provides useful context for where the strongest radiation fields and hottest gas are located when later interpreting observations of the molecular gas.

Figure 1 shows continuum and H α integrated-intensity maps in our sample. We choose the particular RRL which has the highest angular resolution (H26 α in G28

Table 2. Observational Details

Source	R.A.	Dec.	UT Date	Num.	SMA	$\tau_{225\text{GHz}}$	Calibrators		
	(J2000)	(J2000)		Ant. ^a			config.	(mm)	Flux
G28.20-0.05	18:42:58.10	−04:13:57.87	2019 Apr 25	6	COM	0.07	Callisto	3C279	1743-038,1751+096
			2019 Apr 26	7	COM	0.06	Callisto	3C279	1743-038,1751+096
			2019 Mar 12	8	VEX	0.06	Ganymede	3C279	1743-038,1751+096
			2019 Jun 15	8	VEX	0.10	Callisto	3C279	1743-038,1751+096
G20.08-0.14 N	18:28:10.40	−11:28:49.00	2019 Apr 19	7	COM	0.04	Callisto	3C279	1743-038
			2019 Jun 14	8 ^b	VEX	0.07	Titan	3C279	1743-038,nrao530
G35.58-0.03	18:56:22.53	+02:20:27.00	2019 Apr 25	6	COM	0.07	Callisto	3C279	1743-038,1751+096
			2019 Aug 27	8	COM	0.09	Neptune	3C84	1743-038,1751+096
			2019 Mar 18	8	VEX	0.06	Callisto	3C279	1743-038,1751+096
W33 Main	18:14:13.67	−17:55:40.00	2019 Apr 19	7	COM	0.04	Callisto	3C279	1743-038
			2019 Mar 15	8	VEX	0.04	Callisto	3C279	1743-038,nrao530

^aNumber of antennas remaining after flagging.

^bAn additional three antennas were flagged due to unstable phases in the 345 GHz receiver. This resulted in correspondingly degraded angular resolution in the final images (see Table 3).

and G35; H31 α in G20 and W33). In all cases, the continuum and RRLs have broadly similar emission morphologies, which is consistent with a significant fraction of the continuum emission originating from free-free emission. Given the powerful outflows present in these regions, a portion of this free-free emission may also originate from ionized jets (e.g., Purser et al. 2016). Free-free contributions to the total 1.3 mm flux in our sample have been previously estimated to range from $\sim 25\%$ to 80% depending on the particular source (e.g., Galván-Madrid et al. 2009; Zhang et al. 2014; Immer et al. 2014; Law et al. 2022; Armante et al. 2024). G35 is clearly resolved into two distinct UC H II regions in both RRL and continuum emission, while G28 only exhibits a central bright core at the location of its HC H II region. However, high-resolution ALMA observations show that this core in G28 is, in fact, an ionized ring that is not resolved with SMA (Law et al. 2022). Both G28 and G35 show larger scale diffuse continuum emission, likely due to contributions from thermal dust emission (Hernández-Hernández et al. 2014; Zhang et al. 2014). G20 has a central compact core with extended, diffuse continuum emission extending to the south-east. This core is tracing a known bright, molecule-rich HC H II region, while the diffuse emission traces a nearby, extended, but molecule-poor HC H II region (Galván-Madrid et al. 2009). In contrast to G28 and G35, this diffuse emission component is also seen in H31 α in G20, which suggests an extended reservoir of ionized gas, consistent with the presence of nearby H II

regions (Galván-Madrid et al. 2009). W33 shows the most complex continuum structure of our sources with a bright U-shaped feature surrounded by diffuse, arc-like structures that are reminiscent of those seen in the massive star-forming region G10.6-0.4 (Sollins et al. 2005b; Law et al. 2021), which have been interpreted as the ionized edges of clumps of molecular material. The RRL emission shows the same broad U-shaped-structure, but we cannot determine if similar arc-like structures are present in H31 α on small scales due to the lower SNR and coarse beam sizes in the line image cubes of W33.

4.2. Molecular Inventory

4.2.1. Summary of Molecule Detections

One of the primary goals of this work is to determine the chemical composition of each of our sources. To do so, we first aim to establish a comprehensive catalog of detected molecules. Here, we focus on those molecular transitions that are sufficiently bright to allow for an investigation of their spatial distribution and derivation of gas properties. Thus, we only consider transitions which have an absolute peak line intensity of $\gtrsim 3\sigma$. We consider a molecule detected if it has one line with a velocity-integrated intensity exceeding 5σ or at least two lines with total flux greater than 3σ . We excluded significantly blended lines during this process, which resulted in the removal of a few 10s of lines, or less than 5% of total identified lines. In practice, due to our initial peak flux cut, the vast majority of molecules are securely detected via the presence of a single, bright

Table 3. Image Cube Properties

Frequency Range (GHz)	Beam (" × ", deg)	Proj. Linear Res. (au × au)	δv (km s ⁻¹)	RMS ^a (mJy beam ⁻¹)
G28.20-0.05:				
Cont., 230 GHz	0.61 × 0.49, 48.6	3500 × 2800	...	1.0
Cont., 345 GHz	0.41 × 0.34, 44.6	2300 × 1900	...	1.3
208.948–216.910	0.64 × 0.51, 43.1	3600 × 2900	1.12	23.2
224.944–232.907	0.62 × 0.49, 43.6	3500 × 2800	1.12	23.2
332.908–340.870	0.42 × 0.36, 45.1	2400 × 2100	1.12	62.5
348.906–356.868	0.42 × 0.33, 36.8	2400 × 1900	1.12	90.0
G20.08-0.14 N:				
Cont., 230 GHz	0.69 × 0.45, 35.0	8500 × 5500	...	10.5
Cont., 345 GHz	1.62 × 1.46, 30.1	20000 × 18000	...	51.3
208.948–216.910	0.74 × 0.48, 33.3	9100 × 5900	1.12	32.6
224.944–232.907	0.71 × 0.46, 33.6	8700 × 5700	1.12	34.3
332.908–340.870	1.72 × 1.54, 22.2	21000 × 19000	1.12	114.8
348.906–356.868	1.67 × 1.48, 31.1	21000 × 18000	1.12	148.8
G35.58-0.03:				
Cont., 230 GHz	0.81 × 0.59, -89.2	8300 × 6000	...	3.8
Cont., 345 GHz	0.52 × 0.35, 79.9	5300 × 3600	...	7.0
208.948–216.910	1.35 × 1.27, -78.1	14000 × 13000	1.12	32.4
224.944–232.907	1.25 × 1.19, 13.6	13000 × 12000	1.12	34.2
332.908–340.870	0.77 × 0.49, 11.89	7900 × 5000	1.12	72.0
348.906–356.868	0.65 × 0.49, 20.3	6600 × 5000	1.12	107.3
W33 Main:				
Cont., 230 GHz	0.60 × 0.54, 48.9	1400 × 1300	...	7.0
Cont., 345 GHz	0.41 × 0.30, 19.2	980 × 720	...	18.0
208.948–216.910	2.82 × 2.09, 6.7	6800 × 5000	1.12	64.1
224.944–232.907	2.69 × 2.08, 6.8	6500 × 5000	1.12	64.9
332.908–340.870	2.04 × 2.03, 18.3	4900 × 4900	1.12	373.2
348.906–356.868	2.04 × 2.02, 18.6	4900 × 4800	1.12	454.8

^aThe line RMS noise is calculated over five line-free channels of the dirty image, while the continuum RMS noise is computed in a circular region with a radius three times the beam major axis in an emission-free region of the dirty image.

NOTE—All images were generated with a `robust` parameter of 0.5.

(>10 σ) line (e.g., C¹⁷O, ¹³CS, HCO⁺) or numerous (10s of lines) lines at modest SNR (3-5 σ). Molecule detections are compiled from spectra extracted within one beam at the continuum peaks of all sources, except for W33, where they represent the set of unique detections from spectra extracted at both the molecule-rich and RRL emission peak regions (see Appendix A). Figures 2 and 3 show representative spectra from the 230 GHz and 345 GHz receivers, respectively, which illustrate the

line-rich nature of our sample. Appendix B shows the full set of line identifications. Subsequently, we often classify molecule detections and gas properties according to molecular families, namely, those molecules containing oxygen (“O-bearing”), sulfur (“S-bearing”), or nitrogen (“N-bearing”) atoms, as well as hydrocarbons, which consist of only hydrogen and carbon atoms.

Figure 4 shows a summary of molecular detections per source. The majority of molecules are only de-

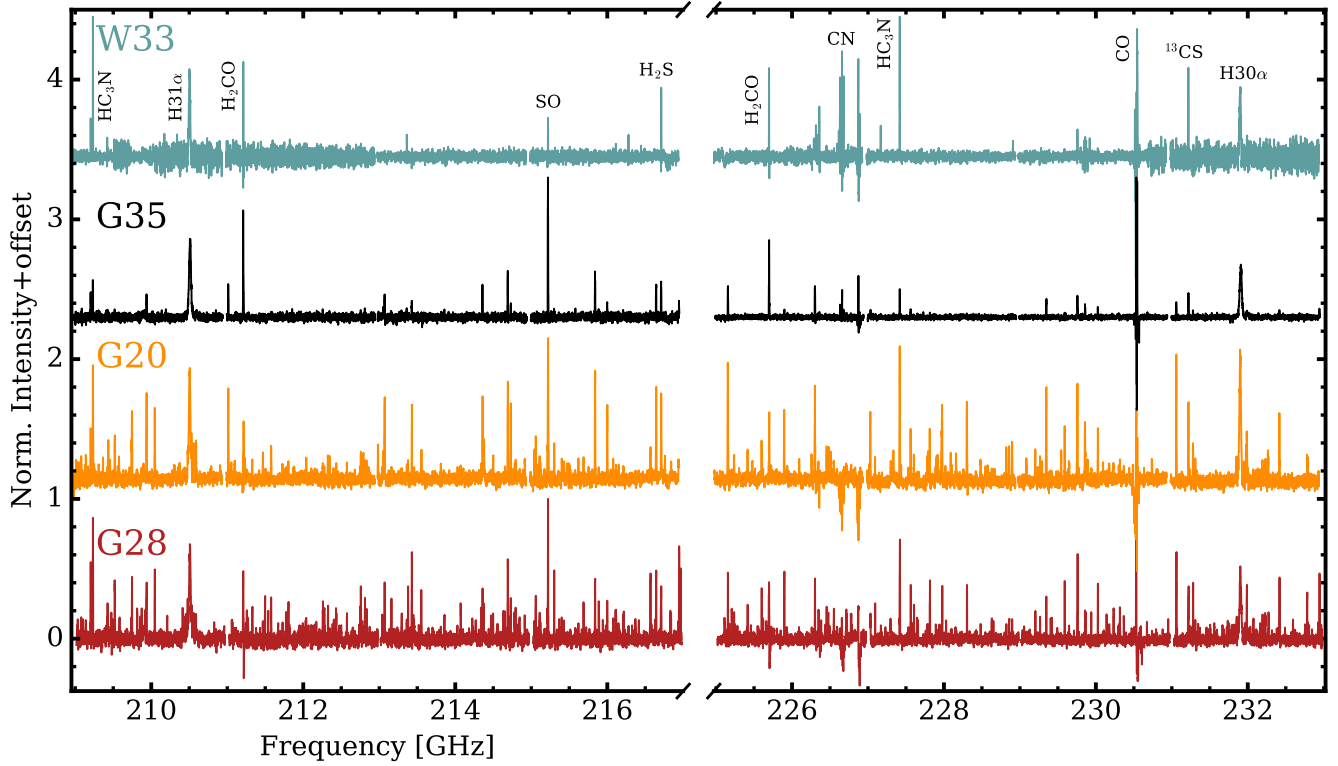


Figure 2. SMA spectra from ≈ 209 to 233 GHz of our sample extracted within one beam at the continuum peak of each source. There are small gaps in spectral coverage at the edges of each sideband. Sources are ordered by evolutionary stage from top (most evolved) to bottom (youngest). A few selected lines are labeled.

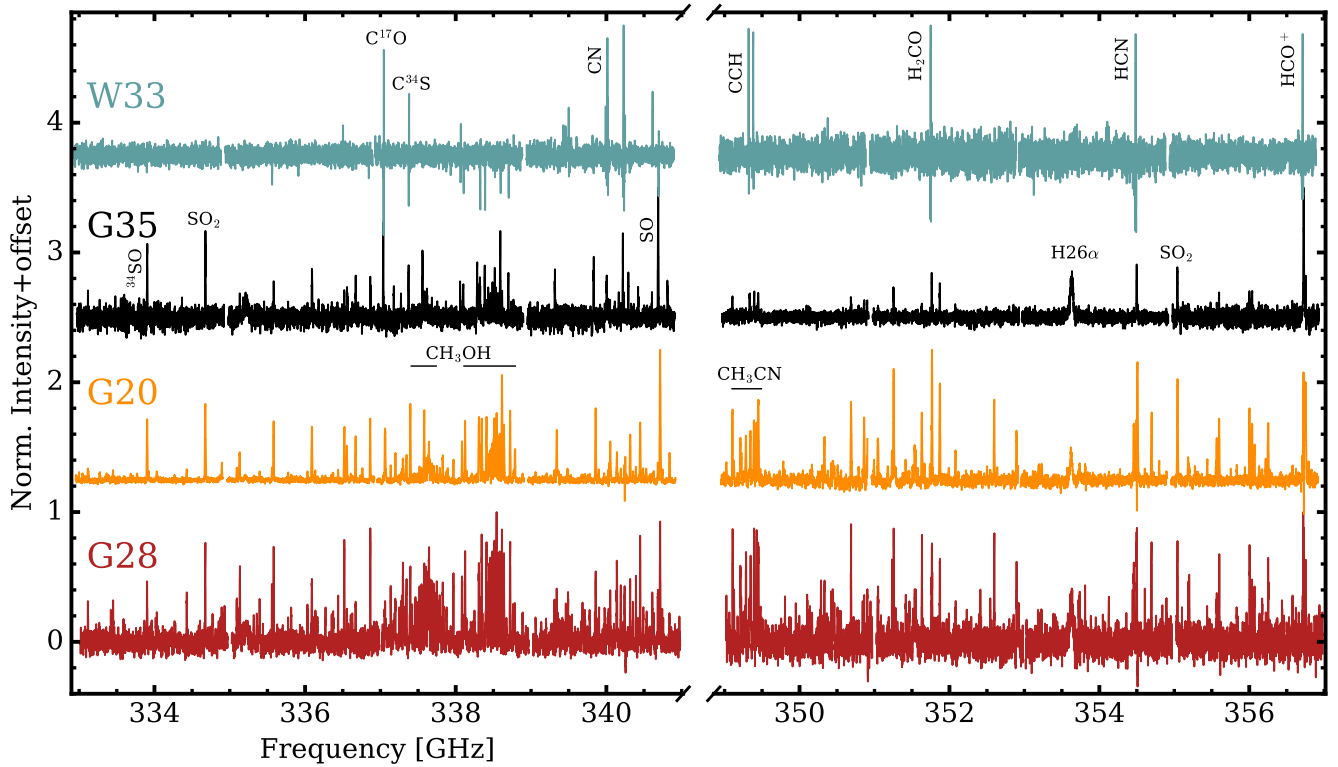


Figure 3. SMA spectra from ≈ 333 to 357 GHz of our sample. Otherwise, as in Figure 2.

tected in emission but a few (CO, H₂CO, CN, HCN, HCO⁺) consistently show both emission and absorption components. The CO, and to a lesser extent, CN, line profiles are heavily influenced by the line-of-sight gas distribution as indicated by the presence of multiple distinct kinematic components, while H₂CO, HCO⁺, and HCN show evidence of complex gas motions, i.e., inflows/outflows. W33 is the only source in which deuterated molecules (DCO⁺, DNC) are detected and shows additional absorption signatures in several molecules (C¹⁷O, CH₃OH, C³⁴S, SO, H₂CS, CCH) not seen in other sources (see Appendix A for more details). The non-detection of certain molecules is, in some cases, likely due to strong line blending. For instance, while ¹³C¹⁸O appears unique to W33, the single transition covered in our observations is blended with strong COM emission in G20 and G28, which is otherwise absent in W33 allowing us to only securely detect it here.

G28 and G20 have the most molecule detections (62 and 63, respectively), followed by the more modest G35 (28), and then the relatively molecule-poor W33 (23). G28 and G20 are chemically-rich in all types of molecules, including S-, O-, and N-bearing species. They also have numerous COM detections and appear similar in their overall chemical inventories. G35 has less than half of the total molecular detections of that of either G20 or G28 and does not show significant emission from large N- and O-bearing COMs, with H₂CCO and CH₃OCHO being the most complex molecules detected. Nonetheless, G35 does host a surprisingly rich sulfur chemistry that is nearly the same as G20 and G28 with the exception of a few rare isotopologues and hot gas tracers. W33 is the most molecule-poor source in our sample, with the simple COMs CH₃OH and CH₃CN being the most complex molecules detected. Emission from H α , H β , and H γ are detected in all sources, while H δ (G28, W33) and He α (G35, W33) are only detected in a subset of sources.

4.2.2. Summary of Line Detections

In addition to establishing the molecular inventory of each source, our observations were designed to include multiple lines with a wide range of upper state energies (E_u) to probe a variety of physical gas conditions.

Figure 5 shows the distribution of detected lines as a function of E_u . Overall, we detected ≈ 600 , ≈ 400 , ≈ 100 , and ≈ 80 lines in G28, G20, G35, and W33, respectively. While G20 and G28 look similar in their overall line E_u distributions, there are a few notable differences. In G20, we often detect additional higher E_u lines relative to G28, particularly in the S-bearing species, while in G28, we consistently have more line

detections of larger O-bearing COMs. For those species detected in all sources, we see the fewest number of lines on a per-molecule basis in W33, followed by G35, and those that are detected typically have lower E_u values. For instance, for CH₃OH, most detected lines in W33 and G35 are $E_u < 300$ K and $E_u < 500$ K, respectively, but in both G20 and G28, lines are consistently detected up to $E_u \approx 800$ K. A similar difference is seen in CH₃CN with only a few lower temperature transitions detected in G35 and W33, which taken together, indicates lower gas temperatures and/or efficient destruction (see Section 4.5 for more details).

Figure 5 is not intended to provide an exhaustive line census, since there are numerous faint lines that do not meet our peak line intensity cutoff in G20 and G28 (see Appendix B), but rather is meant as a catalog of those lines that are minimally blended, sufficiently bright to map the emission morphology, and can be used to extract robust flux measurements for excitation analysis in the following Sections. While shown in Figure 5 for comparison, for this reason, we excluded W33 from all subsequent analysis due to its substantial spatial filtering (see Section 3).

4.3. Molecular Line Emission Morphology

Nearly all of the detected molecular transitions are spatially resolved with the SMA. To visualize the line emission morphologies, we generated maps of velocity-integrated intensity, or “zerth moment maps,” from the image cubes of each detected transition using the Python package `bettermoments` (Teague & Foreman-Mackey 2018). Figures 6, 8, and 7 show zerth moment maps of representative molecular lines which are selected to highlight prominent morphological features of each source. These maps also demonstrate the complex, often molecule-specific, morphologies present across a wide range of scales from a few 1000 au up to ~ 1 pc, depending on the source.

All sources show evidence of compact, hot-core-like chemistry occurring near to the central massive protostars in addition to a diffuse, extended emission component whose orientation matches that of known molecular outflows, identified in either SiO or high-velocity CO emission (Xu & Wang 2013; Zhang et al. 2014; Gorai et al. 2024). Additional line emission substructures (e.g., rings, cavities, emission plateaus, asymmetries) are observed in all sources, highlighting the complex interplay between chemistry and physical gas conditions in these environments. Below, we provide a brief summary of each massive star-forming region, while Appendix C shows zerth moment map galleries of all detected molecules.

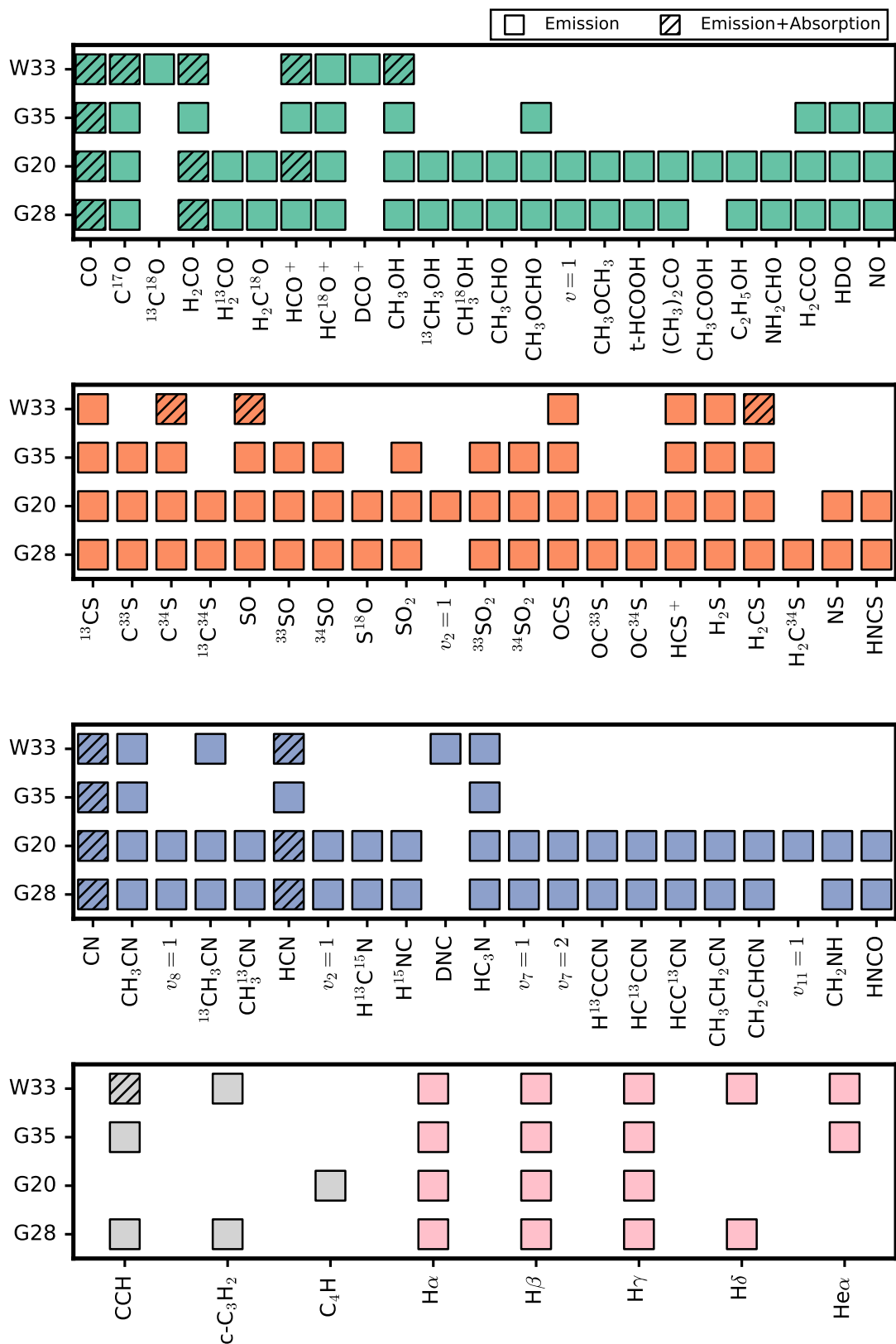


Figure 4. Gallery of molecular and RRL detections in the SMA sample which indicate if the species is detected in emission (solid box) or in both emission and absorption (diagonal lines). No molecules were detected only in absorption. Molecules are divided and colored as O-bearing (green), S-bearing (orange), N-bearing (blue), and hydrocarbons (gray). The detected RRLs are colored in pink. All listed transitions are in the $v = 0$ state, unless otherwise noted. Transitions with $v = 1, 2$, etc., are shown immediately to the right of the molecule name.

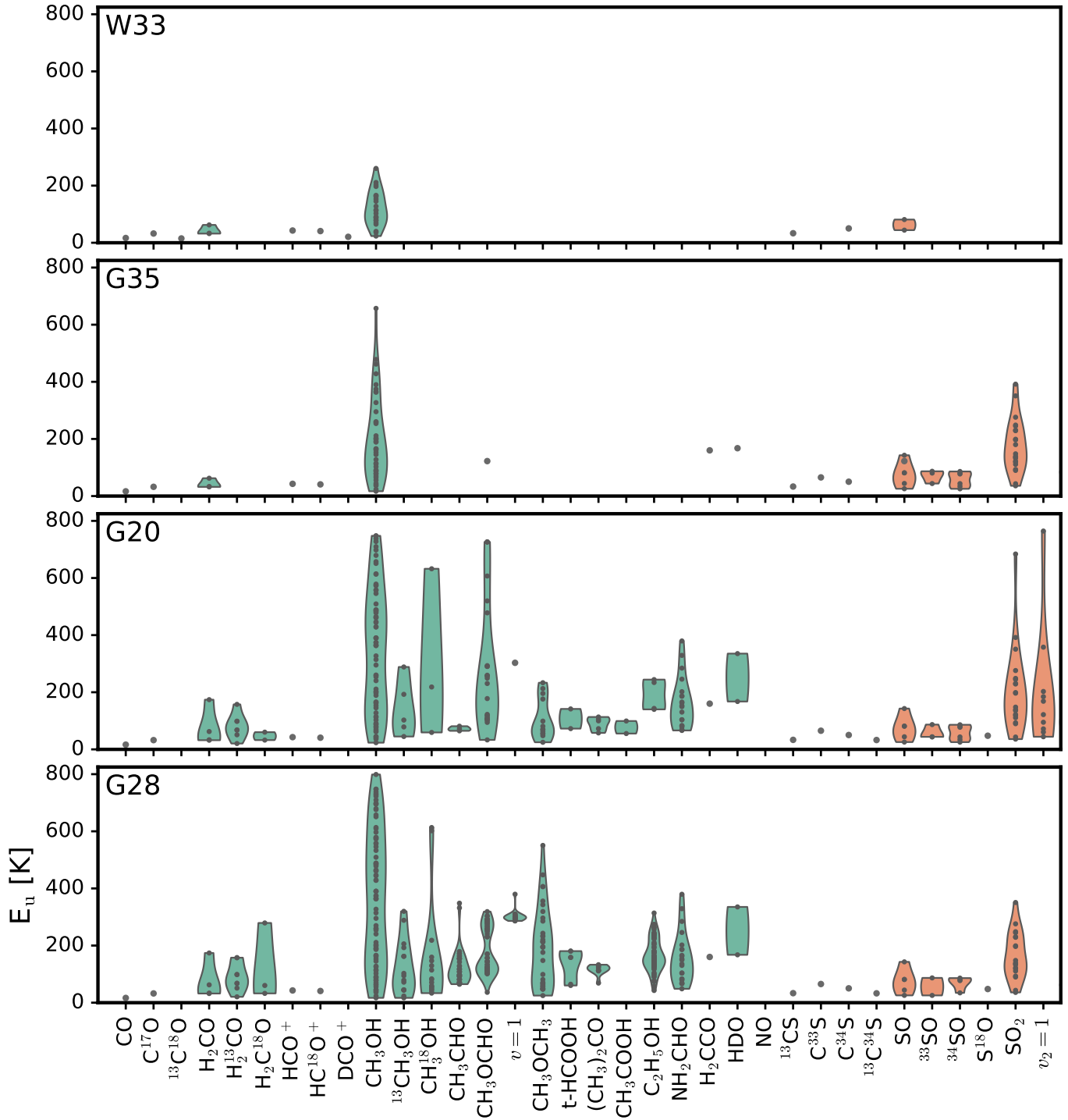


Figure 5. Violin plot of detected transitions as a function of E_u for G28, G20, G35, and W33. The width of each violin shows a kernel density estimation of the underlying E_u distribution for that molecule. Line detections are compiled from beam-averaged spectra at the continuum peaks of all sources, except for W33, where they represent the set of unique detections at both the molecule-rich and RRL emission peak regions (see Appendix B). Molecules are colored as in Figure 4.

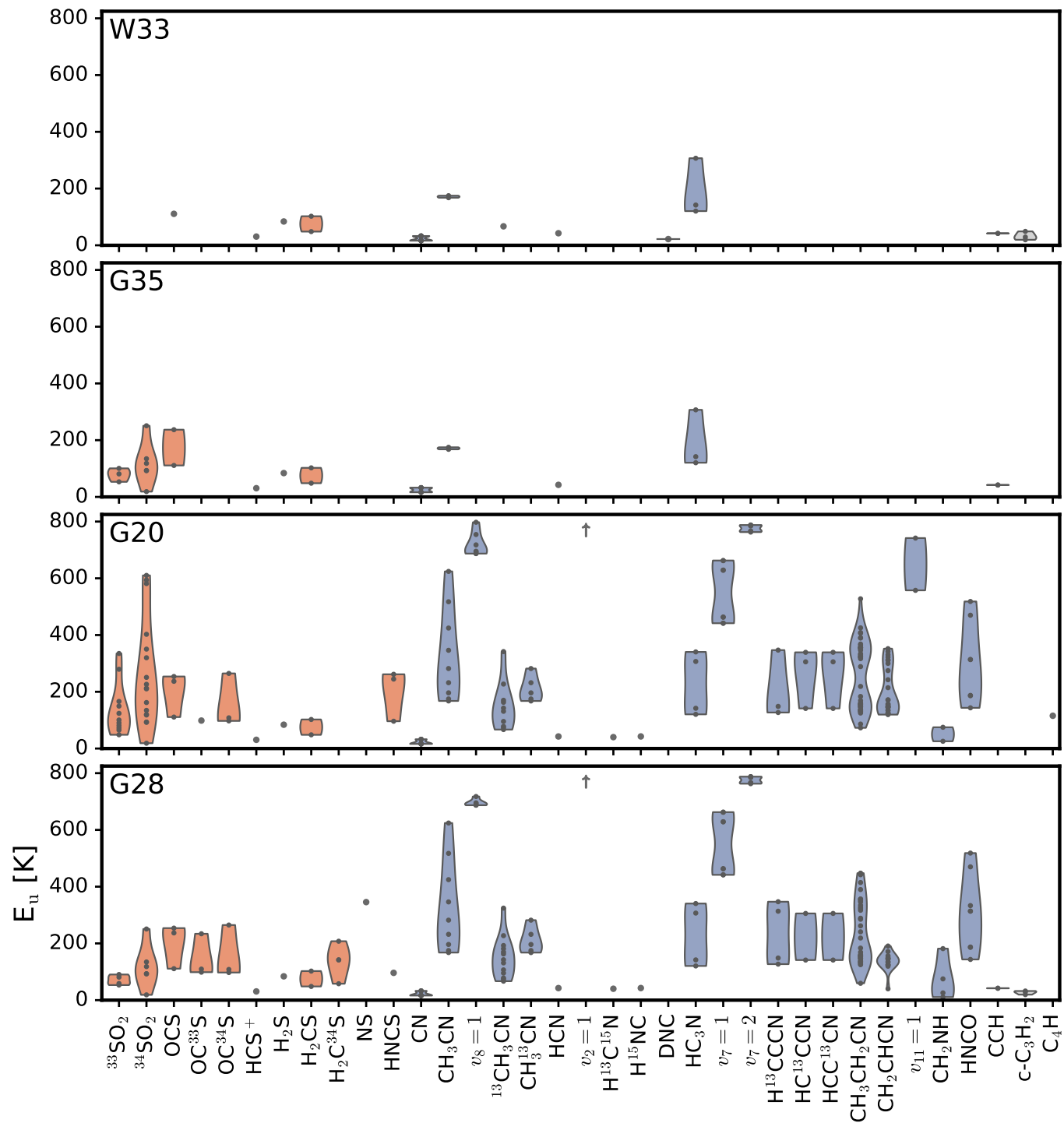


Figure 5. (continued) The detected HCN $v_2 = 1$ line, which has an $E_u = 1067$ K, is shown as an upward-facing arrow for visual clarity.

G28: consists of several distinct emission components summarized in Figure 6, which include: diffuse emission along the NE-SW direction extending out to ≈ 0.25 pc (e.g., H_2CO , CH_3OH , H_2CS , SO); a ring-like structure with a diameter of ≈ 8000 au with either a deep (e.g., CH_2NH) or shallow cavity (e.g., H_2S , HC_3N , ^{13}CS) surrounded by a diffuse envelope out to ≈ 12000 au; and a compact ($\lesssim 4000$ au) emission component, which is either in the form of an unresolved core (e.g., $\text{C}_2\text{H}_5\text{OH}$, CH_3OCHO , $v = 1$) or is spatially-resolved but with a mostly smooth emission profile (e.g., HDO , ^{34}SO). In the latter case, there are, however, tentative brightness asymmetries, which suggest the presence of additional substructure on small scales. Several of the compact molecules also show a diffuse plateau of emission with a diameter of $\lesssim 6000$ au (e.g., ^{34}SO , HDO , CH_3OCH_3), which is directly interior to the molecular ring. Many molecules show the presence of several components simultaneously, e.g., SO , which has both extended, large-scale emission and a ring on intermediate scales. Large-scale asymmetries are also seen, such as in $c\text{-C}_3\text{H}_2$, which is spatially offset to the NW of the molecular ring and continuum peak. This ring is not azimuthally symmetric and shows several, distinct bright clumps of emission (e.g., CH_3OH , SO , HC_3N , ^{13}CS). CN shows extended emission surrounding a deep but localized absorption region that is approximately coincident with the continuum peak and has a total size of ≈ 6000 au. This absorption manifests as an arc-like bowl in Figure 6. Overall, these structures are consistent with those identified in a subset of lines in high-angular resolution ALMA observations (Gorai et al. 2024), who attribute their origins to protostellar heating and outflow shocks as well as dense gas within a surrounding envelope.

G20: exhibits two primary emission components, as shown in Figure 7: extended emission (e.g., H_2CO , CH_3OH , SO) along the NE-SW direction with a total size of ≈ 1 pc and a compact core, which is spatially unresolved (< 8000 au) in most species (e.g., NH_2CHO , $\text{CH}_3\text{CH}_2\text{CN}$, SO_2 , $v_2 = 1$) at the location of a known molecule-rich HC H II region. In the latter case, a few molecules (e.g., HC_3N , OC^{34}S) also show a diffuse plateau of emission on scales of ~ 0.2 pc outside of this central core. The larger-scale, bipolar emission shows complex structure, i.e., in some molecules it is mostly symmetric along the NE-SW axis (e.g., SO , ^{13}CS), while in others (e.g., H_2CO , CH_3OH), the emission is asymmetric with substantially brighter and more extended emission in the NE direction. Moreover, there is an asymmetry along the minor axis of this extended emission with diffuse emission located out to ~ 0.3 pc toward the SE in the direction of another nearby H II

region. CN shows diffuse emission that extends beyond the large-scale emission of the other molecules and has an absorption feature co-located with the continuum. The stippling pattern present in Figure 7 is likely a signature of spatial filtering due to the large angular size of the CN emission.

G35: comprises two major emission components, summarized in Figure 8: diffuse, extended emission along the E-W direction (e.g., H_2CO , SO) with a total size of ≈ 0.7 pc and bright, compact ($\lesssim 0.2$ pc) emission, which traces the two central UC H II regions (e.g., HDO). This compact component is either centrally peaked (e.g., SO_2 , NO), or is asymmetric and peaks on a single, but not always the same UC H II region (e.g., ^{13}CS , CN , CH_3OH , CH_3OCHO). Both components are often present in the same molecule. CN shows extended emission, but along a different position angle than the extended emission of most other molecules, and an absorption region with a total size of ≈ 15000 au at the location of G35 East and West, which appears as a dark lane in Figure 8.

4.4. Line Peak Centroid Positions

While Figures 6-8 provide a representative view of each source, we often have many 10s of detected transitions per molecule (see Section 4.2.2). Thus, we next aim to synthesize this combination of spatial and spectral information to most accurately trace the relative molecular distributions. To do so, we first computed the position of the peak intensity for every detected transition and then computed the median position for each molecule. We visually confirmed that these centroids reflected the overall distribution of line peak positions well. When computing the median position, we also experimented with more stringent selection cuts in line peak intensities (beyond that of the initial 3σ criterion) but found that the centroid positions were not sensitive to the chosen thresholds. To better visualize the distributions, we also generated a kernel density estimation of the median position using the `gaussian_kde` task in `scipy` (Virtanen et al. 2020).

Figure 9 shows a summary of the median positions of all detected molecules in our sample sub-divided into categories for O-, N-, and S-bearing species. All three sources show some degree of spatial segregation among different molecular families and with respect to the continuum peaks. These often take the form of relative spatial offsets where different types of molecules cluster at certain positions, while others exhibit more complex structures, such as ring- or shell-like distributions. Below, we summarize these results for each source, while

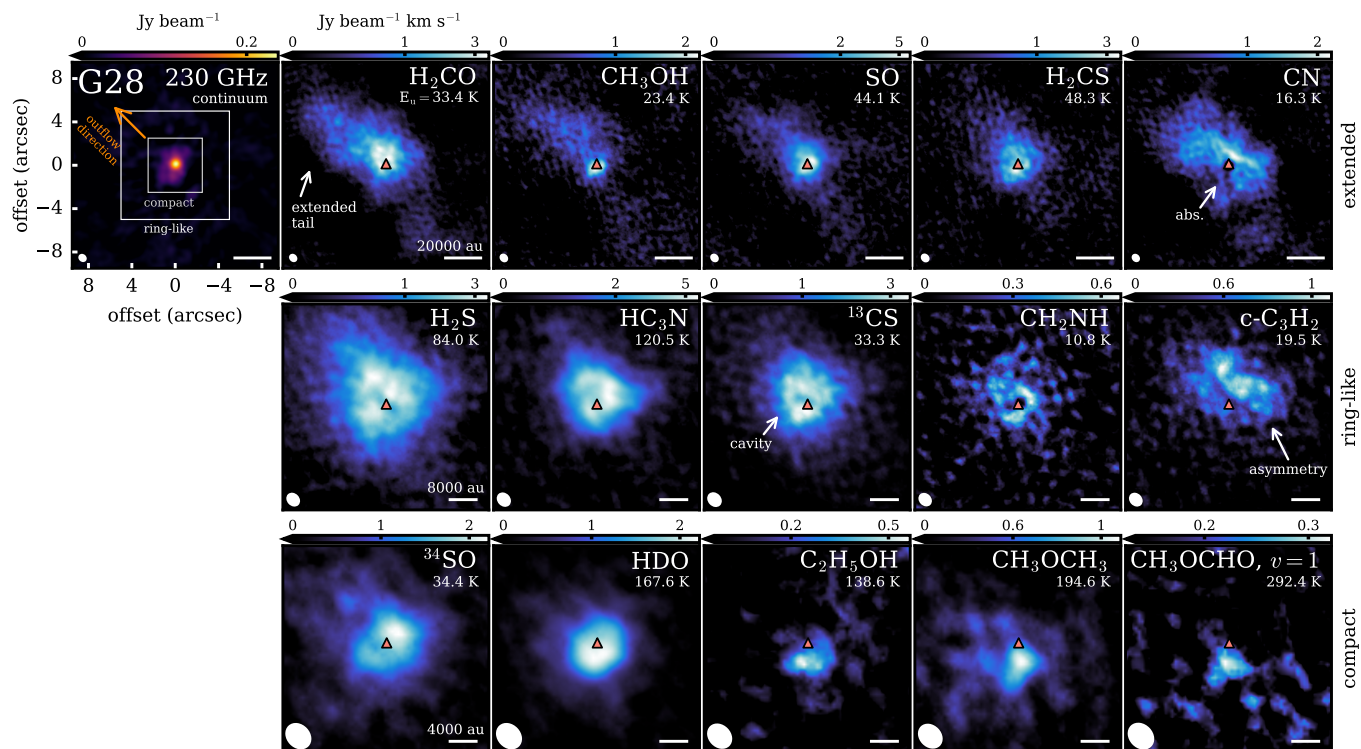


Figure 6. Zeroth moment maps of representative lines demonstrating the multiple emission components that comprise G28. Salient emission features are labeled with arrows. The upper state energy of each transition is labeled in the upper right. The continuum peak is shown as a pink triangle and the synthesized beam is shown in the lower left of each panel. The boxed regions in the continuum image show zoom-ins with corresponding scale bars denoting 20000 au, 8000 au, or 4000 au depending on the spatial scale, respectively, in each panel. The outflow direction, as traced by SiO emission (Gorai et al. 2024), is marked in the continuum image.

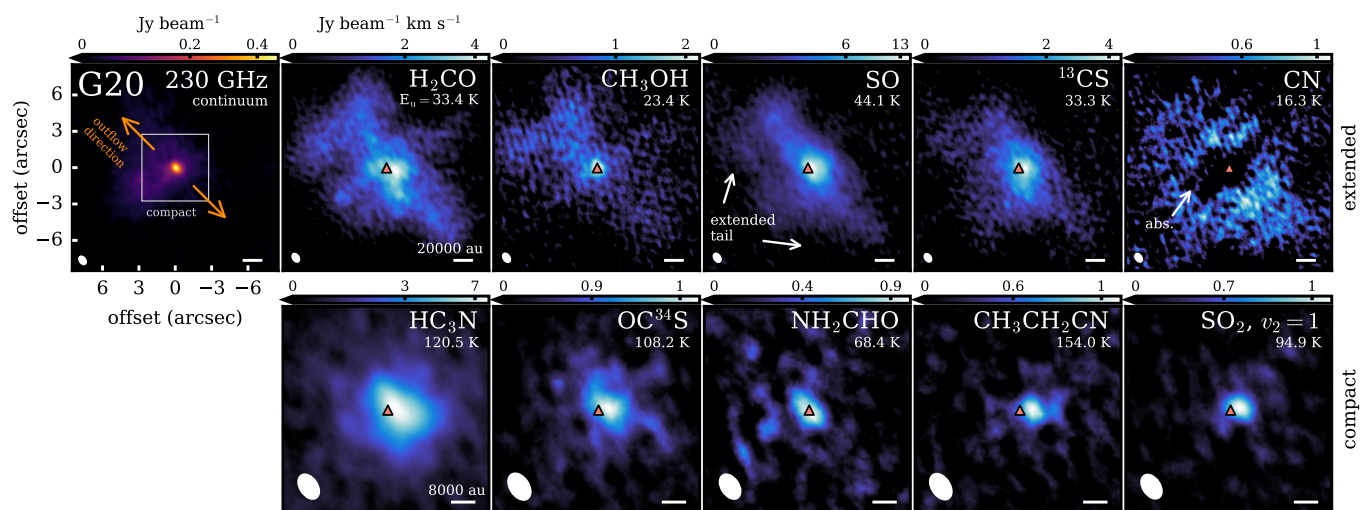


Figure 7. Zeroth moment maps of representative lines in G20. The outflow direction, as traced by SiO emission (Xu & Wang 2013), is marked in the continuum image. Otherwise, as in Figure 6.

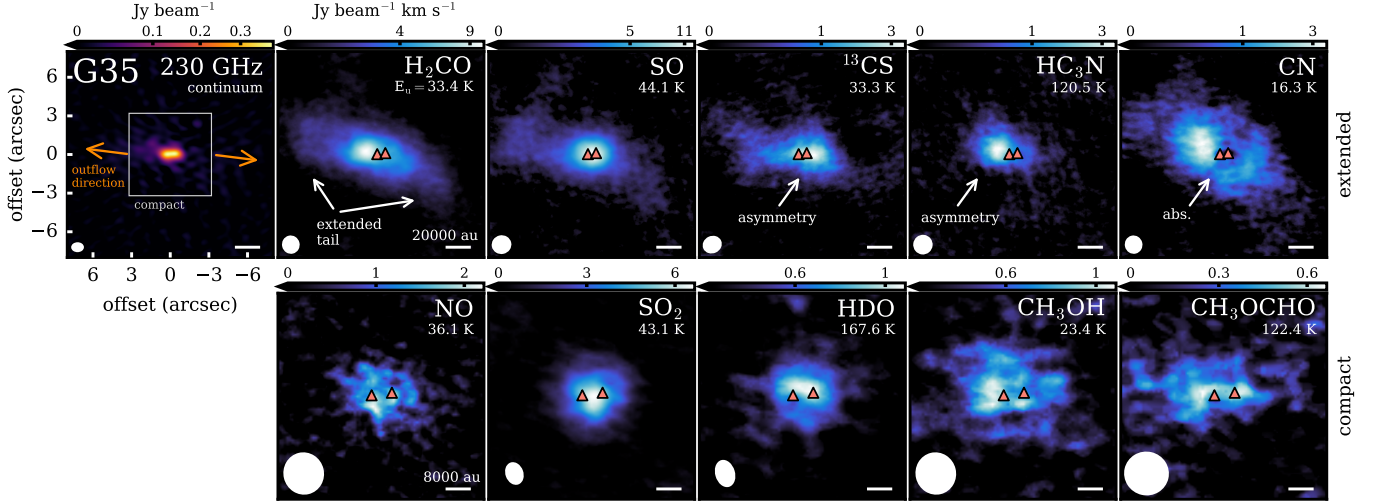


Figure 8. Zeroth moment maps of representative lines in G35. The outflow direction, as traced by high-velocity ^{12}CO emission (Zhang et al. 2014), is marked in the continuum image. Otherwise, as in Figure 6.

we discuss the origins of the observed separations in Section 5.2.

G28: The O-bearing molecules generally occupy two spatially distinct clusters in the SW and NE relative to the continuum peak. These two clusters correspond to the positions of the two hot molecular cores, HMC1 and HMC2, respectively, identified by Gorai et al. (2024) and we subsequently adopt the same nomenclature. HMC1, in particular, shows emission from the majority of COMs and isotopologues as well as vibrationally-excited CH_3OCHO , which taken together, indicates it likely hosts the densest and hottest gas in G28. In contrast, the N-bearing species are confined to a narrow but elongated distribution along the N-S direction and between HMC1 and HMC2, i.e., near the continuum peak. The S-bearing molecules also show a mutually distinct distribution in the form of a ring around the continuum peak, encircling the majority of O- and N-bearing peak positions. Only a few molecules peak outside of the central core of continuum emission, including HCO^+ , H_2S , HCS^+ , CCH , and $c\text{-C}_3\text{H}_2$, which are not shown in Figure 9 (but see Appendix C for zeroth moment maps of each of these molecules).

G20: The O- and N-bearing molecules are largely co-spatial but are offset to the west of the continuum peak of the central bright HC H II region. The S-bearing molecules show a slightly further offset to the west than that of the O- or N-bearing molecules. Similar offsets were previously observed by Galván-Madrid et al. (2009) in a few molecules (e.g., CH_3CN , SO_2 , OCS). Beyond these broad offsets from the continuum emission, no distinct structures are apparent. However, G20 is the most distant source in our sample and hence, our observations probe relatively coarse physical scales (see Table

3). Thus, the lack of apparent structure may simply reflect an observational limitation.

G35: The O-bearing molecules generally trace the continuum emission, with peaks between or at one of the two central UC H II regions. A few O-bearing molecules, however, are offset from the continuum to the east. Besides CH_3CN , which peaks at G35 West, all other N-bearing molecules are asymmetric and peak outside of G35 East. S-bearing molecules are found in two distinct clusters, i.e., near the central UC H II regions or in a shell outside of both regions. Interestingly, only those S-bearing molecules containing oxygen are found close to either G35 West or East, while those that are carbon-bearing are located in this exterior shell (see Section 5.2.2 for more details).

4.5. Rotational Temperatures and Column Densities

4.5.1. Fitting Process

Next, we aim to infer the physical gas conditions on a per-molecule basis in each of our sources. The high number of lines detected across a wide range of excitation conditions enables a rotational diagram approach (e.g., Goldsmith & Langer 1999). We only considered those lines which show a well-defined profile, i.e., no absorption or multiple kinematic components, and excluded blended lines. These criteria resulted in the inability to fit lines from only a few molecules, i.e., CO , CN , HCO^+ , HCN , H_2CO . We then fit all transitions with a single Gaussian profile and ensured fitting parameters were consistent for lines belonging to a single molecule, i.e., line FWHMs varied by no more than a factor of two and central velocities were within ± 2 velocity channels ($\approx 5 \text{ km s}^{-1}$) of the known systemic velocity. For each molecule, we further verified the initial line assignments

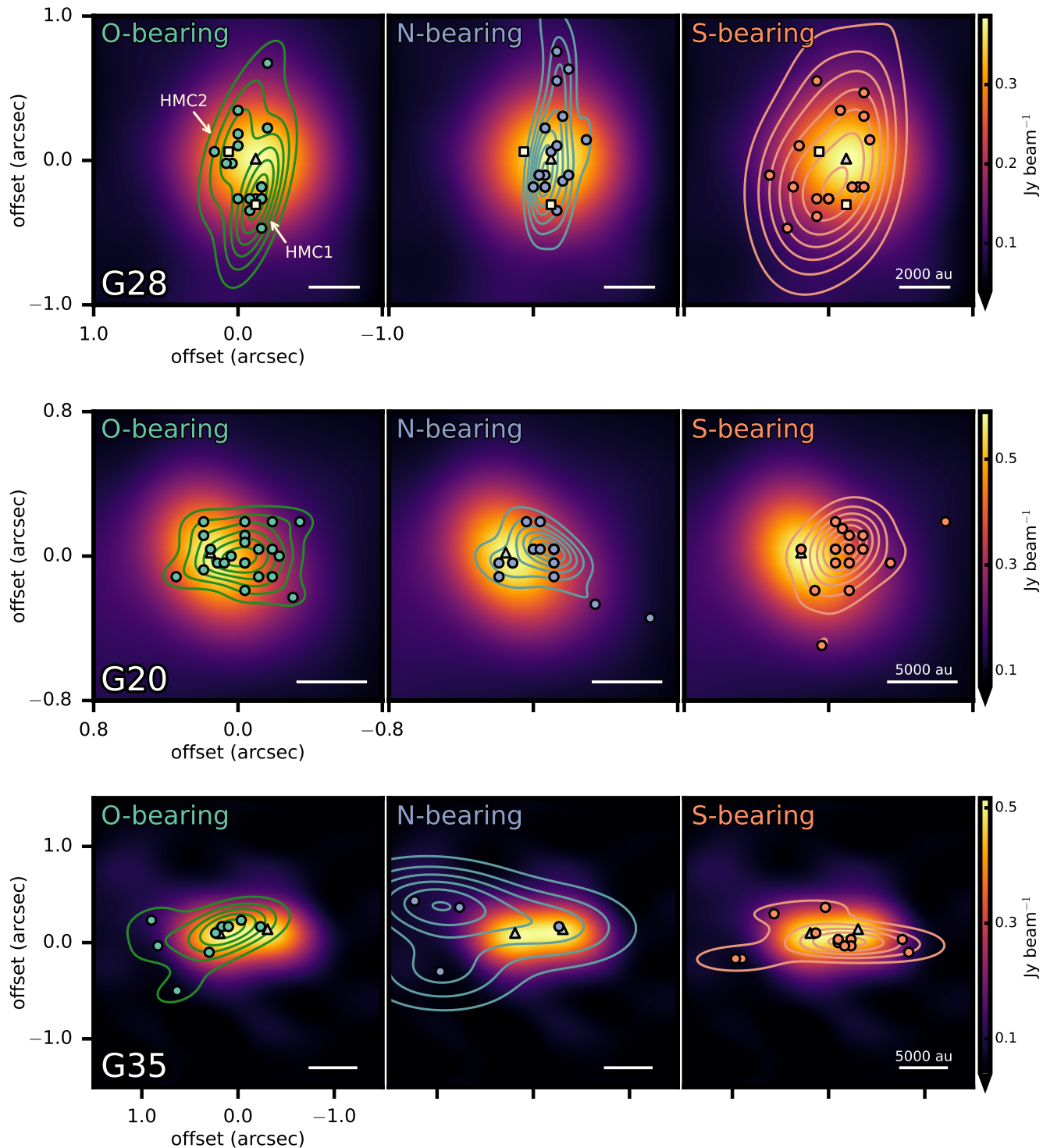


Figure 9. Peak positions for different molecular families (*columns*) are shown for each source (*rows*). Individual points are the median line peak positions for all detected molecules and the contours show the kernel density estimation. The 1.3 mm continuum is shown in colorscale. Continuum peaks are shown as gray triangles in all panels. In G28, the positions of HMC1 and HMC2 are denoted by white squares. In G35, the left-hand triangle corresponds to G35 East and the right-hand triangle marks G35 West. Only a few molecules peak far outside the continuum and are not shown here (but see Appendix C for a full gallery of zeroth moment maps for each species).

(Section 4.2.2) by checking that the best-fit rotational diagram model did not predict lines at frequencies that were covered by our observations but where no emission is detected. We treated unresolved hyperfine line components from the same species (e.g., CCH, C¹⁷O) as a single line by combining upper state level degeneracies and line intensities.

We used the Markov Chain Monte Carlo (MCMC) code `emcee` (Foreman-Mackey et al. 2013) to generate posterior probability distributions for rotational temperature (T_{rot}) and column density (N_{col}). Following Law et al. (2021), we simultaneously fit and correct for line optical depths. We explored a relatively broad parameter space of $10^{12} \text{ cm}^{-2} < N_{\text{col}} < 10^{20} \text{ cm}^{-2}$ and $50 \text{ K} < T_{\text{rot}} < 500 \text{ K}$ to capture the diverse physical gas conditions expected in massive star-forming regions (e.g., Moscadelli et al. 2018; Gieser et al. 2021; Motte et al. 2022). We ensured that the fitted T_{rot} and N_{col} values were not sharply peaked toward the edge of these priors. We adopted the 50th, 16th, and 84th percentiles from the marginalized posterior distributions as the best-fit values and uncertainties, respectively.

To ensure robust T_{rot} and N_{col} determinations, we only attempted to fit rotational diagrams for those species with at least two lines spanning a range of 30 K or more in E_u . For those molecules that did not meet this criterion, or only had multiple low-SNR line detections resulting in poor T_{rot} constraints, we instead adopted a rotational temperature from a chemically-similar species, i.e., belonging to the same molecular family (see Section 4.2.1). Assumed T_{rot} values are marked by square brackets in Table 4. We excluded all highly optically-thick lines from the rotational diagram analysis. For molecules for which the main isotopologue lines are expected to be optically thick, we instead used minor isotopologues, when available, along with the appropriate isotopic elemental ratios to infer their column densities (see Appendix E; Wilson & Rood 1994; Milam et al. 2005; Yu et al. 2020; Yan et al. 2023). Given the high gas temperatures expected in our sources, we selected spectroscopic data for partition functions that included any non-negligible contributions from vibrational and torsional states. When such data was unavailable, we applied temperature-dependent corrections to the derived column densities. See Appendix D for a detailed description of these corrections and a summary of the spectroscopic data used in this work.

In G20, we only use those lines covered by the lower frequency receiver to derive rotational temperatures and column densities. This was done to avoid potentially significant beam dilution from the coarser angular resolution associated with data from the higher frequency

receiver, as noted in Section 3. However, a handful of molecules (e.g., C¹⁷O, HC¹⁸O⁺, ³³SO₂, H₂CCO, CH₃¹³CN, C³³S, C³⁴S) only have transitions in the high frequency spectral windows. For these molecules, we also adopted the T_{rot} of a chemically-similar species to compute their column densities, but caution that these N_{col} values are likely underestimates.

4.5.2. Molecular Column Densities

To probe the spatial variation expected across our sources, we chose a few points of interest for this analysis. In G28, we picked HMC1 and the continuum peak, while in G35, we extracted values from both the G35 East and West UC H II regions. In G20, we chose the continuum peak of the central HC H II region. Table 4 and Figure 10 provide a summary of the derived values. Table 4 is also available in its entirety in machine-readable format.

We derived the highest number of rotational temperatures for G28, followed by G20, and then G35, where we only have a handful of T_{rot} constraints. We have a T_{rot} estimate from either CH₃CN or one its isotopologues, which provide a measure of physical gas temperatures, in each of our sources. G28 possesses the hottest ($\approx 210 \text{ K}$) gas, followed by warm ($\approx 160 \text{ K}$) gas in G20, and then relatively lukewarm ($\approx 60\text{-}70 \text{ K}$) gas in G35. In terms of typical N_{col} , both G20 and G28 have column densities that are several orders of magnitude greater than those seen in G35. Overall, G20 and G28 show comparable molecular column densities and relative N_{col} ratios among different species, which reflects their chemical similarity.

We find modest evidence for spatial variation in the gas properties across our sources. We focus on G35 and G28, since we lack adequate physical resolution for a meaningful analysis in G20 due to its far distance. While G35 East and West have consistent rotational temperatures, G35 West is generally enhanced in molecular column densities. The brightness asymmetries observed in the zeroth moment maps of a few molecules (Figure 8) are reflected in N_{col} differences, such as CCH, HC₃N, which show higher N_{col} in G35 East. Nonetheless, these differences are typically no more than a factor of a few and both cores appear broadly chemically similar. In G28, HMC1 generally shows warmer rotational temperatures of $\approx 20\text{-}50 \text{ K}$ and higher column densities by a factor of a few-to-several versus the continuum peak. These high temperatures and densities are consistent with its previous classification as a hot core (Gorai et al. 2024).



Figure 10. Derived molecular column densities for selected positions in G28 (left), G20 (middle), and G35 (right). Molecules are colored as in Figure 4 and labels for the vibrational states correspond to the molecule listed immediately above. Due to the wide range in N_{col} shown, markers are larger than the uncertainties in most cases.

Table 4. Rotational Temperature and Column Density

	G28 HMC1		G28 Cont. Peak		G20 Cont. Peak		G35 East Cont. Peak		G35 West Cont. Peak	
	T_{rot} (K)	N_{col} (cm^{-2})	T_{rot} (K)	N_{col} (cm^{-2})	T_{rot} (K)	N_{col} (cm^{-2})	T_{rot} (K)	N_{col} (cm^{-2})	T_{rot} (K)	N_{col} (cm^{-2})
C ¹⁷ O	[125]	$\gtrsim 2.9 \times 10^{16}$	[138]	$\gtrsim 2.7 \times 10^{16}$	[138]	$\gtrsim 1.3 \times 10^{16}$	[77]	$\gtrsim 1.1 \times 10^{16}$	[61]	$\gtrsim 8.4 \times 10^{15}$
H ₂ ¹³ CO	181 ⁺¹⁷ ₋₁₄	$\gtrsim 2.0 \times 10^{16}$	165 ⁺¹⁸ ₋₁₄	1.1 ^{+1.2} _{-1.0} $\times 10^{16}$	138 ⁺⁴⁵ ₋₂₆	6.3 ^{+8.7} _{-5.2} $\times 10^{15}$
H ₂ C ¹⁸ O	[181]	1.6 ^{+1.8} _{-1.4} $\times 10^{15}$	[165]	1.5 ^{+1.7} _{-1.4} $\times 10^{15}$	[138]	3.6 ^{+4.2} _{-3.0} $\times 10^{14}$
HC ¹⁸ O ⁺	[125]	5.3 ^{+4.7} _{-4.7} $\times 10^{13}$	[138]	7.5 ^{+8.6} _{-8.5} $\times 10^{13}$	[138]	$\gtrsim 9.9 \times 10^{12}$	[77]	2.1 ^{+2.7} _{-1.4} $\times 10^{13}$
CH ₃ OH ^a	...	5.6 ^{+6.4} _{-4.9} $\times 10^{18}$...	3.4 ^{+3.6} _{-3.2} $\times 10^{18}$...	2.5 ^{+2.8} _{-2.2} $\times 10^{19}$	77 ⁺³ ₋₃	1.8 ^{+1.9} _{-1.7} $\times 10^{16}$	61 ⁺⁴ ₋₃	$\gtrsim 1.8 \times 10^{16}$
¹³ CH ₃ OH	125 ⁺³ ₋₃	8.6 ^{+8.8} _{-8.3} $\times 10^{16}$	138 ⁺⁷ ₋₆	4.3 ^{+4.5} _{-4.2} $\times 10^{16}$	[138]	3.1 ^{+3.6} _{-2.7} $\times 10^{16}$
CH ₃ ¹⁸ OH	161 ⁺¹⁷ ₋₁₄	1.8 ^{+2.1} _{-1.6} $\times 10^{16}$	129 ⁺¹⁰ ₋₈	1.1 ^{+1.2} _{-1.0} $\times 10^{16}$	[138]	7.3 ^{+8.1} _{-6.4} $\times 10^{16}$
CH ₃ CHO	[103]	4.1 ^{+4.2} _{-3.3} $\times 10^{15}$	[74]	5.6 ^{+5.7} _{-5.5} $\times 10^{15}$	[228]	7.2 ^{+7.9} _{-6.5} $\times 10^{15}$
CH ₃ OCHO	103 ⁺¹ ₋₁	1.9 ^{+1.9} _{-1.8} $\times 10^{16}$	74 ⁺² ₋₁	9.3 ^{+9.8} _{-8.8} $\times 10^{15}$	[228]	7.2 ^{+8.6} _{-5.7} $\times 10^{16}$	[77]	7.0 ^{+7.6} _{-6.6} $\times 10^{13}$	[61]	9.9 ^{+11.0} _{-8.7} $\times 10^{13}$
$v = 1$	[103]	1.2 ^{+1.2} _{-1.2} $\times 10^{17}$	[74]	8.1 ^{+8.5} _{-7.7} $\times 10^{16}$	[228]	4.4 ^{+4.6} _{-4.3} $\times 10^{17}$
CH ₃ OCH ₃	140 ⁺⁵ ₋₅	5.7 ^{+5.9} _{-5.6} $\times 10^{16}$	149 ⁺⁷ ₋₇	2.9 ^{+3.1} _{-2.9} $\times 10^{16}$	228 ⁺⁴³ ₋₃₃	4.0 ^{+5.5} _{-3.3} $\times 10^{16}$
t-HCOOH	[125]	9.4 ^{+9.9} _{-8.9} $\times 10^{15}$	[138]	4.7 ^{+4.9} _{-4.4} $\times 10^{15}$	[138]	1.5 ^{+1.7} _{-1.3} $\times 10^{16}$
C ₂ H ₅ OH	59 ⁺² ₋₂	3.0 ^{+3.2} _{-2.4} $\times 10^{16}$	61 ⁺⁴ ₋₄	2.3 ^{+2.6} _{-2.1} $\times 10^{16}$	[228]	2.8 ^{+3.2} _{-2.4} $\times 10^{17}$
(CH ₃) ₂ CO	[140]	4.4 ^{+4.6} _{-4.1} $\times 10^{15}$	[149]	7.5 ^{+8.0} _{-7.0} $\times 10^{15}$	51 ⁺¹ ₋₁	$\gtrsim 1.2 \times 10^{16}$
CH ₃ COOH	[228]	2.1 ^{+2.4} _{-1.7} $\times 10^{17}$
NH ₂ CHO	88 ⁺⁶ ₋₆	$\gtrsim 2.3 \times 10^{15}$	91 ⁺¹⁰ ₋₈	1.5 ^{+1.6} _{-1.4} $\times 10^{15}$	55 ⁺² ₋₂	$\gtrsim 1.9 \times 10^{15}$
H ₂ CCO	[181]	$\gtrsim 1.9 \times 10^{16}$	[165]	$\gtrsim 8.3 \times 10^{15}$	[138]	$\gtrsim 1.2 \times 10^{15}$	[61]	1.0 ^{+1.6} _{-0.5} $\times 10^{15}$
HDO	392 ⁺⁷⁵ ₋₉₀	9.0 ^{+10.0} _{-7.9} $\times 10^{16}$	381 ⁺⁷⁹ ₋₉₀	8.2 ^{+9.2} _{-7.3} $\times 10^{16}$	[214]	$\gtrsim 7.7 \times 10^{16}$	[77]	4.0 ^{+4.3} _{-3.7} $\times 10^{15}$	[61]	7.2 ^{+7.6} _{-6.7} $\times 10^{15}$
¹³ CS	[178]	$\gtrsim 2.0 \times 10^{15}$	[169]	1.5 ^{+1.6} _{-1.5} $\times 10^{15}$	[132]	$\gtrsim 3.3 \times 10^{15}$	[122]	2.4 ^{+2.5} _{-2.2} $\times 10^{14}$	[133]	3.4 ^{+3.6} _{-3.1} $\times 10^{14}$
C ³³ S	[178]	$\gtrsim 1.2 \times 10^{15}$	[169]	$\gtrsim 1.1 \times 10^{15}$	[132]	$\gtrsim 4.3 \times 10^{14}$	[122]	1.2 ^{+1.3} _{-1.0} $\times 10^{14}$	[133]	1.2 ^{+1.4} _{-1.0} $\times 10^{14}$
C ³⁴ S	[178]	$\gtrsim 2.0 \times 10^{15}$	[169]	$\gtrsim 2.0 \times 10^{15}$	[132]	$\gtrsim 7.8 \times 10^{14}$	[122]	2.7 ^{+3.0} _{-2.4} $\times 10^{14}$	[133]	2.8 ^{+3.0} _{-2.6} $\times 10^{14}$
¹³ C ³⁴ S	[178]	3.6 ^{+4.0} _{-3.3} $\times 10^{14}$	[169]	3.7 ^{+4.0} _{-3.4} $\times 10^{14}$	[132]	4.1 ^{+4.7} _{-3.4} $\times 10^{14}$
SO ^a	...	1.3 ^{+1.6} _{-0.9} $\times 10^{18}$...	8.4 ^{+10.0} _{-6.9} $\times 10^{17}$...	1.6 ^{+2.0} _{-1.3} $\times 10^{18}$...	2.4 ^{+2.8} _{-2.0} $\times 10^{16}$...	2.9 ^{+3.3} _{-2.6} $\times 10^{16}$
³³ SO	[178]	4.1 ^{+4.8} _{-3.4} $\times 10^{14}$	[169]	6.9 ^{+8.1} _{-5.8} $\times 10^{14}$	[132]	4.1 ^{+5.6} _{-2.6} $\times 10^{15}$	[108]	2.8 ^{+3.2} _{-2.2} $\times 10^{14}$	[169]	3.3 ^{+3.8} _{-3.0} $\times 10^{14}$
³⁴ SO	[178]	$\gtrsim 6.9 \times 10^{15}$	[169]	$\gtrsim 9.3 \times 10^{15}$	[132]	$\gtrsim 2.5 \times 10^{16}$	[108]	2.6 ^{+2.6} _{-2.5} $\times 10^{15}$	[169]	3.7 ^{+3.7} _{-3.6} $\times 10^{15}$
S ¹⁸ O	[178]	4.2 ^{+5.2} _{-3.1} $\times 10^{15}$	[169]	2.7 ^{+3.3} _{-2.4} $\times 10^{15}$	[132]	4.7 ^{+5.7} _{-3.8} $\times 10^{15}$
SO ₂ ^a	...	9.0 ^{+11.8} _{-6.4} $\times 10^{17}$...	9.1 ^{+9.3} _{-9.0} $\times 10^{17}$...	2.6 ^{+2.9} _{-2.4} $\times 10^{16}$...	3.5 ^{+4.4} _{-2.6} $\times 10^{16}$...	4.1 ^{+4.8} _{-3.8} $\times 10^{16}$
³³ SO ₂	[178]	1.1 ^{+1.4} _{-0.8} $\times 10^{16}$	[169]	1.1 ^{+1.1} _{-1.1} $\times 10^{16}$	[132]	$\gtrsim 3.1 \times 10^{14}$	[108]	4.1 ^{+5.1} _{-3.0} $\times 10^{14}$	[169]	4.7 ^{+5.5} _{-3.8} $\times 10^{14}$
³⁴ SO ₂	[178]	1.4 ^{+1.4} _{-1.3} $\times 10^{16}$	[169]	1.7 ^{+1.7} _{-1.6} $\times 10^{16}$	132 ⁺¹² ₋₁₀	6.5 ^{+6.9} _{-6.2} $\times 10^{16}$	[108]	2.8 ^{+3.3} _{-2.4} $\times 10^{15}$	[169]	6.9 ^{+8.5} _{-5.3} $\times 10^{15}$
OCS ^a	...	3.2 ^{+3.9} _{-2.3} $\times 10^{17}$...	2.2 ^{+2.5} _{-2.0} $\times 10^{17}$...	3.2 ^{+5.7} _{-1.3} $\times 10^{17}$	108 ⁺⁴⁰ ₋₂₇	3.1 ^{+3.7} _{-2.7} $\times 10^{15}$	169 ⁺⁵³ ₋₃₄	3.3 ^{+3.7} _{-3.1} $\times 10^{15}$
OC ³³ S	[178]	3.8 ^{+4.7} _{-3.1} $\times 10^{15}$	[169]	2.7 ^{+3.0} _{-2.4} $\times 10^{15}$	[132]	3.8 ^{+6.7} _{-4.6} $\times 10^{15}$
OC ³⁴ S	178 ⁺²² ₋₁₈	1.3 ^{+1.4} _{-1.3} $\times 10^{16}$	169 ⁺²⁶ ₋₂₀	9.3 ^{+9.8} _{-8.7} $\times 10^{15}$	[132]	1.2 ^{+1.5} _{-0.9} $\times 10^{16}$
HCS ⁺	[178]	5.0 ^{+5.7} _{-4.4} $\times 10^{14}$	[169]	4.1 ^{+4.4} _{-3.7} $\times 10^{14}$	[132]	5.4 ^{+7.7} _{-2.8} $\times 10^{14}$	[122]	6.4 ^{+7.0} _{-5.0} $\times 10^{13}$	[133]	5.8 ^{+7.0} _{-4.6} $\times 10^{13}$
H ₂ S	[178]	3.5 ^{+4.0} _{-3.0} $\times 10^{16}$	[169]	3.2 ^{+3.6} _{-2.8} $\times 10^{16}$	[132]	$\gtrsim 1.3 \times 10^{17}$	[122]	4.6 ^{+5.0} _{-4.3} $\times 10^{15}$	[133]	5.1 ^{+5.5} _{-4.7} $\times 10^{15}$
H ₂ CS ^a	...	2.4 ^{+2.8} _{-1.9} $\times 10^{16}$...	1.1 ^{+1.2} _{-0.8} $\times 10^{16}$	[214]	$\gtrsim 1.3 \times 10^{16}$	122 ⁺⁵⁴ ₋₂₅	1.3 ^{+1.7} _{-1.1} $\times 10^{15}$	133 ⁺⁷⁸ ₋₃₀	1.2 ^{+1.8} _{-1.0} $\times 10^{15}$
H ₂ C ³⁴ S	[178]	1.8 ^{+2.0} _{-1.6} $\times 10^{15}$	[169]	7.7 ^{+8.6} _{-6.7} $\times 10^{14}$
NS	[212]	2.1 ^{+2.4} _{-1.9} $\times 10^{15}$	[155]	5.0 ^{+8.8} _{-2.3} $\times 10^{15}$
HNCS	[178]	1.5 ^{+1.8} _{-1.1} $\times 10^{15}$	[169]	1.5 ^{+2.3} _{-0.7} $\times 10^{15}$	[132]	2.5 ^{+3.0} _{-2.0} $\times 10^{15}$
CH ₃ CN ^a	...	7.9 ^{+8.5} _{-7.0} $\times 10^{16}$...	4.8 ^{+5.2} _{-4.1} $\times 10^{16}$...	3.9 ^{+4.8} _{-3.5} $\times 10^{16}$	71 ⁺⁸ ₋₅	$\gtrsim 1.4 \times 10^{15}$	62 ⁺²⁹ ₋₂₁	$\gtrsim 2.3 \times 10^{15}$
$v_8 = 1$	[212]	2.3 ^{+2.6} _{-2.0} $\times 10^{16}$	[228]	1.3 ^{+1.5} _{-1.1} $\times 10^{16}$	[155]	$\gtrsim 4.9 \times 10^{15}$
¹³ CH ₃ CN	212 ⁺²⁹ ₋₂₃	1.7 ^{+1.8} _{-1.5} $\times 10^{15}$	228 ⁺⁴² ₋₂₈	1.0 ^{+1.1} _{-0.9} $\times 10^{15}$	155 ⁺³² ₋₂₃	7.5 ^{+9.3} _{-6.8} $\times 10^{14}$
CH ₃ ¹³ CN	[212]	1.6 ^{+1.8} _{-1.3} $\times 10^{15}$	[228]	2.1 ^{+2.7} _{-1.6} $\times 10^{15}$	[155]	$\gtrsim 2.4 \times 10^{14}$
HCN, $v_2 = 1$	[304]	$\gtrsim 3.0 \times 10^{15}$	[299]	3.4 ^{+3.8} _{-3.0} $\times 10^{15}$	[155]	2.3 ^{+2.7} _{-2.0} $\times 10^{16}$
H ¹³ C ¹⁵ N	[233]	2.0 ^{+2.3} _{-1.7} $\times 10^{14}$	[177]	1.5 ^{+1.5} _{-1.4} $\times 10^{14}$	[155]	$\gtrsim 6.3 \times 10^{13}$
H ¹⁵ NC	[233]	3.2 ^{+4.1} _{-2.3} $\times 10^{14}$	[177]	1.6 ^{+1.7} _{-1.7} $\times 10^{14}$	[155]	$\gtrsim 5.9 \times 10^{13}$
HC ₃ N ^a	...	4.8 ^{+6.0} _{-4.1} $\times 10^{16}$...	3.6 ^{+3.8} _{-3.4} $\times 10^{16}$...	6.1 ^{+6.4} _{-5.7} $\times 10^{16}$	146 ⁺⁷⁹ ₋₄₃	2.8 ^{+3.7} _{-2.4} $\times 10^{14}$	[146]	1.6 ^{+1.7} _{-1.5} $\times 10^{14}$
$v_7 = 1$	304 ⁺³⁵ ₋₃₀	6.8 ^{+7.0} _{-6.5} $\times 10^{15}$	299 ⁺³³ ₋₂₈	6.5 ^{+6.8} _{-6.3} $\times 10^{15}$	[155]	$\gtrsim 4.2 \times 10^{16}$
$v_7 = 2$	[304]	6.3 ^{+6.6} _{-5.9} $\times 10^{15}$	[299]	7.2 ^{+7.6} _{-6.8} $\times 10^{15}$	[155]	7.4 ^{+7.7} _{-7.2} $\times 10^{16}$
H ¹³ CCCN	233 ⁺⁴⁸ ₋₃₇	1.0 ^{+1.3} _{-1.1} $\times 10^{15}$	177 ⁺¹⁸ ₋₁₅	7.6 ^{+8.1} _{-7.1} $\times 10^{14}$	[155]	1.2 ^{+1.2} _{-1.1} $\times 10^{15}$
HC ¹³ CCN	[233]	6.9 ^{+7.1} _{-6.7} $\times 10^{14}$	[177]	5.1 ^{+5.3} _{-5.0} $\times 10^{14}$	[155]	1.2 ^{+1.9} _{-0.6} $\times 10^{15}$
HCC ¹³ CN	[233]	9.8 ^{+11.0} _{-8.4} $\times 10^{14}$	[177]	7.5 ^{+8.3} _{-6.5} $\times 10^{14}$	[155]	1.4 ^{+2.1} _{-0.6} $\times 10^{15}$
CH ₃ CH ₂ CN	52 ⁺² ₋₁	$\gtrsim 7.3 \times 10^{15}$	51 ⁺² ₋₁	$\gtrsim 4.7 \times 10^{15}$	98 ⁺⁴ ₋₄	8.4 ^{+8.7} _{-8.2} $\times 10^{15}$
CH ₂ CHCN	[52]	1.5 ^{+1.6} _{-1.4} $\times 10^{15}$	[51]	2.2 ^{+2.2} _{-2.1} $\times 10^{15}$	129 ⁺⁶ ₋₆	3.9 ^{+4.0} _{-3.8} $\times 10^{15}$
$v_{11} = 1$	[129]	4.7 ^{+5.5} _{-3.8} $\times 10^{16}$
CH ₂ NH	139 ⁺¹³ ₋₁₁	$\gtrsim 1.6 \times 10^{15}$	75 ⁺⁹ ₋₆	$\gtrsim 1.1 \times 10^{15}$	[138]	1.0 ^{+1.7} _{-0.5} $\times 10^{15}$
HNCO	179 ⁺⁸ ₋₆	$\gtrsim 1.6 \times 10^{16}$	167 ⁺⁷ ₋₇	$\gtrsim 1.7 \times 10^{16}$	[138]	1.1 ^{+1.7} _{-0.7} $\times 10^{17}$
CCH	[212]	$\gtrsim 1.6 \times 10^{15}$	[228]	1.8 ^{+2.7} _{-1.1} $\times 10^{15}$	[71]	$\gtrsim 6.4 \times 10^{14}$	[62]	$\gtrsim 2.4 \times 10^{14}$
c-C ₃ H ₂	[212]	3.8 ^{+4.2} _{-3.5} $\times 10^{15}$	[228]	5.6 ^{+6.2} _{-5.0} $\times 10^{15}$
C ₄ H	[155]	1.1 ^{+1.1} _{-1.0} $\times 10^{15}$

NOTE—Column densities derived from species whose median line optical depth exceeds 0.5 are indicated by \gtrsim , as are those derived for molecules which only had transitions in the lower-resolution, high-frequency data of G20. These should collectively be treated as lower limits. Adopted rotational temperatures are indicated by brackets. Labels for the vibrational states correspond to the molecule listed immediately above.

^a Column densities computed from minor isotopologues when available assuming the appropriate isotopic elemental ratios (see Appendix E).

Each of our sources has previous estimates of rotational temperature and column density in at least a handful of the same molecules considered here (e.g., CH₃CN, CH₃OH, SO₂, H₂S). Our derived values are generally consistent with these prior inferences in G20 (Galván-Madrid et al. 2009; Xu & Wang 2013) and G35 (Zhang et al. 2014), which both used substantially lower resolution (a few arcseconds) SMA data, as well as those derived from high-resolution ($\approx 0''.2$) ALMA observations in G28 (Gorai et al. 2024).

5. DISCUSSION

5.1. Chemical Richness and Evolutionary Stage

In high-mass star-forming regions, the observed chemistry varies as a function of evolutionary stage (e.g., Sanhueza et al. 2012; Gerner et al. 2014, 2015; Liu et al. 2021). Molecular complexity initially increases starting from the infrared dark cloud phase until the emergence of a hot core, where the molecular abundance, complexity, and detection rate tends to peak. Once more evolved H II regions are formed, however, this detection rate then again decreases, as powerful stellar radiation destroys many molecular species.

Our sample follows these previously observed trends, which indicates that their relative chemical richness is consistent with an evolutionary sequence. G28 and G20 are the youngest regions with known HMCs and HC H II regions, followed by the UC H II regions in G35 and then the evolved H II region W33, which shows the most advanced signs of star formation in our sample. G28 and G20 are the most chemically-rich with numerous COM detections and consistently show the highest column densities. In contrast, few COMs are detected in G35 with mean column density reductions of one-to-two orders of magnitude. W33 is notably molecule-poor and since it is the only source in our sample categorized as a full H II region, this is likely attributable to much of its molecular material having already been largely destroyed or dispersed. This scenario is further supported by the detection of He α RRLs in only G35 and W33, which indicates that these sources have more massive zero-age-main-sequence stars driving their H II regions due to the larger ionization potential of He compared to H.

Given that our survey sensitivity varies by no more than a factor of five among our sources (Table 3), these discrepancies reflect true chemical and physical differences. Moreover, potential biases in the detection rates due to the different sources distances also cannot explain the observed trends. For instance, W33 is the closest source at 2.4 kpc but shows the fewest molecular detec-

tions, while G20, the furthest source at 12.3 kpc, shows a molecule-rich spectra.

5.2. Spatial Distribution of Molecular Families

5.2.1. Evidence for Carbon Grain Sublimation in G28

Spatial offsets between N- and O-bearing COMs are commonly observed in massive star-forming regions. Orion KL is the prototypical example, where the N-COMs peak at the hot core and the O-COMs are associated with the compact ridge (e.g., Blake et al. 1987; Friedel & Snyder 2008). Subsequent observations of larger samples show that N-COMs typically peak at the location of continuum maxima, while the O-COMs are offset from the location of the central protostar (e.g., Jiménez-Serra et al. 2012; Fayolle et al. 2015; Allen et al. 2017; Bøgelund et al. 2019; Csengeri et al. 2019). While the exact origins of these separations remains unclear, one explanation is the sublimation of refractory carbon grains within the so-called “soot line” at ~ 300 K near the central protostar (van ’t Hoff et al. 2020). This mechanism predicts that N-COMs will be located close to the warmest molecular gas, i.e., within the soot line, and thus have higher rotational temperatures than those of the O-COMs, which are desorbed uniformly within the water snowline (~ 100 K). Here, we aim to see if such a scenario is operating in any of sources in our sample.

G28 is the only source in our sample that shows significant spatial offsets between N- and O-bearing species. As shown in Figure 9, N-bearing molecules are located at the continuum peak while the O-bearing molecules are offset at either the HMC1 or HMC2 positions. Moreover, the RRLs, which trace the hottest gas, also peak at the continuum position (see Figure 1). We also compiled all derived rotational temperatures for both N- and O-bearing molecules in Figure 11. In G28, the N-bearing molecules potentially show warmer rotational temperatures than those of that are O-bearing, with median temperatures of ≈ 210 K and ≈ 140 K, respectively. This trend is primarily driven by the especially warm temperatures of H¹³CCCN, HC₃N, $v_7 = 1$, and ¹³CH₃CN. Although we derive T_{rot} values for the N-bearing molecules that are less than 300 K, as predicted for grain sublimation, this is likely due to a beam dilution effect. At the resolution of our observations, most molecular emission is likely at least partially beam diluted and thus, it is the difference, rather the absolute values, of the rotational temperatures that points to potential carbon grain sublimation. Specifically, the hottest gas will be within the soot line, which is at least an order of magnitude more compact than the water snowline. Thus, we expect the N-COMs to be more severely affected by beam dilution, and the fact that we still measure warmer T_{rot} val-

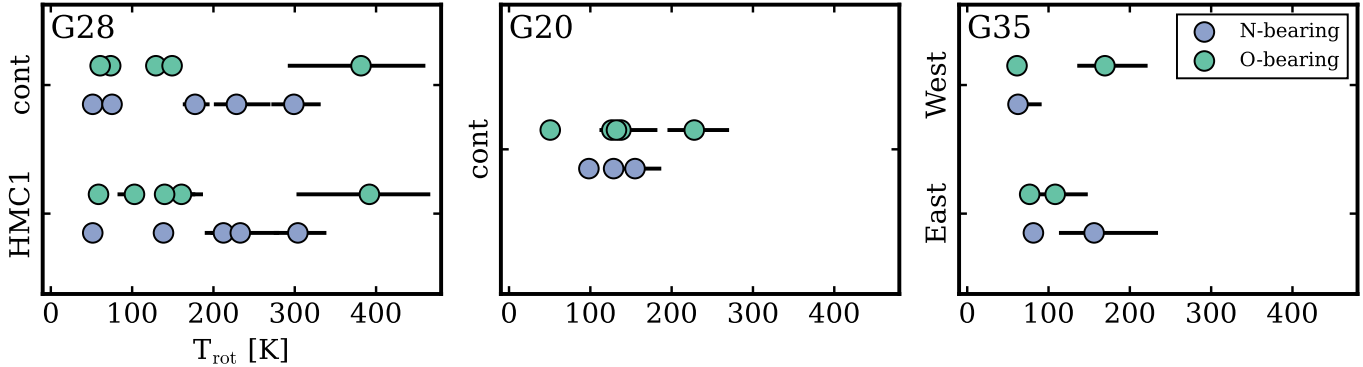


Figure 11. Derived rotational temperatures of O-bearing (green) and N-bearing (blue) species in our sample. Molecules containing both N and O, i.e., HNC and NH_2CHO , are excluded.

ues for a handful of N-bearing species implies a reservoir of even hotter gas. Further evidence of beam dilution is supported by the results of [Gorai et al. \(2024\)](#), who infer excitation temperatures³ of ~ 300 K and ~ 250 K for HMC1 and HMC2, respectively, in ALMA observations of G28 in a $0''.2$ beam. Taken together, carbon grain sublimation provides a plausible explanation for the observed spatial offsets and T_{rot} distributions of N- and O-bearing molecules in G28.

We cannot assess if a similar scenario is operating in the other sources in our sample. We do not detect a sufficient number of molecules in G35 or W33 to meaningfully compare relative spatial distributions. Due to the far distance of G20, we lack the effective spatial resolution to observe comparable separations (a few 1000 au) as were seen in G28. We also expect much more significant beam dilution in G20, making it difficult to properly interpret the T_{rot} distributions in Figure 11 without additional high-angular resolution observations.

5.2.2. An Elemental Oxygen Gradient in G35

While we do not observe any clear spatial separations among O-, N-, and S-bearing species in G35 in Figure 9, we do identify a broad spatial difference between those molecules containing oxygen versus those lacking oxygen. We demonstrate this difference in Figure 12, where we compute the radial distance of all detected molecules from a position between G35 East and West. The majority of molecules that contain oxygen are clustered at small radial distances (< 0.3 pc), while those that do not are located at larger distances (≈ 0.4 - 0.8 pc). These spatial offsets suggest the presence of a gas-phase ele-

mental oxygen gradient across G35 where the regions close to G35 East and West are oxygen-rich and those at further distances are oxygen-poor. As noted in the previous Section, we are not able to probe the innermost regions (a few 1000 au) around the UC H II regions in G35, where we might expect carbon grain sublimation to perhaps boost the gas-phase C/O ratio on small scales, as illustrated in Figure 12.

A possible explanation for the observed C/O gradient is vigorous thermal sublimation of O-rich ices, i.e., water ice, due to high gas temperatures near one or both of the central UC H II regions, which, in turn, triggered the formation of abundant O-rich species in the gas-phase (e.g., [Bergin et al. 1998](#); [Fraser et al. 2001](#); [Rodgers & Charnley 2003](#); [Bjerkeli et al. 2016](#); [van Dishoeck et al. 2021](#)). For instance, chemical modeling predicts that sudden ice evaporation induced by protostellar accretion bursts can form O-bearing organic molecules ([Taquet et al. 2016](#)). This scenario is also consistent with the detection of gas-phase HDO in this inner 0.3 pc region (Figure 8). Similar trends have been seen in protostellar envelopes ([van't Hoff et al. 2022](#)), disks around young eruptive stars ([Tobin et al. 2023](#); [Lee et al. 2024](#)) and massive star-forming regions (e.g., [McGuire et al. 2018](#); [Csengeri et al. 2019](#)), where gas-phase emission from HDO and O-rich COMs show similar spatial distributions. At larger distances, the temperatures are cooler and freeze-out timescales quicker, so the outermost regions would be the first regions where O-rich molecules have already begun freezing out.

If we assume that the transition zone between O-rich and O-poor molecules corresponds to the water snowline at ≈ 0.3 pc, this would require a luminosity increase of ~ 20 - $60\times$ the current G35 luminosity, adopting typical dust temperatures and gas densities of massive star-forming regions (e.g., [Bisschop et al. 2007](#); [van't Hoff et al. 2022](#)). We can also approximately estimate the re-freeze-out timescale for water, which is on the order of a

³ Due to the smaller bandwidth of the ALMA observations, [Gorai et al. \(2024\)](#) are not able to derive rotational temperatures on a per-molecule basis. Instead, they adopt a single excitation temperature at each position that well-reproduces several high excitation ($E_{\text{u}} \approx 350$ - 500 K) transitions of HNC, $^{13}\text{CH}_3\text{CN}$, and CH_3OCHO .

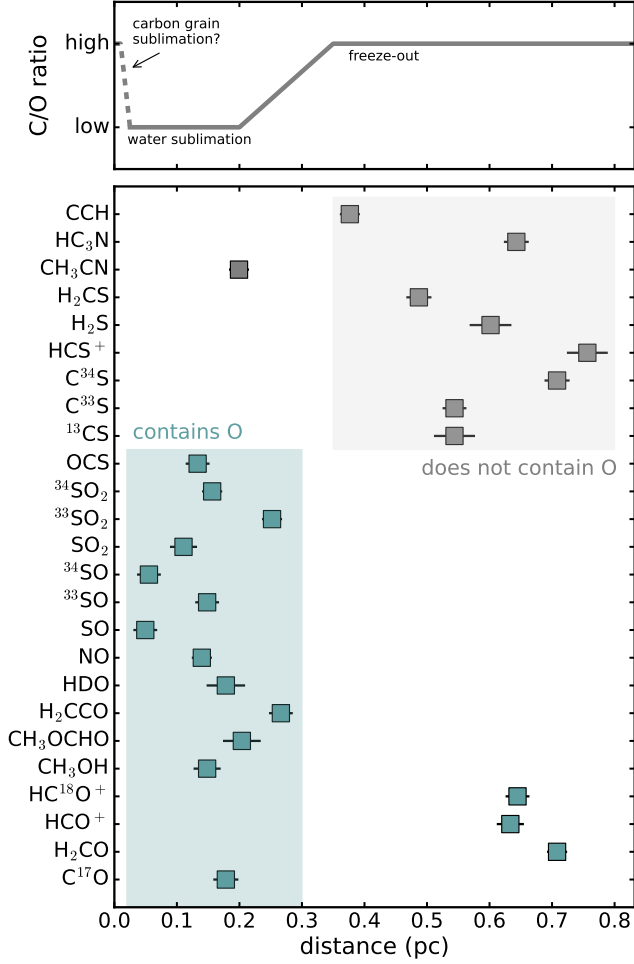


Figure 12. Schematic of expected gas-phase C/O ratios (*top*) and projected radial distance of molecular line peaks measured in G35 (*bottom*). Molecules containing oxygen are shown in green and those without are colored in gray.

few thousands years (Visser et al. 2012). This suggests a relatively recent event, such as an outburst, would be needed to drive this temporary luminosity increase. This scenario does not fully explain the relatively high detection rate of S-bearing molecules, relative to the O- or N-bearing molecules, in this source. This may be due to either an intrinsically rich sulfur chemistry in G35 or could point to an additional mechanism, e.g., shocks, outflows, outbursts, driving additional S-chemistry (e.g., Pineau des Forets et al. 1993; Gusdorf et al. 2008; Liu et al. 2012; Minh et al. 2016; Townner et al. 2024). Although beyond the scope of this work, detailed chemical and physical modeling of G35 is required to verify the origins of these observed chemical trends.

5.3. Chemical Origins of COMs

COM column density ratios have often been used to gain insight into their formation mechanisms (e.g., Biss-

chop et al. 2007; Fontani et al. 2007; Fayolle et al. 2015; Law et al. 2021; Nazari et al. 2023). Recent surveys have identified nearly constant COM abundance ratios in sources across a wide range of bolometric luminosities, including in both high- and low-mass protostars (Coletta et al. 2020; van Gelder et al. 2020; Nazari et al. 2022; Chen et al. 2023), which suggests that COM abundances are likely set during the earlier, cold pre-stellar phases. For this to be the case, complex organics, or their precursors, must share a common formation environment, i.e., on pre-stellar ices. Detections of multiple COMs in pre-stellar cores (e.g., Vastel et al. 2014; Scibelli et al. 2021) and on ices (McClure et al. 2023) lends further support to such an interpretation. Here, we compare column density ratios of several O-, N-, and S-bearing species in our sample to those derived in the literature to see if such a scenario is compatible with our observations.

Figure 13 shows column density ratios for a select set of molecules. Specifically, we chose a variety of O- and N-COMs, which are thought to be chemically related, e.g., CH₃OH/CH₃OCH₃/CH₃OCHO (e.g., Garrod & Herbst 2006; Balucani et al. 2015) or HNCO/NH₂CHO (e.g., López-Sepulcre et al. 2015; Quénard et al. 2018), or have previous observational evidence of correlations, e.g., CH₃OH/CH₃CN (Gieser et al. 2021; Law et al. 2021). We also include several S-bearing molecules in this comparison. The typical 1 σ range in abundance ratios reported in the literature, which are shown as shaded lines in Figure 13, were computed using a sample of both high- and low-mass protostars (Nazari et al. 2022; Chen et al. 2023), with the exception of the CH₃OCHO/CH₃OCH₃ ratio and those of the S-bearing molecules, which were derived from only high-mass sources (Li et al. 2015; Coletta et al. 2020).

In general, we find remarkably consistent N_{col} ratios across our sample, which are largely in agreement with literature abundance ratios. Among our sample, the largest source-to-source differences ($\approx 30\times$) are those found for the N_{col} ratio of CH₃CN/CH₃OH, but this is perhaps not surprising. While these molecule have shown empirical correlations in prior surveys, there is no known chemical link between them. If we exclude this ratio, then both the O- and N-COM abundance ratios show source-to-source variations of no more than a factor of 5. As can be seen in Figure 13, all of these variations are well within the uncertainties. The S-bearing molecules show modestly higher source-to-source differences, up to a factor of nearly 10, but are again consistent within errors. Moreover, all O- and N-bearing COMs shown in Figure 13 are in agreement with literature abundance ratios, as are the S-bearing species with

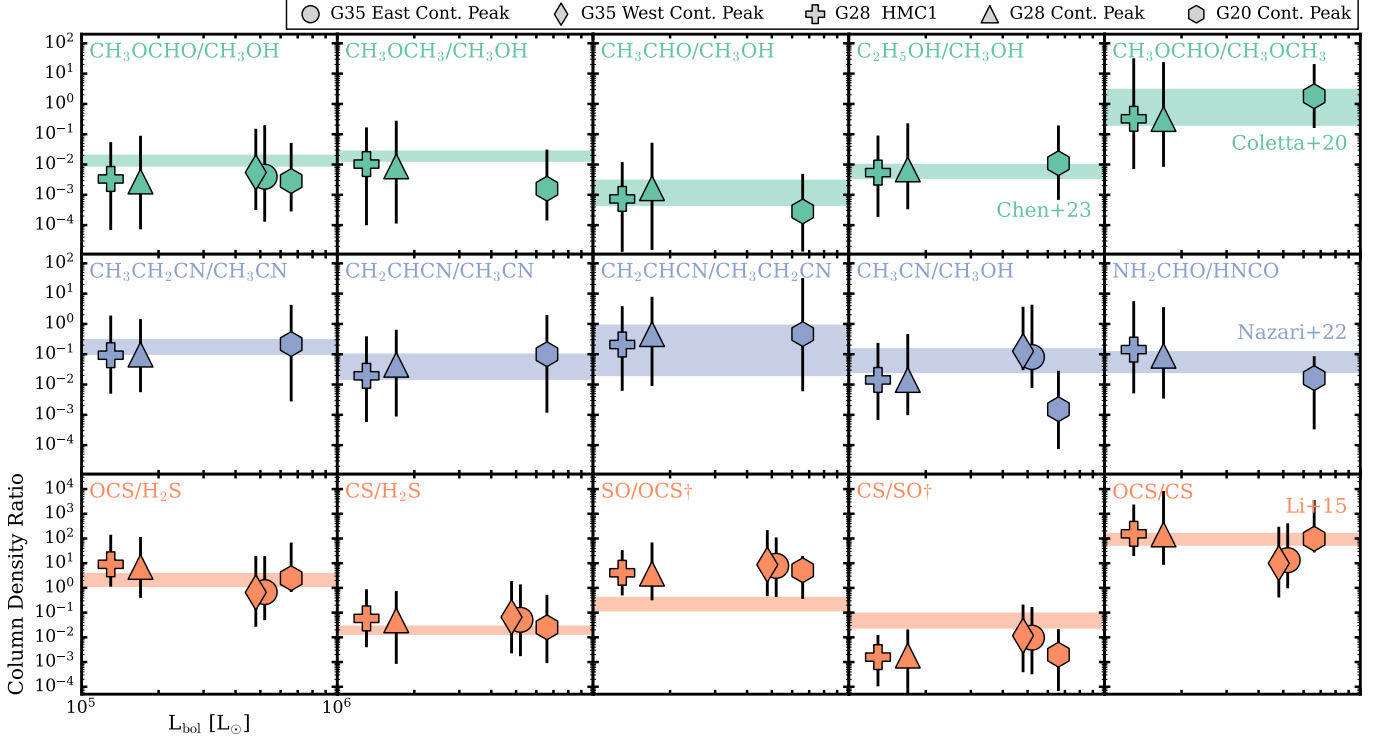


Figure 13. Column density ratios of select molecules (*columns*). Shaded bands correspond to the typical 1σ range of abundance ratios observed in star-forming regions for O-, N-, and S-bearing species (*rows*). Ratios from Nazari et al. (2022); Chen et al. (2023) include a sample of both high- and low-mass protostars, while Li et al. (2015); Coletta et al. (2020) were derived from only high-mass sources. The CS column densities are computed from ^{13}C S, assuming the relevant isotopic elemental ratios (Yan et al. 2023). The ratios marked by a † symbol indicate those derived using likely optically-thick SO. Bolometric luminosity uncertainties are on the order of $\approx 30\text{-}50\%$ (Wood & Churchwell 1989; Liu et al. 2019b; Law et al. 2022). Molecules are colored as in Figure 4.

the exception of the SO/OCS and CS/SO N_{col} ratios. The consistent discrepancies related to the SO abundance in all sources, namely, an elevated SO/OCS and lower-than-expected CS/SO ratio relative to the trends from Li et al. (2015), is likely an optical depth effect. The SO column densities reported in Li et al. (2015) were derived using a single transition, but SO is typically optically thick in massive star-forming regions and these values are likely underestimated. Since we cover multiple lines of the ^{33}SO and ^{34}SO isotopologues, we are able to derive more robust column densities based on optically-thin lines. Thus, overall, the nearly constant N_{col} ratios measured in our sample support the notion that COM abundances must share similar formation environments.

6. CONCLUSIONS

We present a wideband (≈ 32 GHz) chemical survey of four massive star-forming regions with the SMA at sub-arcsecond angular resolution. We conclude the following:

1. We establish a comprehensive molecular inventory of all sources and identify over 60 molecules, including numerous COMs and isotopologues. We also detect several bright RRLs, indicating the presence of ionized gas.
2. The sources in our sample demonstrate a wide range of chemical richness that is consistent with an evolutionary sequence from the line-rich hot cores and HC H II regions of G28 and G20 to the more chemically-modest UC H II regions in G35, followed by the molecule-poor H II region W33.
3. Our sample shows complex, often molecule-specific, emission morphologies on multiple spatial scales from several 1000 au up to ~ 1 pc. In all sources, we identify diffuse, extended emission, indicating outflow-induced chemistry, as well as compact emission components that are driven by hot, gas-phase chemistry near the central protostars. Mutual spatial offsets among O-, N-, and S-bearing molecules and the millimeter continuum are observed in all four massive star-forming regions.

4. We compute rotational temperatures and column densities for a large number of molecules at a few positions of interest in G28, G20, and G35. The inclusion of multiple isotopologues and lines with a wide range of excitation conditions in our observations enable robust estimates on the gas physical properties.
5. We find potential evidence for carbon grain sublimation around the central protostar in G28. N-bearing molecules are co-located with the continuum and RRL peaks and have systemically warmer rotational temperatures (≈ 210 K), while O-bearing species are spatially offset and have lower rotational temperatures (≈ 140 K).
6. We also find evidence of an elemental oxygen gradient in G35, with an O-rich environment close to the two central UC H II regions and an O-poor chemistry at larger radii. One possible explanation for this gradient is vigorous thermal sublimation of nearby O-rich ices, i.e., water ice, due to high gas temperatures while at larger radii, freeze-out has already halted much of the gas-phase O-chemistry. G35 also hosts a relatively rich S-chemistry, which may be intrinsic or could point to an additional dynamical mechanism, e.g., shocks, outflows, outbursts.
7. We observe remarkably constant COM abundance ratios among our sources that agree with literature values in other low- and high-mass protostars. Overall, our sample supports the idea that COM

formation occurs in similar environments during the earlier pre-stellar phases, i.e., likely in ices.

The authors thank the anonymous referee for valuable comments that improved both the content and presentation of this work. The authors wish to recognize and acknowledge the very significant cultural role and reverence that the summit of Maunakea has always had within the indigenous Hawaiian community. We are most fortunate to have had the opportunity to conduct observations from this mountain.

Support for C.J.L. was provided by NASA through the NASA Hubble Fellowship grant No. HST-HF2-51535.001-A awarded by the Space Telescope Science Institute, which is operated by the Association of Universities for Research in Astronomy, Inc., for NASA, under contract NAS5-26555. H.B.L. is supported by the National Science and Technology Council (NSTC) of Taiwan (Grant Nos. 111-2112-M-110-022-MY3). L.I.C. acknowledges support from NASA ATP 80NSSC20K0529. R.G.M. acknowledges support from UNAM-PAPIIT project IN108822 and from CONACyT Ciencia de Frontera project ID 86372.

Facilities: SMA

Software: Astropy (Astropy Collaboration et al. 2013; Price-Whelan et al. 2018; Astropy Collaboration et al. 2022), `bettermoments` (Teague & Foreman-Mackey 2018), CASA (McMullin et al. 2007; CASA Team et al. 2022), `cmasher` (van der Velden 2020), `emcee` (Foreman-Mackey et al. 2013), Matplotlib (Hunter 2007), MIR (<https://lweb.cfa.harvard.edu/~cqi/mircook.html>), NumPy (van der Walt et al. 2011), SciPy (Virtanen et al. 2020)

APPENDIX

A. LARGE-SCALE EMISSION IN W33 MAIN

Figure 14 provides a gallery of line peak intensity maps for all detected molecules in W33. These maps demonstrate the complex morphology of the continuum and molecular line emission present in the central few 0.1 pc of W33. In addition to the main core (“W33 Main-Central”), we also label the location of the additional cores reported in Immer et al. (2014), i.e., W33 Main-North, W33 Main-West, and W33 Main-South. The spectral extraction positions in Figures 27-30 are indicated by crosses.

B. FULL SPECTRA AND LINE IDENTIFICATION

The full spectra for each source labeled with all detected lines used in this work is shown in Figure Set

15 (Figures 15-30) The spectra for G28 and G20 are extracted at the continuum peak, while G35 shows the spectra of the East UC H II region. In W33, we show spectra extracted from two different positions corresponding to a molecule-rich region and the peak of the RRL emission, which is comparatively molecule-poor (see Figure 14).

C. GALLERY OF ZEROth MOMENT MAPS

We provide zeroth moment map galleries of all detected molecules toward G28 (Figures 31-32), G20 (Figures 33-34), and G35 (Figures 35-36). For ease of visualization, we categorize each molecule as either extended or spatially-compact. In the case of G28, the ring-like

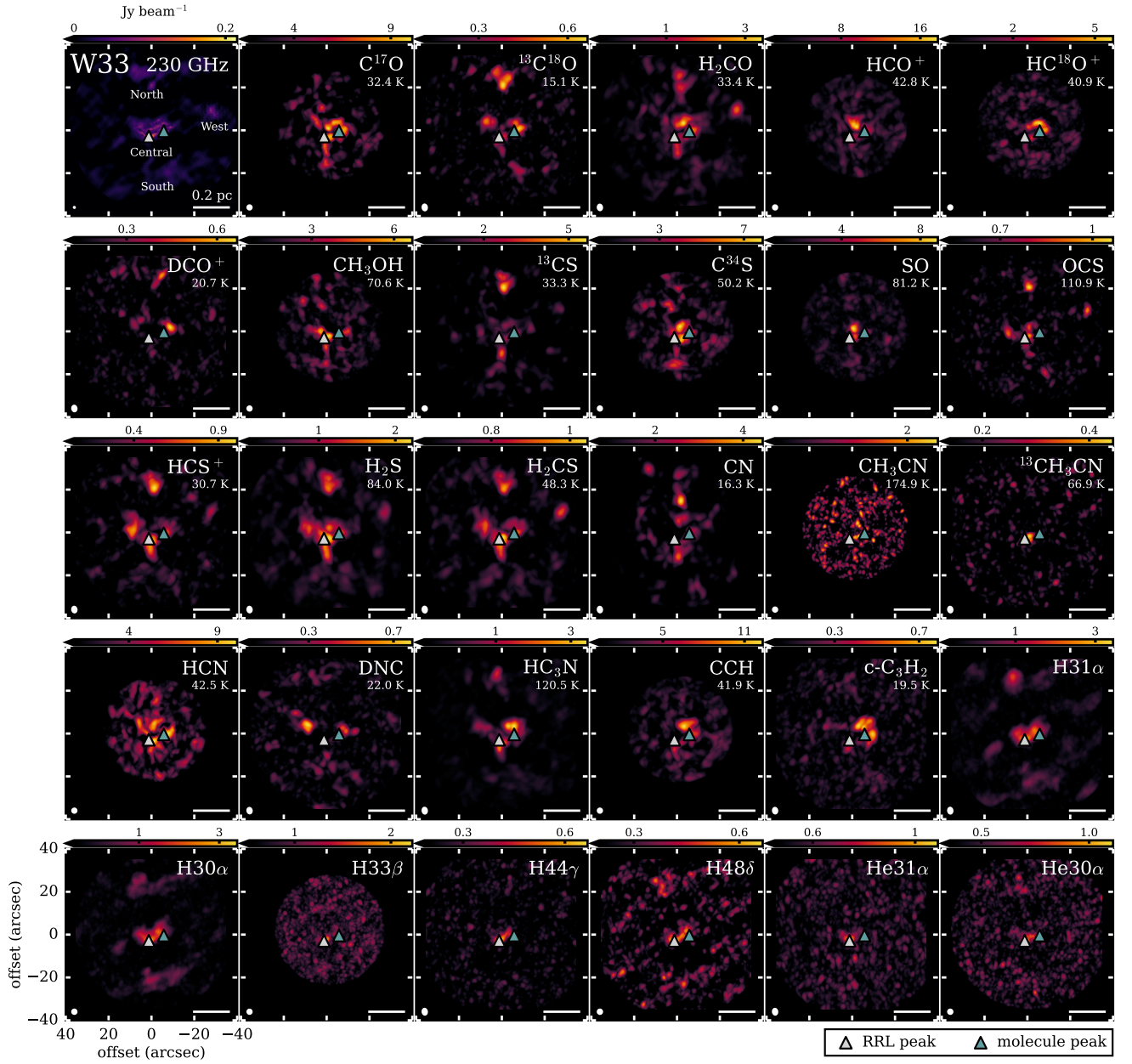


Figure 14. 230 GHz continuum image and gallery of peak line intensity maps of W33 in an extended field of view. The location of the cores (W33 Main-Central, W33 Main-North, W33 Main-West, W33 Main-South) initially identified in Immer et al. (2014) are labeled in the top left panel.

structure, which manifests on intermediate scales, is apparent in molecules in both categories.

D. SPECTROSCOPIC DATA

Table 5 shows a complete set of spectroscopic details for the molecules included in this study. Care was taken to select, when possible, spectroscopic data for partition functions that included any non-negligible contributions from vibrational and torsional states relevant at the high gas temperatures of massive star-forming regions. However, this was not possible for all species and thus, we applied a range of temperature-dependent corrections (C_{vib}) to the derived column densities of the following molecules:

The spectroscopic data for $\text{C}_2\text{H}_5\text{OH}$ is from CDMS and the vibrational correction factor is 2.8 at 300 K (Durig et al. 1975).

The spectroscopic data for NH_2CHO is taken from CDMS and the vibrational correction factor is 1.5 for 300 K (Kryvda et al. 2009; Motiyenko et al. 2012).

The spectroscopic data for OCS, OC^{34}S , and OC^{33}S were obtained from CDMS. For OCS, the vibrational correction factor is 1.2 at 300 K (Saupe et al. 1996; Mürtz et al. 2000). We adopt the same C_{vib} for OC^{34}S , and OC^{33}S .

The spectroscopic data for CH_3CN , $^{13}\text{CH}_3\text{CN}$, and $\text{CH}_3^{13}\text{CN}$ are from CDMS. While the partition function of CH_3CN includes vibrational contributions, those of the isotopologues do not. Thus, we adopt the vibrational correction factor of CH_3CN for $^{13}\text{CH}_3\text{CN}$, and $\text{CH}_3^{13}\text{CN}$, which is 1.5 at 300 K (Bocquet et al. 1988; Tolonen et al. 1993).

The spectroscopic data for H^{15}NC is taken from JPL and we adopt the same vibrational correction factor of HNC, which is 1.5 at 300 K (Burkholder et al. 1987; Maki & Mellau 2001).

The spectroscopic data for HC_3N , H^{13}CCCN , HC^{13}CCN , and HCC^{13}CN are taken from CDMS. The vibrational correction factor for HC_3N is 2.6 at 300 K (Mallinson & Fayt 1976). We adopt the same C_{vib} for H^{13}CCCN , HC^{13}CCN , and HCC^{13}CN .

The spectroscopic data for $\text{CH}_3\text{CH}_2\text{CN}$ was obtained from CDMS. For $\text{CH}_3\text{CH}_2\text{CN}$, the vibrational correction factor ranges 1.1 at 100 K to 3.5 at 300 K Heise et al. (1981).

E. ISOTOPIC RATIOS USED IN THIS WORK

When available, we infer column densities from minor isotopologues to mitigate potential high line optical depths of the main isotopologues. To do so, we use

the following isotope ratios for $^{12}\text{C}/^{13}\text{C}$ (Milam et al. 2005), $^{16}\text{O}/^{18}\text{O}$ (Wilson & Rood 1994), $^{32}\text{S}/^{33}\text{S}$ (Yan et al. 2023), and $^{32}\text{S}/^{34}\text{S}$ (Yu et al. 2020):

$$(^{12}\text{C}/^{13}\text{C}) = (6.21 \pm 1.00)D_{\text{GC}} + (18.71 \pm 7.37) \quad (\text{E1})$$

$$(^{16}\text{O}/^{18}\text{O}) = (58.8 \pm 11.8)D_{\text{GC}} + (37.1 \pm 82.6) \quad (\text{E2})$$

$$(^{32}\text{S}/^{33}\text{S}) = (2.64 \pm 0.77)D_{\text{GC}} + (70.80 \pm 5.57) \quad (\text{E3})$$

$$(^{32}\text{S}/^{34}\text{S}) = (1.56 \pm 0.17)D_{\text{GC}} + (6.75 \pm 1.22). \quad (\text{E4})$$

Table 6 lists the adopted isotopic ratios for each of our sources.

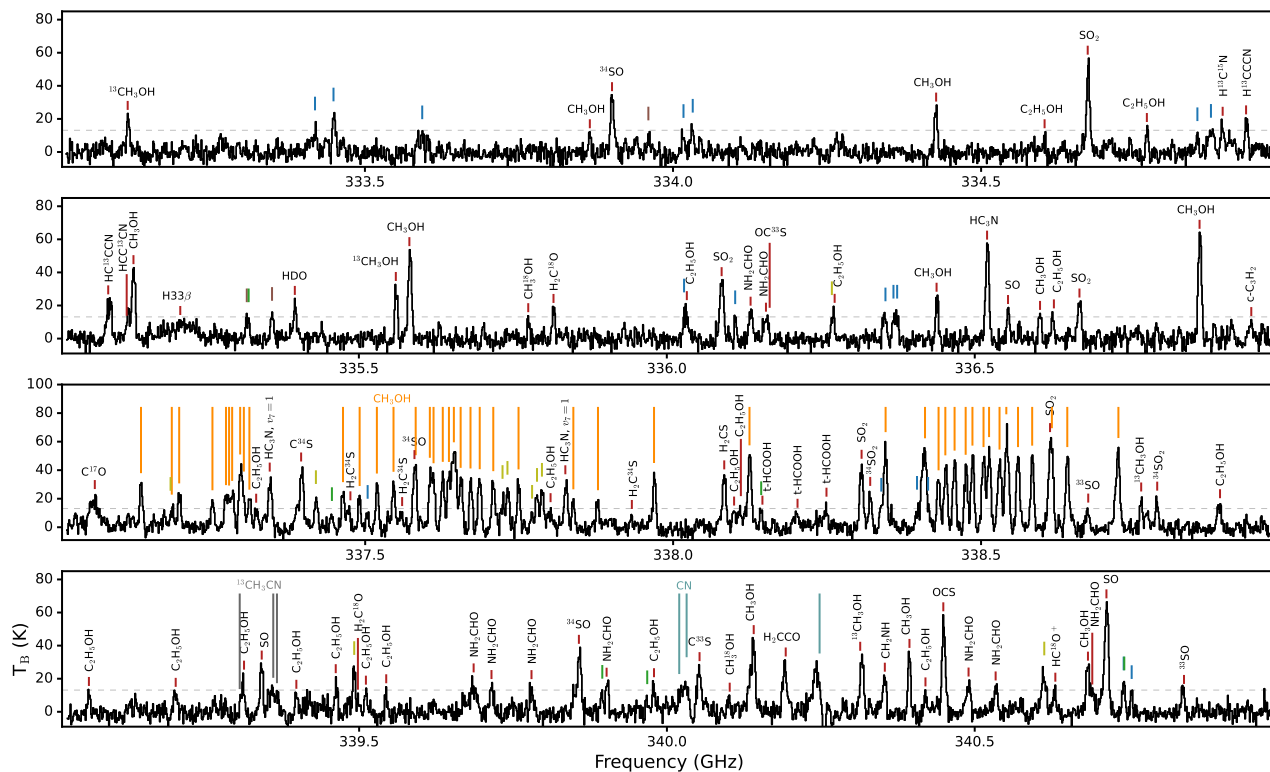


Figure 17. Zoomed-in and labeled SMA spectra of G28 from ≈ 333 -341 GHz. The gray dashed line shows $3\times\text{RMS}$.

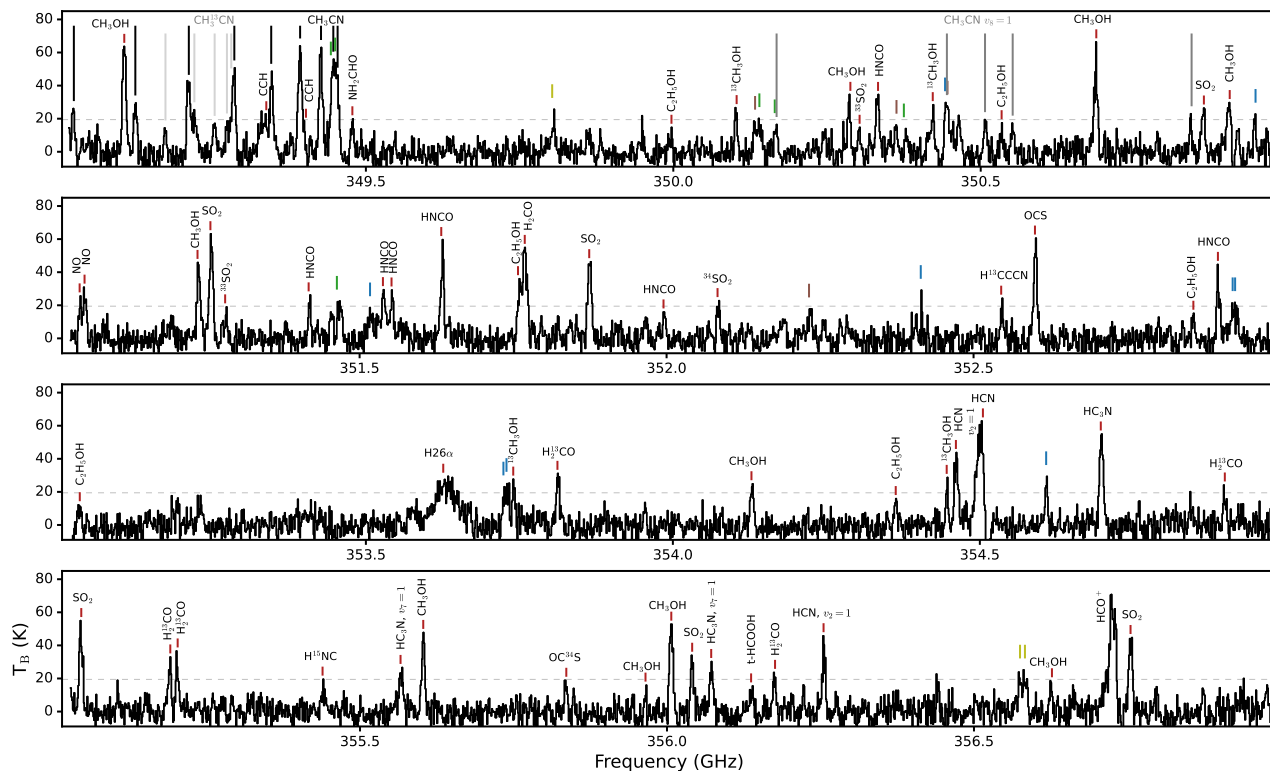


Figure 18. Zoomed-in and labeled SMA spectra of G28 from ≈ 349 -357 GHz. The gray dashed line shows $3\times\text{RMS}$.

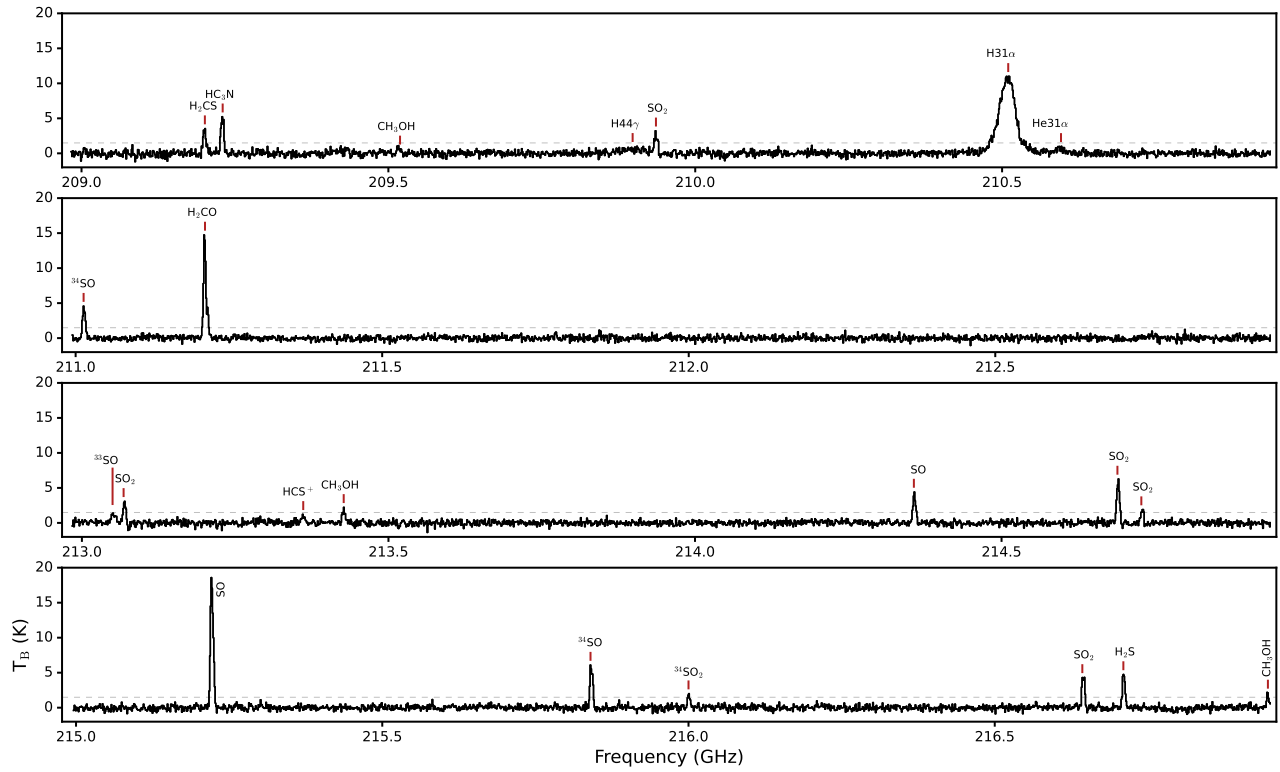


Figure 23. Zoomed-in and labeled SMA spectra of G35 from ≈ 209 -217 GHz. The gray dashed line shows $3\times$ RMS.

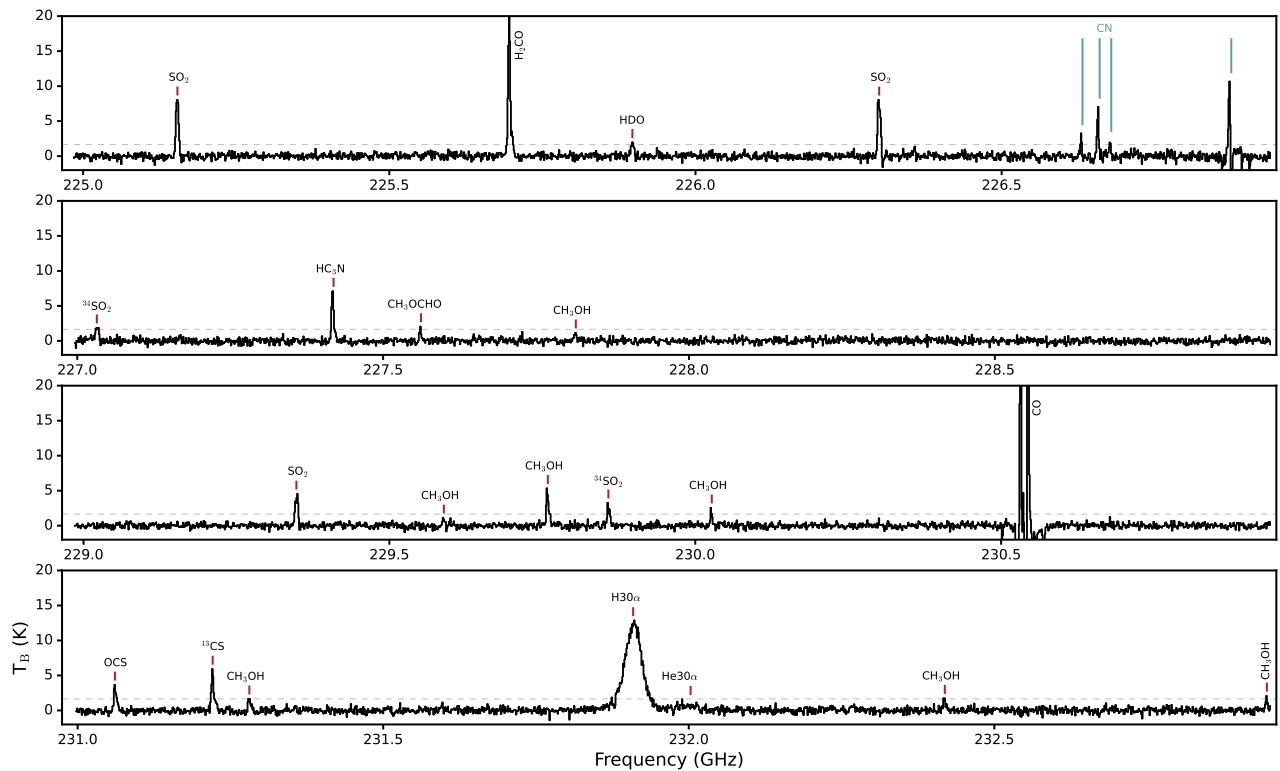


Figure 24. Zoomed-in and labeled SMA spectra of G35 from ≈ 225 -233 GHz. The gray dashed line shows $3\times$ RMS.

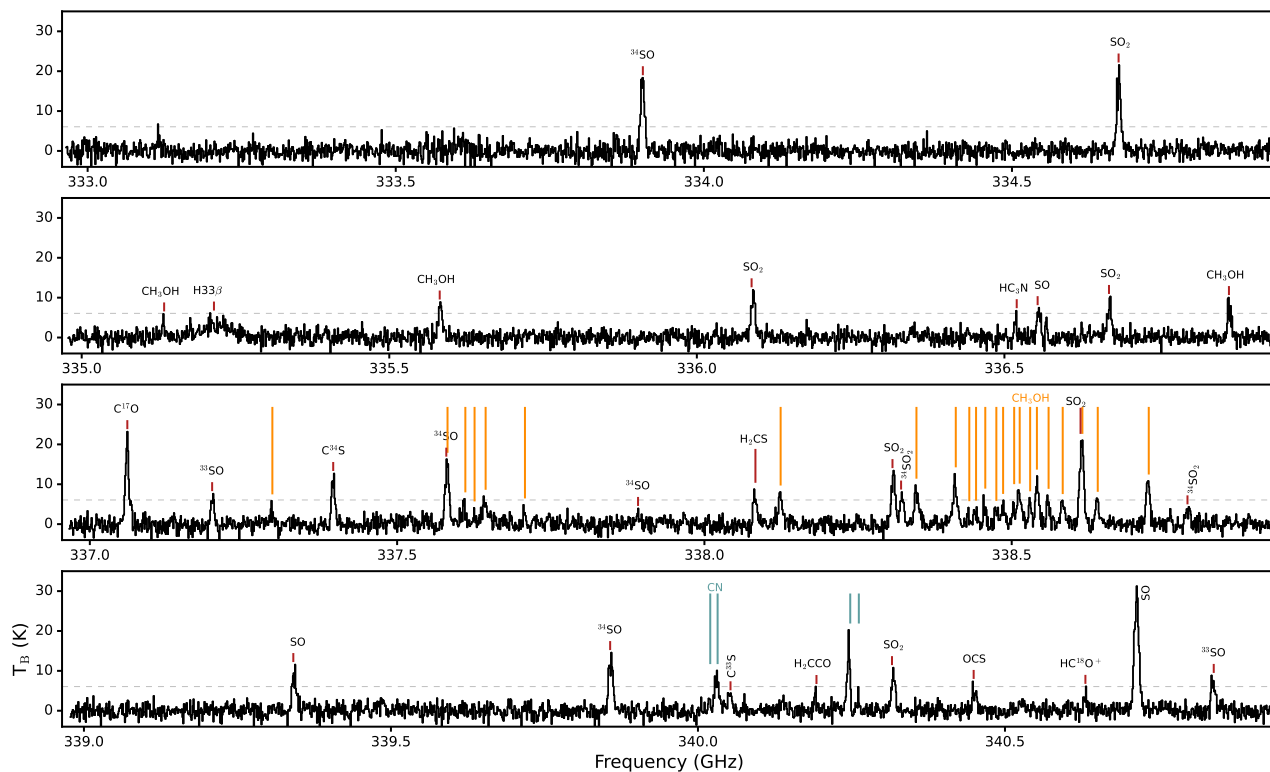


Figure 25. Zoomed-in SMA and labeled spectra of G35 from ≈ 333 -341 GHz. The gray dashed line shows $3\times$ RMS.

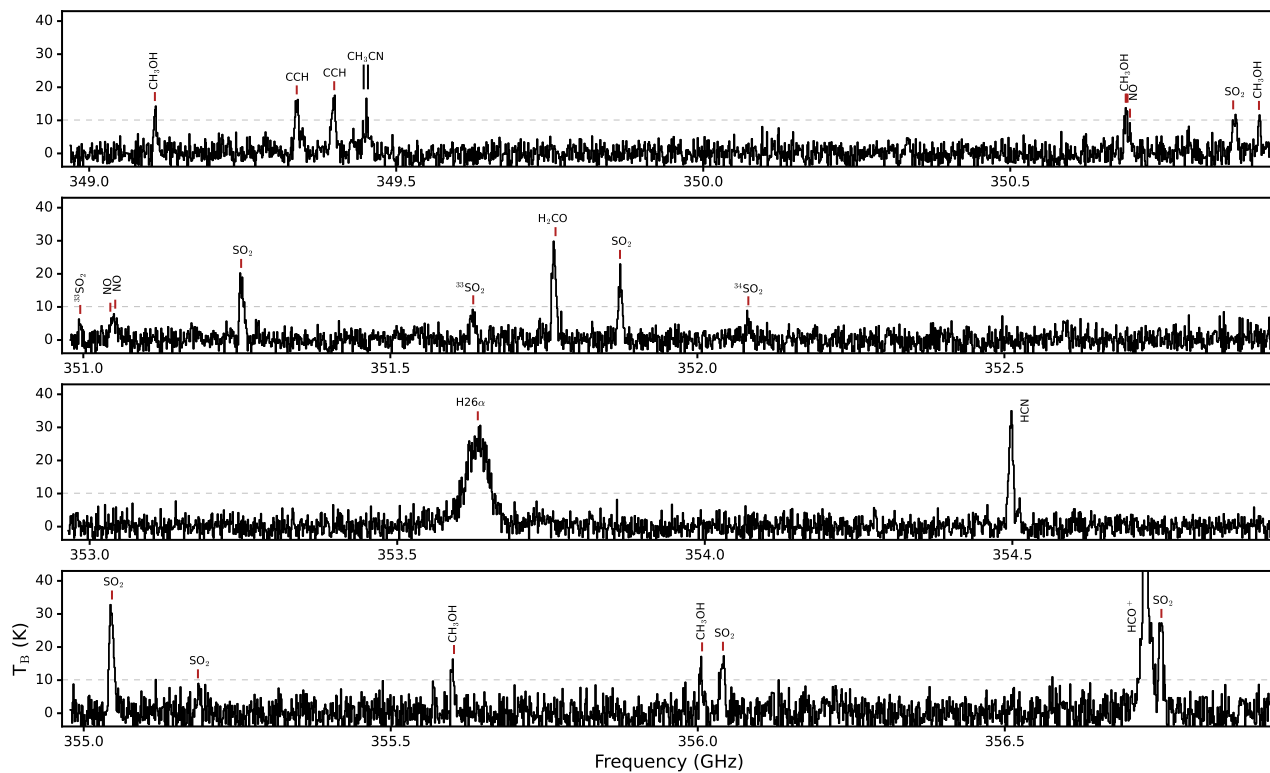


Figure 26. Zoomed-in and labeled SMA spectra of G35 from ≈ 349 -357 GHz. The gray dashed line shows $3\times$ RMS.

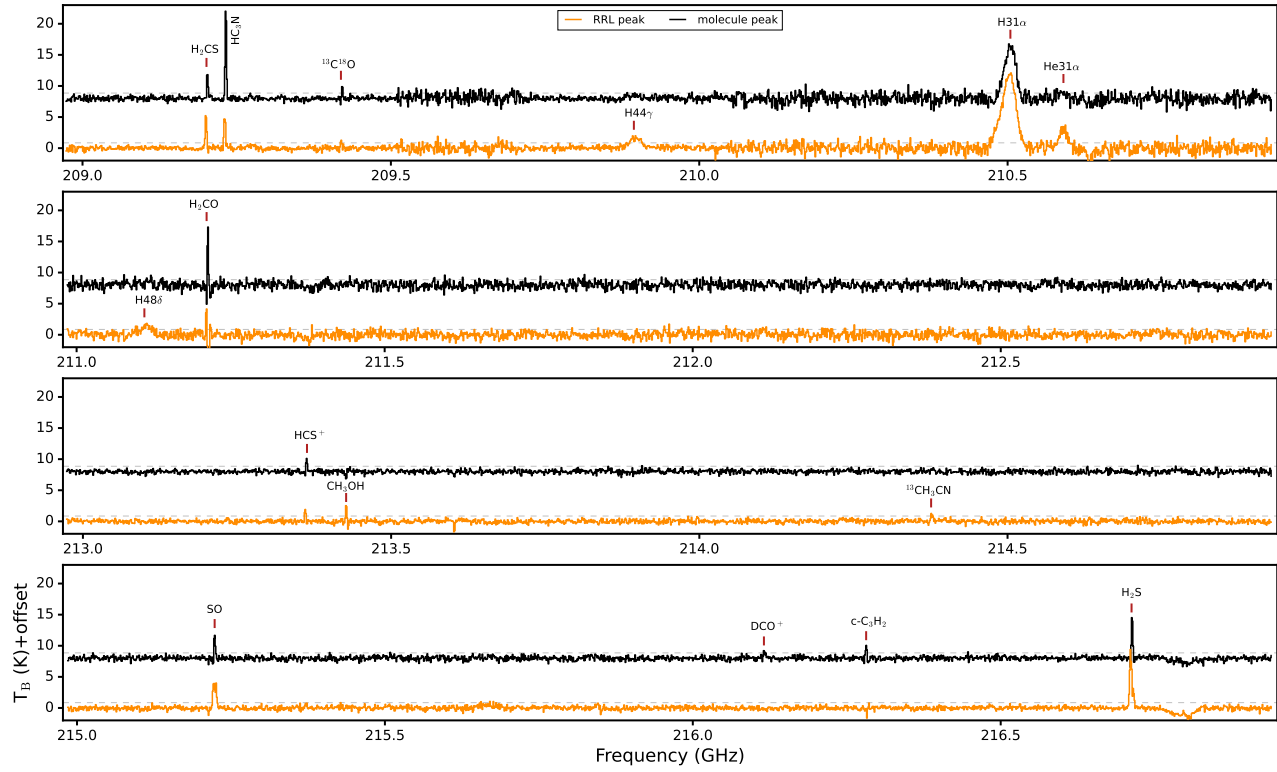


Figure 27. Zoomed-in and labeled SMA spectra of W33 from ≈ 209 -217 GHz. Spectra are vertically offset for visual clarity and the gray dashed lines shows $3\times$ RMS.

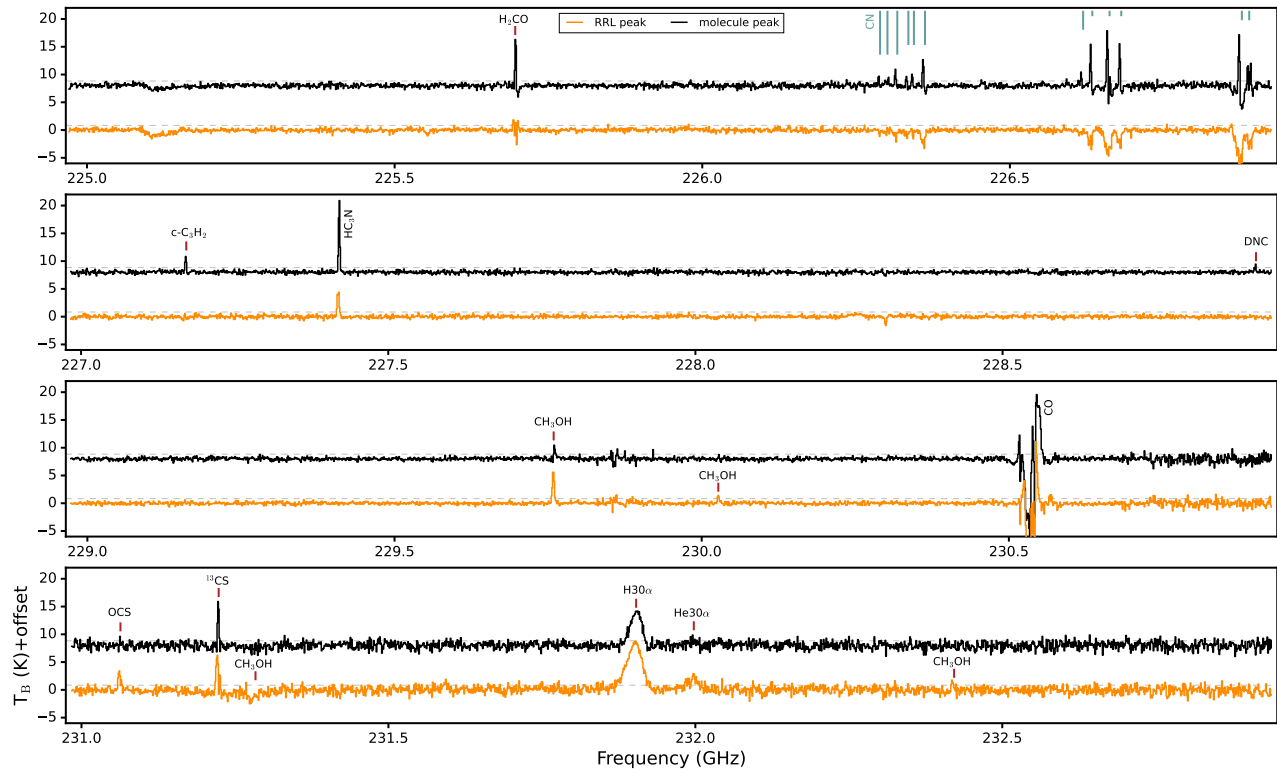


Figure 28. Zoomed-in and labeled SMA spectra of W33 from ≈ 225 -233 GHz. Spectra are vertically offset for visual clarity and the gray dashed lines shows $3\times$ RMS.

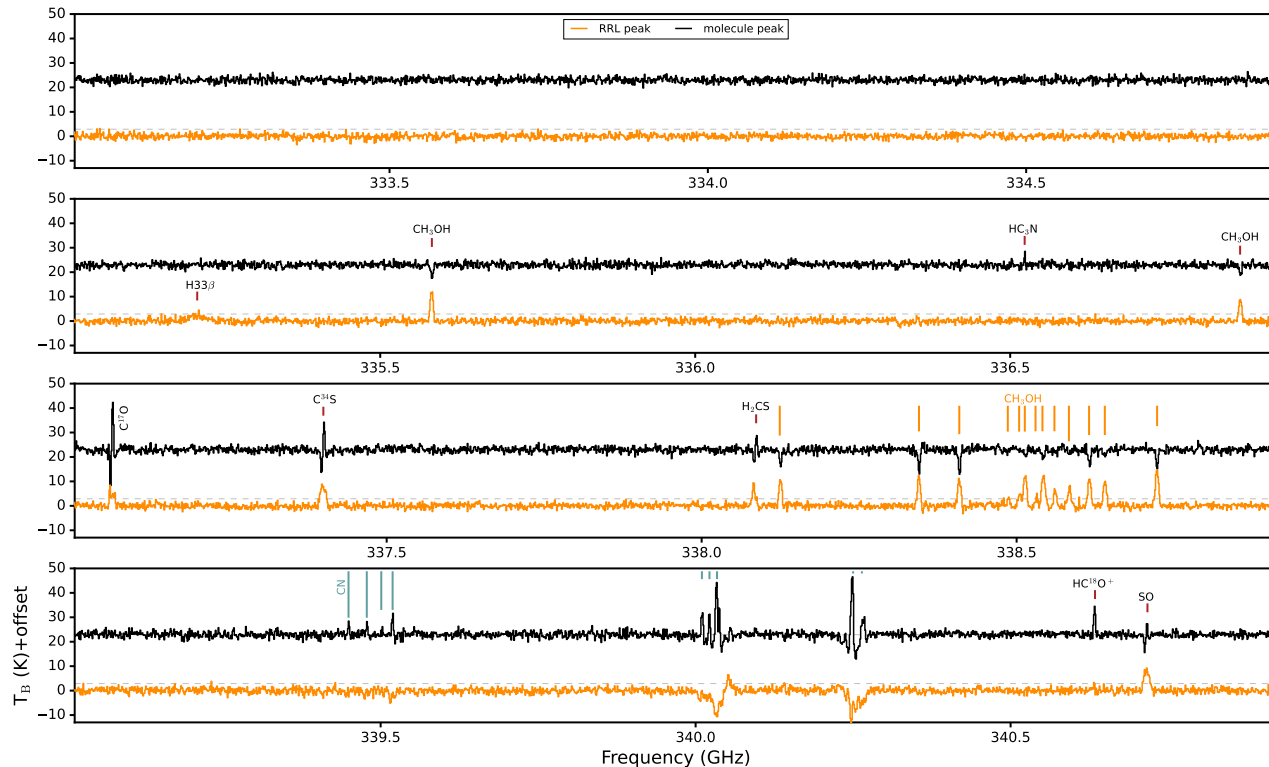


Figure 29. Zoomed-in and labeled SMA spectra of W33 from ≈ 333 -341 GHz. Spectra are vertically offset for visual clarity and the gray dashed lines shows $3\times\text{RMS}$.

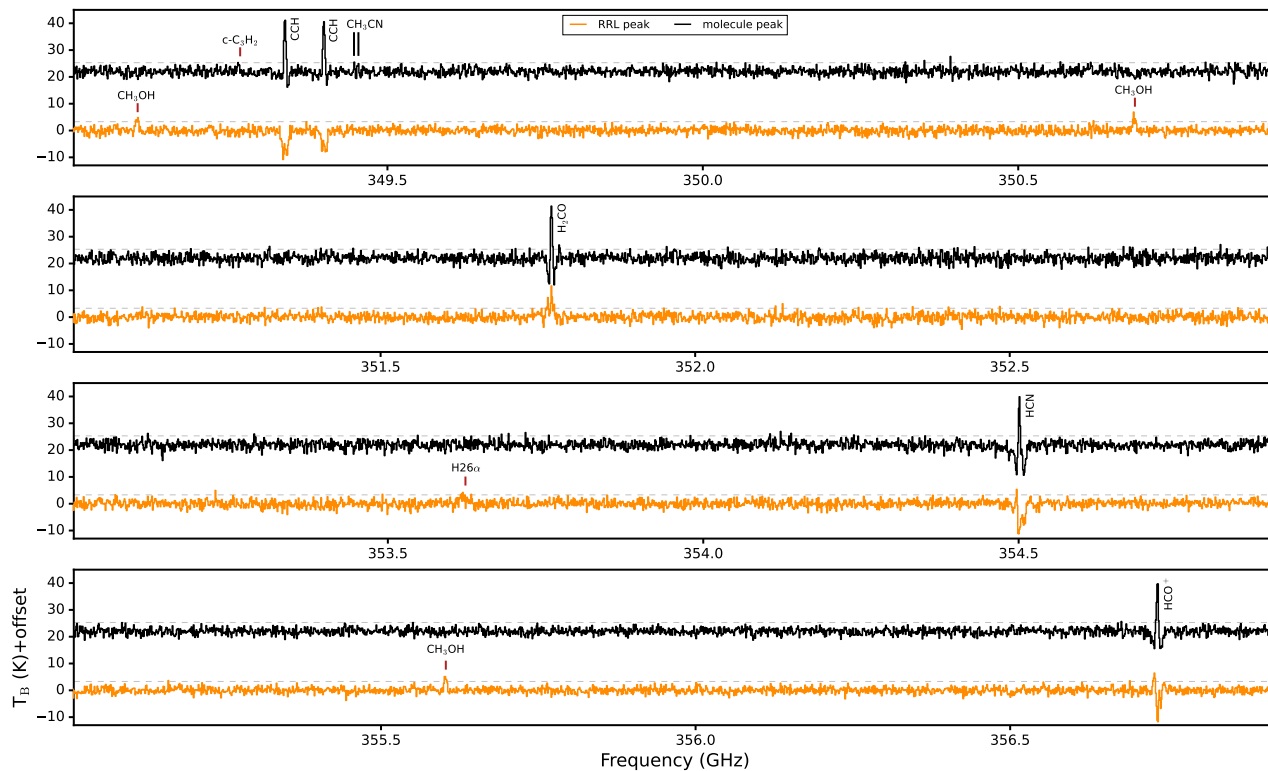


Figure 30. Zoomed-in and labeled SMA spectra of W33 from ≈ 349 -357 GHz. Spectra are vertically offset for visual clarity and the gray dashed lines shows $3\times\text{RMS}$.

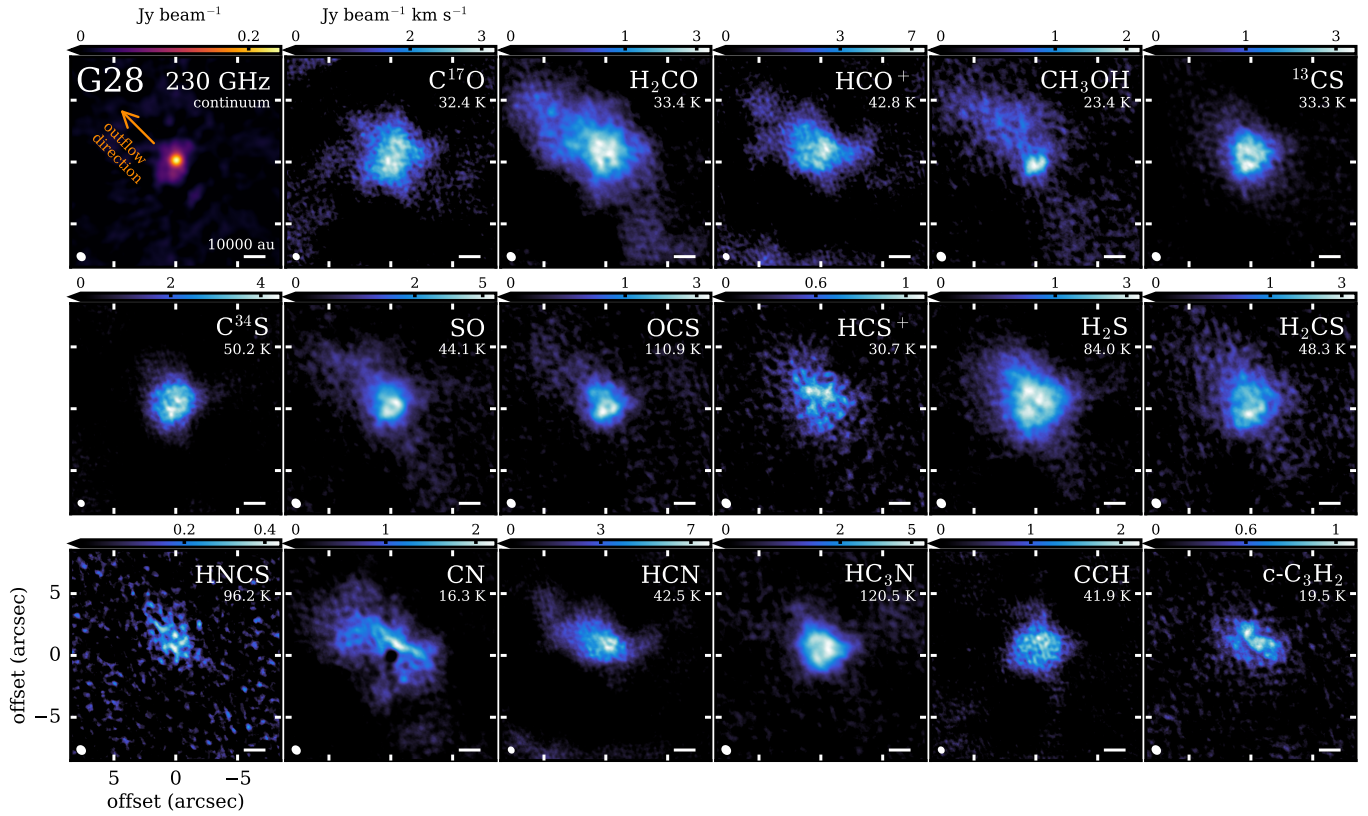


Figure 31. Zeroth moment maps of representative lines of the spatially-extended molecules in G28. The upper state energy of each transition is labeled in the upper right. The synthesized beam and a scale bar indicating 10000 au is shown in the lower left and right corner, respectively, of each panel. The outflow direction, as traced by SiO emission (Gorai et al. 2024), is marked in the continuum image.

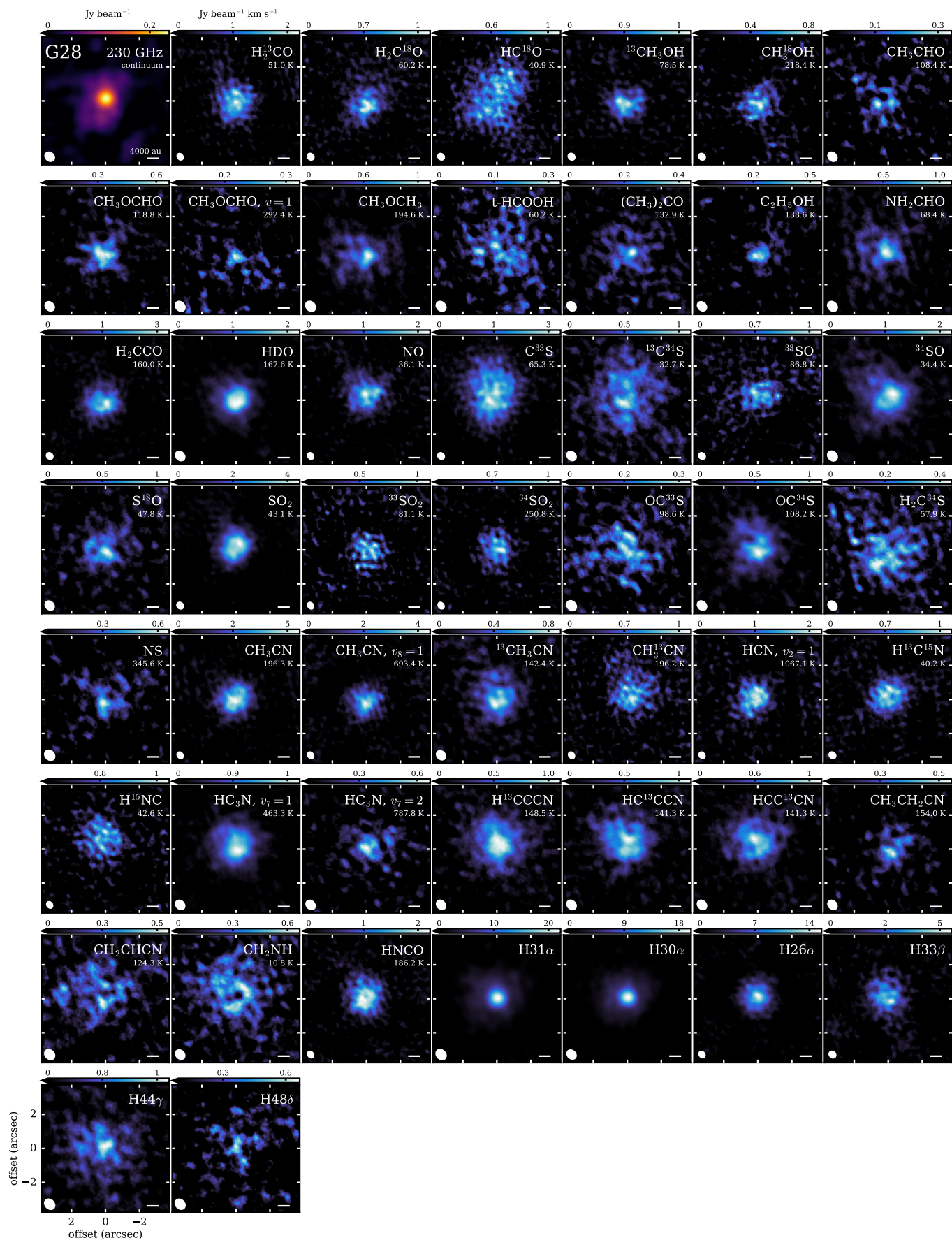


Figure 32. Zeroth moment maps of representative lines of the spatially-compact molecules in G28. The synthesized beam and a scale bar indicating 4000 au is shown in the lower left and right corner, respectively, of each panel.

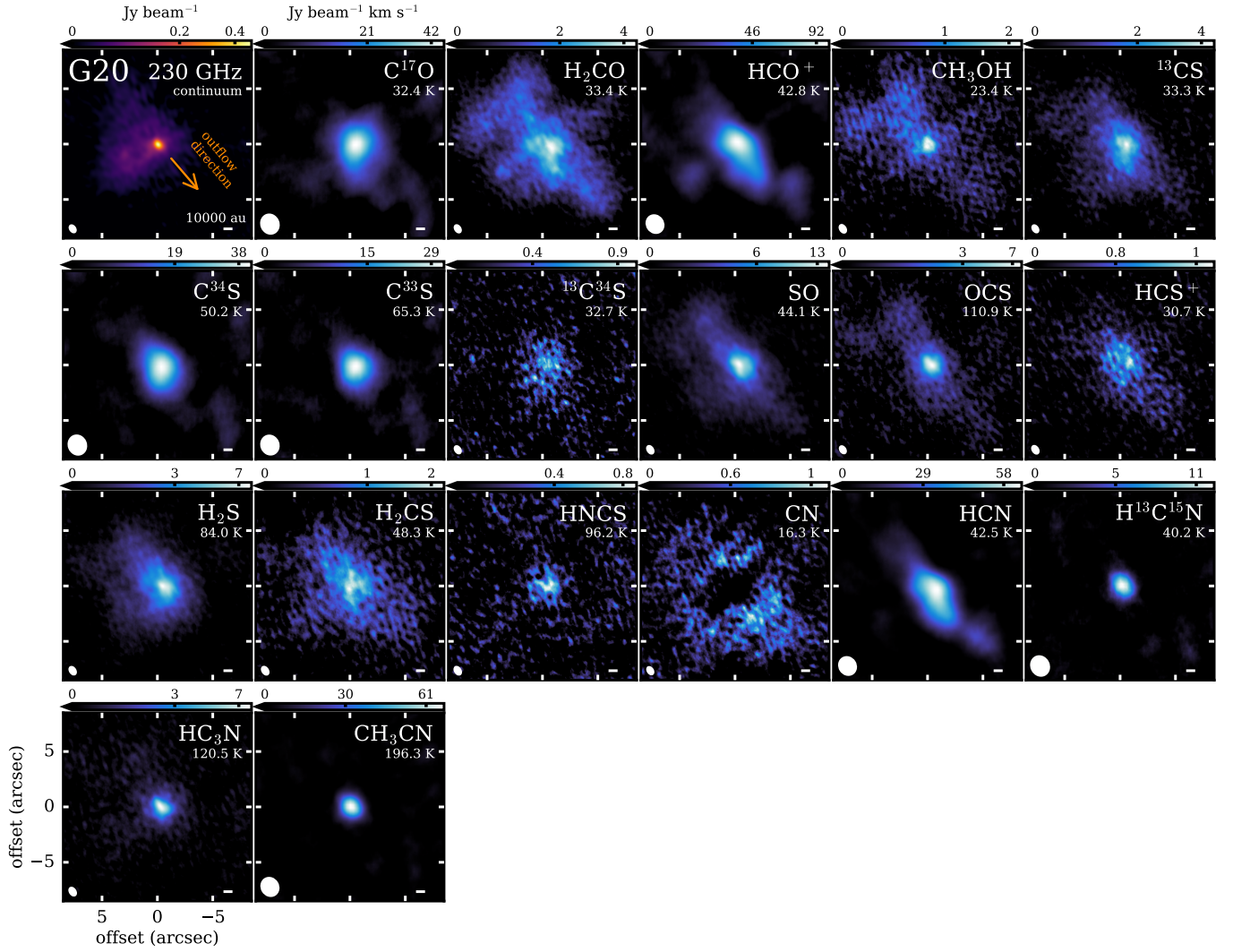


Figure 33. Gallery of spatially-extended lines in G20. The outflow direction, as traced by SiO emission (Xu & Wang 2013), is marked in the continuum image. Otherwise, as in Figure 31.

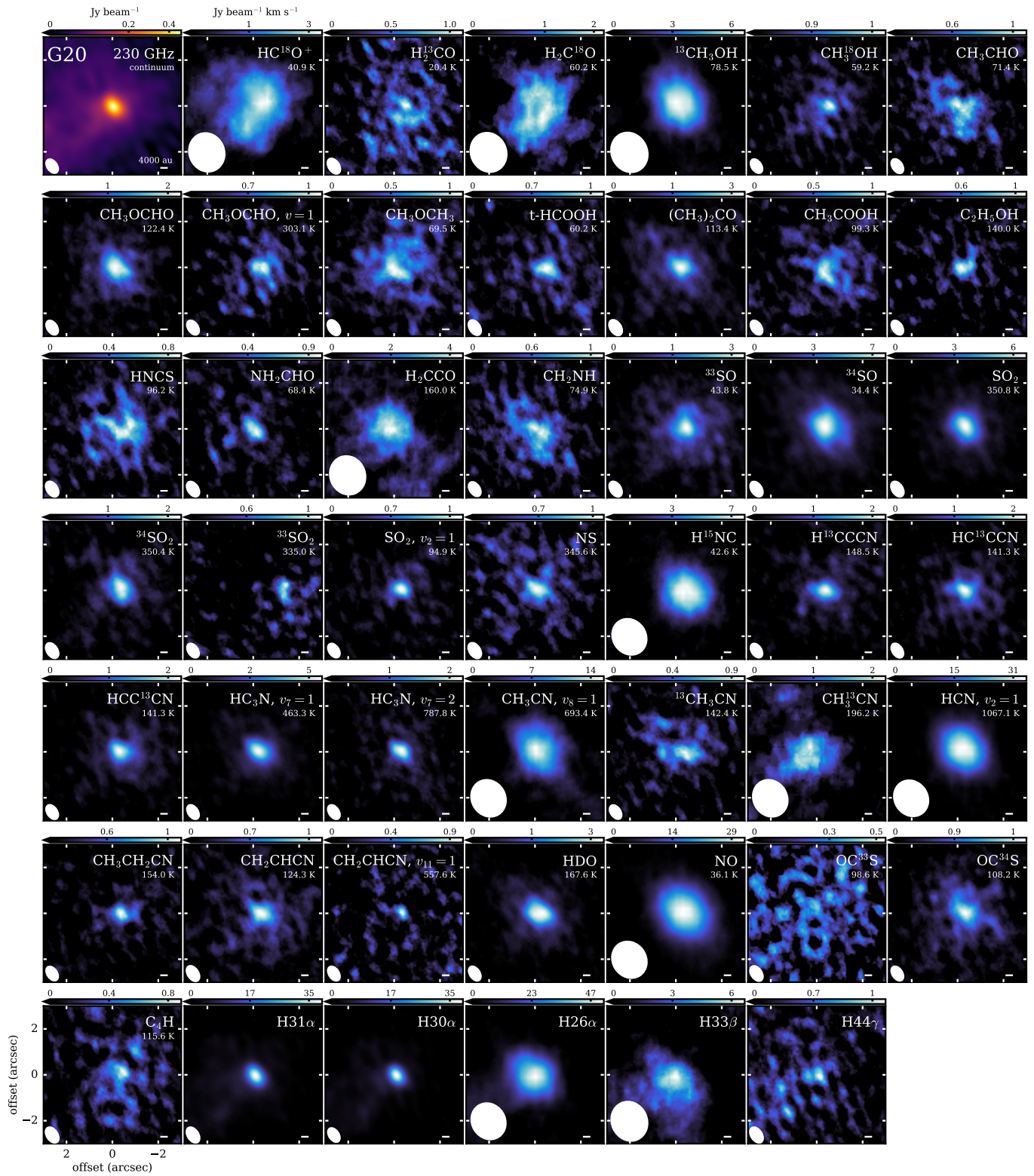


Figure 34. Gallery of spatially-compact lines in G20. Otherwise, as in Figure 32.

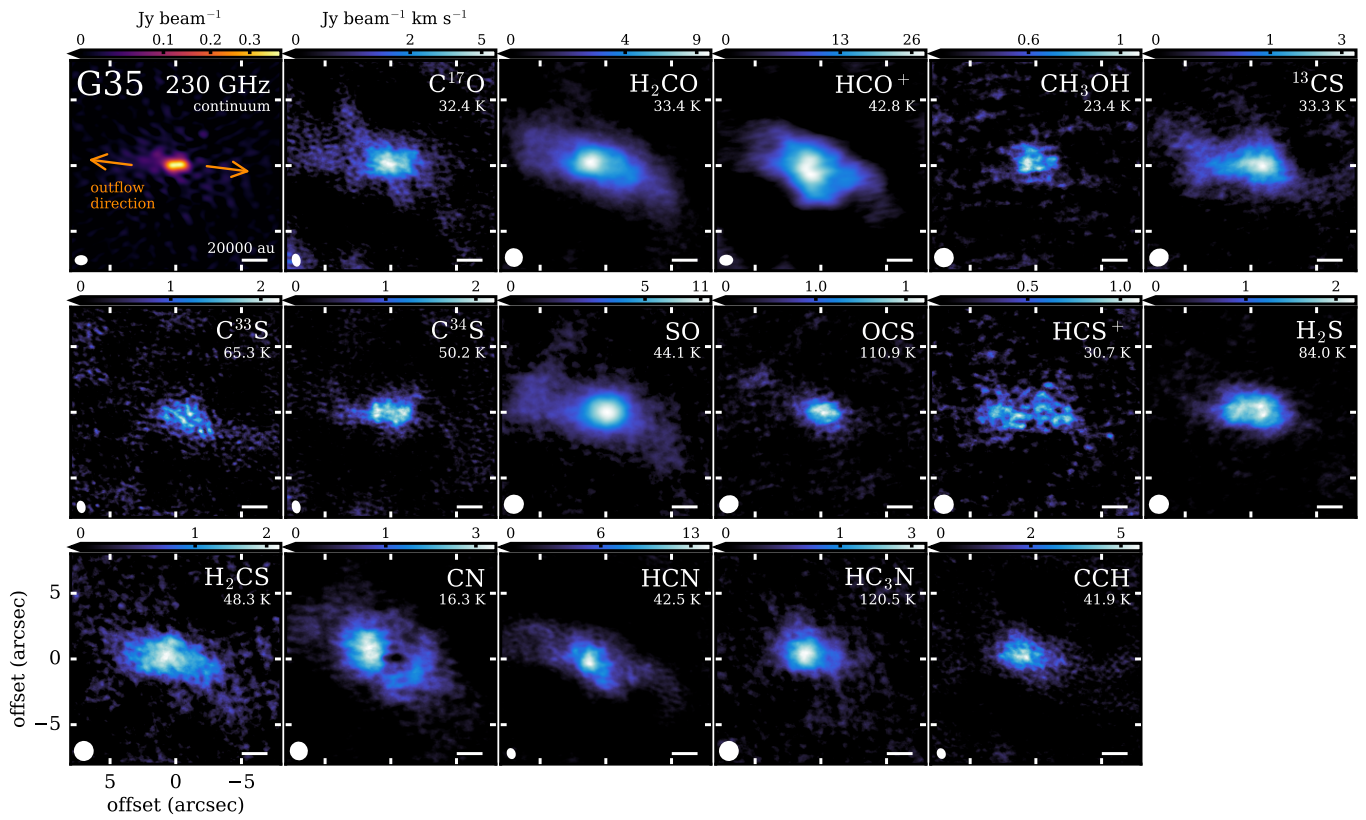


Figure 35. Gallery of spatially-extended lines in G35. The outflow direction, as traced by high-velocity ^{12}CO emission (Zhang et al. 2014), is marked in the continuum image. Otherwise, as in Figure 31.

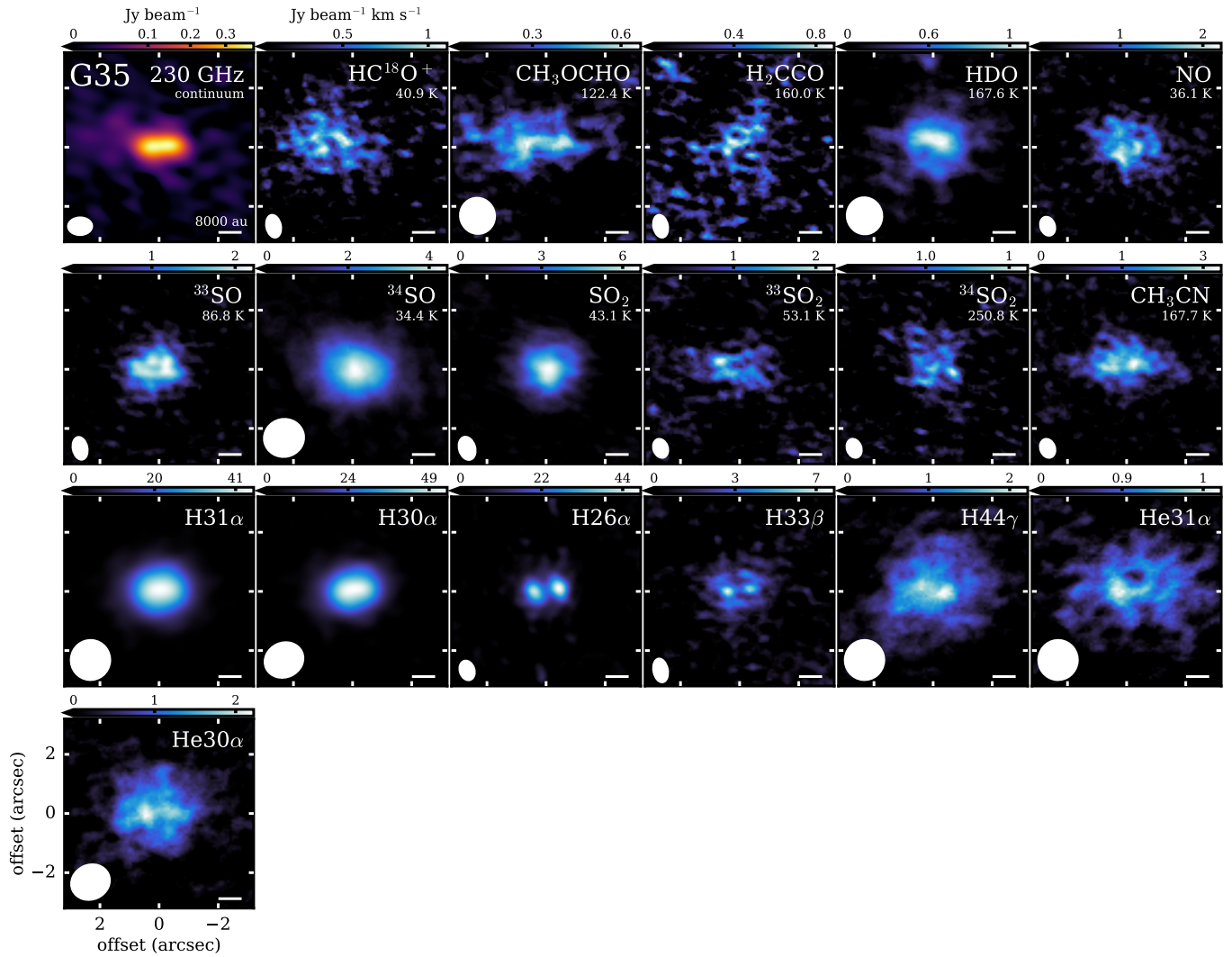


Figure 36. Gallery of spatially-compact lines in G35. Otherwise, as in Figure 32.

Table 5. References for Spectroscopic Information Used in this Work

Name	Molecule	Catalog	References
Carbon monoxide	C ¹⁷ O	CDMS	Klapper et al. 2003
Formaldehyde	H ₂ CO	CDMS	Bocquet et al. 1996; Mendoza et al. 2023
	H ₂ ¹³ CO	CDMS	Müller et al. 2000d; Mendoza et al. 2023
	H ₂ C ¹⁸ O	CDMS	Müller et al. 2000b; Mendoza et al. 2023
Formylium	HCO ⁺	CDMS	Tinti et al. 2007
	HC ¹⁸ O ⁺	CDMS	Schmid-Burgk et al. 2004
Methanol	CH ₃ OH	CDMS	Xu et al. 2008
	¹³ CH ₃ OH	CDMS	Xu & Lovas 1997
	CH ₃ ¹⁸ OH	CDMS	Fisher et al. 2007
Acetaldehyde	CH ₃ CHO	JPL	Kleiner et al. 1996
Methyl formate	CH ₃ OCHO	JPL	Ilyushin et al. 2009; Carvajal et al. 2019
	CH ₃ OCHO, $v = 1$	JPL	Ilyushin et al. 2009
Dimethyl ether	CH ₃ OCH ₃	CDMS	Endres et al. 2009
Formic acid	t-HCOOH	CDMS	Winnewisser et al. 2002
Acetone	(CH ₃) ₂ CO	JPL	Groner et al. 2002
Acetic acid	CH ₃ COOH	CDMS	Ilyushin et al. 2013; Xue et al. 2019
Ethanol	C ₂ H ₅ OH	CDMS	Pearson et al. 2008; Müller et al. 2016
Formamide	NH ₂ CHO	CDMS	Hirota et al. 1974; Motiyenko et al. 2012
Ketene	H ₂ CCO	CDMS	Brown et al. 1990; Johns et al. 1992
Water	HDO	JPL	Messer et al. 1984
Nitric oxide	NO	CDMS	Müller et al. 2015
Carbon monosulfide	¹³ CS	CDMS	Bogey et al. 1982
	C ³⁴ S	CDMS	Gottlieb et al. 2003
	C ³³ S	CDMS	Bogey et al. 1981
	¹³ C ³⁴ S	CDMS	Bogey et al. 1981
Sulfur monoxide	SO	CDMS	Tiemann 1982; Bogey et al. 1997
	S ¹⁸ O	CDMS	Tiemann 1974
	³⁴ SO	CDMS	Tiemann 1974; Klaus et al. 1996
	³³ SO	CDMS	Klaus et al. 1996
Sulfur dioxide	SO ₂	CDMS	Alekseev et al. 1996; Müller & Brünken 2005
	SO ₂ , $v_2 = 1$	CDMS	Alekseev et al. 1996; Müller & Brünken 2005
	³⁴ SO ₂	CDMS	Alekseev et al. 1996; Belov et al. 1998
	³³ SO ₂	CDMS	Müller et al. 2000a
Carbonyl sulfide	OCS	CDMS	Dubrulle et al. 1980; Golubiatnikov et al. 2005
	OC ³⁴ S	CDMS	Dubrulle et al. 1980; Vanek et al. 1989
	OC ³³ S	CDMS	Dubrulle et al. 1980; Burenin et al. 1981
Thioformylium	HCS ⁺	CDMS	Margulès et al. 2003
Hydrogen sulfide	H ₂ S	CDMS	Belov et al. 1995
Thioformaldehyde	H ₂ CS	CDMS	Beers et al. 1972; Maeda et al. 2008
	H ₂ C ³⁴ S	CDMS	Mcnaughton & Bruget 1993
Nitric sulfide	NS	CDMS	Lee et al. 1995
Isothiocyanic acid	HNCS	CDMS	Niedenhoff et al. 1995
Methyl cyanide	CH ₃ CN	CDMS	Müller et al. 2009
	CH ₃ CN, $v_8 = 1$	JPL	Bocquet et al. 1988
	¹³ CH ₃ CN	CDMS	Müller et al. 2009
	CH ₃ ¹³ CN	CDMS	Müller et al. 2009
Hydrogen cyanide	HCN, $v_2 = 1$	CDMS	Thorwirth et al. 2003
	H ¹³ C ¹⁵ N	CDMS	Fuchs et al. 2004
Hydrogen isocyanide	H ¹⁵ NC	JPL	Creswell et al. 1976; Pearson et al. 1976
Cyanoacetylene	HC ₃ N	CDMS	Thorwirth et al. 2000
	HC ₃ N, $v_7 = 1$	CDMS	Yamada & Creswell 1986; Thorwirth et al. 2000
	HC ₃ N, $v_7 = 2$	CDMS	Yamada & Creswell 1986; Thorwirth et al. 2000
	H ¹³ CCCN	CDMS	Thorwirth et al. 2001
	HC ¹³ CCN	CDMS	Thorwirth et al. 2001
	HCC ¹³ CN	CDMS	Thorwirth et al. 2001
Ethyl cyanide	CH ₃ CH ₂ CN	CDMS	Brauer et al. 2009
Vinyl cyanide	CH ₂ CHCN	CDMS	Müller et al. 2008
	CH ₂ CHCN, $v_{11}=1$	CDMS	Müller et al. 2008
Methanimine	CH ₂ NH	CDMS	Dore et al. 2012
Isocyanic acid	HNCO	CDMS	Lapinov et al. 2007; Carvajal et al. 2019
Ethynyl radical	CCH	CDMS	Müller et al. 2000c; Padovani et al. 2009
Cyclopropenyldiene	c-C ₃ H ₂	CDMS	Bogey & Destombes 1986; Bogey et al. 1987
Butadiynyl	C ₄ H	CDMS	Guelin et al. 1982; Gottlieb et al. 1983

NOTE—All spectroscopic data were obtained from the JPL (Pickett et al. 1998) and CDMS (Müller et al. 2001, 2005; Endres et al. 2016) catalogs.

Table 6. Assumed Isotopic Ratios

Source	D_{GC}	$^{12}C/^{13}C$	$^{16}O/^{18}O$	$^{32}S/^{33}S$	$^{32}S/^{34}S$
	(kpc)				
G28.20-0.05	4.6	47 ± 5	308 ± 54	83 ± 4	14 ± 1
G20.08-0.14 N	5.3	52 ± 5	349 ± 63	85 ± 4	15 ± 1
G35.58-0.03	6.0	56 ± 6	390 ± 71	87 ± 5	16 ± 1

NOTE—Following the approach of Nazari et al. (2022); Chen et al. (2023), we do not include the intercept error in the error propagation, as only the slope in Equations E1-E4 contains the information of the trend between the isotopic ratio and D_{GC} .

REFERENCES

- Alekseev, E. A., Dyubko, S. F., Ilyushin, V. V., & Podnos, S. V. 1996, *Journal of Molecular Spectroscopy*, 176, 316, doi: [10.1006/jmsp.1996.0092](https://doi.org/10.1006/jmsp.1996.0092)
- Allen, V., van der Tak, F. F. S., Sánchez-Monge, Á., Cesaroni, R., & Beltrán, M. T. 2017, *A&A*, 603, A133, doi: [10.1051/0004-6361/201629118](https://doi.org/10.1051/0004-6361/201629118)
- Anderson, L. D., & Bania, T. M. 2009, *ApJ*, 690, 706, doi: [10.1088/0004-637X/690/1/706](https://doi.org/10.1088/0004-637X/690/1/706)
- Argon, A. L., Reid, M. J., & Menten, K. M. 2000, *ApJS*, 129, 159, doi: [10.1086/313406](https://doi.org/10.1086/313406)
- Armante, M., Gusdorf, A., Louvet, F., et al. 2024, *A&A*, 686, A122, doi: [10.1051/0004-6361/202347595](https://doi.org/10.1051/0004-6361/202347595)
- Astropy Collaboration, Robitaille, T. P., Tollerud, E. J., et al. 2013, *A&A*, 558, A33, doi: [10.1051/0004-6361/201322068](https://doi.org/10.1051/0004-6361/201322068)
- Astropy Collaboration, Price-Whelan, A. M., Lim, P. L., et al. 2022, *ApJ*, 935, 167, doi: [10.3847/1538-4357/ac7c74](https://doi.org/10.3847/1538-4357/ac7c74)
- Balucani, N., Ceccarelli, C., & Taquet, V. 2015, *MNRAS*, 449, L16, doi: [10.1093/mnras/1slv009](https://doi.org/10.1093/mnras/1slv009)
- Beers, Y., Klein, G. P., Kirchhoff, W. H., & Johnson, D. R. 1972, *Journal of Molecular Spectroscopy*, 44, 553, doi: [10.1016/0022-2852\(72\)90263-9](https://doi.org/10.1016/0022-2852(72)90263-9)
- Beilis, D., Beck, S., & Lacy, J. 2022, *MNRAS*, 509, 2234, doi: [10.1093/mnras/stab3105](https://doi.org/10.1093/mnras/stab3105)
- Belov, S. P., Tretyakov, M. Y., Kozin, I. N., et al. 1998, *Journal of Molecular Spectroscopy*, 191, 17, doi: [10.1006/jmsp.1998.7576](https://doi.org/10.1006/jmsp.1998.7576)
- Belov, S. P., Yamada, K. M. T., Winnewisser, G., et al. 1995, *Journal of Molecular Spectroscopy*, 173, 380, doi: [10.1006/jmsp.1995.1242](https://doi.org/10.1006/jmsp.1995.1242)
- Bergin, E. A., Melnick, G. J., & Neufeld, D. A. 1998, *ApJ*, 499, 777, doi: [10.1086/305656](https://doi.org/10.1086/305656)
- Beuther, H., Churchwell, E. B., McKee, C. F., & Tan, J. C. 2007, in *Protostars and Planets V*, ed. B. Reipurth, D. Jewitt, & K. Keil, 165, doi: [10.48550/arXiv.astro-ph/0602012](https://doi.org/10.48550/arXiv.astro-ph/0602012)
- Bisschop, S. E., Jørgensen, J. K., van Dishoeck, E. F., & de Wachter, E. B. M. 2007, *A&A*, 465, 913, doi: [10.1051/0004-6361:20065963](https://doi.org/10.1051/0004-6361:20065963)
- Bjerkeli, P., Jørgensen, J. K., Bergin, E. A., et al. 2016, *A&A*, 595, A39, doi: [10.1051/0004-6361/201628795](https://doi.org/10.1051/0004-6361/201628795)
- Blake, G. A., Mundy, L. G., Carlstrom, J. E., et al. 1996, *ApJL*, 472, L49, doi: [10.1086/310347](https://doi.org/10.1086/310347)
- Blake, G. A., Sutton, E. C., Masson, C. R., & Phillips, T. G. 1987, *ApJ*, 315, 621, doi: [10.1086/165165](https://doi.org/10.1086/165165)
- Bocquet, R., Wlodarczak, G., Bauer, A., & Demaison, J. 1988, *Journal of Molecular Spectroscopy*, 127, 382, doi: [10.1016/0022-2852\(88\)90128-2](https://doi.org/10.1016/0022-2852(88)90128-2)
- Bocquet, R., Demaison, J., Poteau, L., et al. 1996, *Journal of Molecular Spectroscopy*, 177, 154, doi: [10.1006/jmsp.1996.0128](https://doi.org/10.1006/jmsp.1996.0128)
- Bøgelund, E. G., Barr, A. G., Taquet, V., et al. 2019, *A&A*, 628, A2, doi: [10.1051/0004-6361/201834527](https://doi.org/10.1051/0004-6361/201834527)
- Bogey, M., Civiš, S., Delcroix, B., et al. 1997, *Journal of Molecular Spectroscopy*, 182, 85, doi: [10.1006/jmsp.1996.7218](https://doi.org/10.1006/jmsp.1996.7218)
- Bogey, M., Demuynck, C., & Destombes, J. L. 1981, *Chemical Physics Letters*, 81, 256, doi: [10.1016/0009-2614\(81\)80247-3](https://doi.org/10.1016/0009-2614(81)80247-3)
- . 1982, *Journal of Molecular Spectroscopy*, 95, 35, doi: [10.1016/0022-2852\(82\)90234-X](https://doi.org/10.1016/0022-2852(82)90234-X)
- Bogey, M., Demuynck, C., Destombes, J. L., & Dubus, H. 1987, *Journal of Molecular Spectroscopy*, 122, 313, doi: [10.1016/0022-2852\(87\)90007-5](https://doi.org/10.1016/0022-2852(87)90007-5)
- Bogey, M., & Destombes, J. L. 1986, *A&A*, 159, L8

- Brauer, C. S., Pearson, J. C., Drouin, B. J., & Yu, S. 2009, *ApJS*, 184, 133, doi: [10.1088/0067-0049/184/1/133](https://doi.org/10.1088/0067-0049/184/1/133)
- Brouillet, N., Despois, D., Molet, J., et al. 2022, *A&A*, 665, A140, doi: [10.1051/0004-6361/202243669](https://doi.org/10.1051/0004-6361/202243669)
- Brown, R. D., Godfrey, P. D., McNaughton, D., Pierlot, A. P., & Taylor, W. H. 1990, *Journal of Molecular Spectroscopy*, 140, 340, doi: [10.1016/0022-2852\(90\)90146-H](https://doi.org/10.1016/0022-2852(90)90146-H)
- Burenin, A. V., Val'dov, A. N., Karyakin, E. N., Krupnov, A. F., & Shapin, S. M. 1981, *Journal of Molecular Spectroscopy*, 87, 312, doi: [10.1016/0022-2852\(81\)90404-5](https://doi.org/10.1016/0022-2852(81)90404-5)
- Burkholder, J. B., Sinha, A., Hammer, P. D., & Howard, C. J. 1987, *Journal of Molecular Spectroscopy*, 126, 72, doi: [10.1016/0022-2852\(87\)90077-4](https://doi.org/10.1016/0022-2852(87)90077-4)
- Busch, L. A., Belloche, A., Garrod, R. T., Müller, H. S. P., & Menten, K. M. 2022, *A&A*, 665, A96, doi: [10.1051/0004-6361/202243383](https://doi.org/10.1051/0004-6361/202243383)
- Carvajal, M., Favre, C., Kleiner, I., et al. 2019, *A&A*, 627, A65, doi: [10.1051/0004-6361/201935469](https://doi.org/10.1051/0004-6361/201935469)
- CASA Team, Bean, B., Bhatnagar, S., et al. 2022, *PASP*, 134, 114501, doi: [10.1088/1538-3873/ac9642](https://doi.org/10.1088/1538-3873/ac9642)
- Chen, Y., van Gelder, M. L., Nazari, P., et al. 2023, *A&A*, 678, A137, doi: [10.1051/0004-6361/202346491](https://doi.org/10.1051/0004-6361/202346491)
- Churchwell, E. 2002, *ARA&A*, 40, 27, doi: [10.1146/annurev.astro.40.060401.093845](https://doi.org/10.1146/annurev.astro.40.060401.093845)
- Codella, C., Ceccarelli, C., Caselli, P., et al. 2017, *A&A*, 605, L3, doi: [10.1051/0004-6361/201731249](https://doi.org/10.1051/0004-6361/201731249)
- Coletta, A., Fontani, F., Rivilla, V. M., et al. 2020, *A&A*, 641, A54, doi: [10.1051/0004-6361/202038212](https://doi.org/10.1051/0004-6361/202038212)
- Contreras, Y., Schuller, F., Urquhart, J. S., et al. 2013, *A&A*, 549, A45, doi: [10.1051/0004-6361/201220155](https://doi.org/10.1051/0004-6361/201220155)
- Creswell, R. A., Pearson, E. F., Winnewisser, M., & Winnewisser, G. 1976, *Zeitschrift Naturforschung Teil A*, 31, 221, doi: [10.1515/zna-1976-3-401](https://doi.org/10.1515/zna-1976-3-401)
- Csengeri, T., Belloche, A., Bontemps, S., et al. 2019, *A&A*, 632, A57, doi: [10.1051/0004-6361/201935226](https://doi.org/10.1051/0004-6361/201935226)
- Csengeri, T., Bontemps, S., Wyrowski, F., et al. 2017, *A&A*, 601, A60, doi: [10.1051/0004-6361/201628254](https://doi.org/10.1051/0004-6361/201628254)
- De Buizer, J. M., Radomski, J. T., Telesco, C. M., & Piña, R. K. 2005, *ApJS*, 156, 179, doi: [10.1086/426941](https://doi.org/10.1086/426941)
- Dore, L., Bizzocchi, L., & Degli Esposti, C. 2012, *A&A*, 544, A19, doi: [10.1051/0004-6361/201219674](https://doi.org/10.1051/0004-6361/201219674)
- Dubrulle, A., Demaison, J., Burie, J., & Boucher, D. 1980, *Zeitschrift Naturforschung Teil A*, 35, 471, doi: [10.1515/zna-1980-0501](https://doi.org/10.1515/zna-1980-0501)
- Durig, J. R., Bucy, W. E., Wurrey, C. J., & Carreira, L. A. 1975, *The Journal of Physical Chemistry*, 79, 988, doi: [10.1021/j100577a009](https://doi.org/10.1021/j100577a009)
- Dyck, H. M., & Simon, T. 1977, *ApJ*, 211, 421, doi: [10.1086/154947](https://doi.org/10.1086/154947)
- Endres, C. P., Drouin, B. J., Pearson, J. C., et al. 2009, *A&A*, 504, 635, doi: [10.1051/0004-6361/200912409](https://doi.org/10.1051/0004-6361/200912409)
- Endres, C. P., Schlemmer, S., Schilke, P., Stutzki, J., & Müller, H. S. P. 2016, *Journal of Molecular Spectroscopy*, 327, 95, doi: [10.1016/j.jms.2016.03.005](https://doi.org/10.1016/j.jms.2016.03.005)
- Fayolle, E. C., Öberg, K. I., Garrod, R. T., van Dishoeck, E. F., & Bisschop, S. E. 2015, *A&A*, 576, A45, doi: [10.1051/0004-6361/201323114](https://doi.org/10.1051/0004-6361/201323114)
- Fish, V. L., Reid, M. J., Argon, A. L., & Zheng, X.-W. 2005, *ApJS*, 160, 220, doi: [10.1086/431669](https://doi.org/10.1086/431669)
- Fish, V. L., Reid, M. J., Wilner, D. J., & Churchwell, E. 2003, *ApJ*, 587, 701, doi: [10.1086/368284](https://doi.org/10.1086/368284)
- Fisher, J., Paciga, G., Xu, L.-H., et al. 2007, *Journal of Molecular Spectroscopy*, 245, 7, doi: [10.1016/j.jms.2007.06.004](https://doi.org/10.1016/j.jms.2007.06.004)
- Fontani, F., Pascucci, I., Caselli, P., et al. 2007, *A&A*, 470, 639, doi: [10.1051/0004-6361:20077485](https://doi.org/10.1051/0004-6361:20077485)
- Foreman-Mackey, D., Hogg, D. W., Lang, D., & Goodman, J. 2013, *PASP*, 125, 306, doi: [10.1086/670067](https://doi.org/10.1086/670067)
- Forster, J. R., & Caswell, J. L. 1989, *A&A*, 213, 339
- Fraser, H. J., Collings, M. P., McCoustra, M. R. S., & Williams, D. A. 2001, *MNRAS*, 327, 1165, doi: [10.1046/j.1365-8711.2001.04835.x](https://doi.org/10.1046/j.1365-8711.2001.04835.x)
- Friedel, D. N., & Snyder, L. E. 2008, *ApJ*, 672, 962, doi: [10.1086/523896](https://doi.org/10.1086/523896)
- Fuchs, U., Bruenken, S., Fuchs, G. W., et al. 2004, *Zeitschrift Naturforschung Teil A*, 59, 861, doi: [10.1515/zna-2004-1123](https://doi.org/10.1515/zna-2004-1123)
- Galván-Madrid, R., Keto, E., Zhang, Q., et al. 2009, *ApJ*, 706, 1036, doi: [10.1088/0004-637X/706/2/1036](https://doi.org/10.1088/0004-637X/706/2/1036)
- Galván-Madrid, R., Zhang, Q., Izquierdo, A., et al. 2023, *ApJL*, 942, L7, doi: [10.3847/2041-8213/aca9cb](https://doi.org/10.3847/2041-8213/aca9cb)
- Garay, G., Reid, M. J., & Moran, J. M. 1985, *ApJ*, 289, 681, doi: [10.1086/162932](https://doi.org/10.1086/162932)
- Garrod, R. T., & Herbst, E. 2006, *A&A*, 457, 927, doi: [10.1051/0004-6361:20065560](https://doi.org/10.1051/0004-6361:20065560)
- Garrod, R. T., Widicus Weaver, S. L., & Herbst, E. 2008, *ApJ*, 682, 283, doi: [10.1086/588035](https://doi.org/10.1086/588035)
- Genzel, R., & Downes, D. 1977, *A&AS*, 30, 145
- Gerner, T., Beuther, H., Semenov, D., et al. 2014, *A&A*, 563, A97, doi: [10.1051/0004-6361/201322541](https://doi.org/10.1051/0004-6361/201322541)
- Gerner, T., Shirley, Y. L., Beuther, H., et al. 2015, *A&A*, 579, A80, doi: [10.1051/0004-6361/201423989](https://doi.org/10.1051/0004-6361/201423989)
- Gieser, C., Beuther, H., Semenov, D., et al. 2021, *A&A*, 648, A66, doi: [10.1051/0004-6361/202039670](https://doi.org/10.1051/0004-6361/202039670)
- Goldsmith, P. F., & Langer, W. D. 1999, *ApJ*, 517, 209, doi: [10.1086/307195](https://doi.org/10.1086/307195)
- Golubiatnikov, G. Y., Lapinov, A. V., Guarnieri, A., & Knöchel, R. 2005, *Journal of Molecular Spectroscopy*, 234, 190, doi: [10.1016/j.jms.2005.08.012](https://doi.org/10.1016/j.jms.2005.08.012)

- Gorai, P., Law, C.-Y., Tan, J. C., et al. 2024, *ApJ*, 960, 127, doi: [10.3847/1538-4357/ad09bb](https://doi.org/10.3847/1538-4357/ad09bb)
- Gottlieb, C. A., Gottlieb, E. W., Thaddeus, P., & Kawamura, H. 1983, *ApJ*, 275, 916, doi: [10.1086/161585](https://doi.org/10.1086/161585)
- Gottlieb, C. A., Myers, P. C., & Thaddeus, P. 2003, *ApJ*, 588, 655, doi: [10.1086/368378](https://doi.org/10.1086/368378)
- Groner, P., Albert, S., Herbst, E., et al. 2002, *ApJS*, 142, 145, doi: [10.1086/341221](https://doi.org/10.1086/341221)
- Guelin, M., Friberg, P., & Mezaoui, A. 1982, *A&A*, 109, 23
- Gusdorf, A., Cabrit, S., Flower, D. R., & Pineau Des Forêts, G. 2008, *A&A*, 482, 809, doi: [10.1051/0004-6361/20078900](https://doi.org/10.1051/0004-6361/20078900)
- Han, F., Mao, R. Q., Lu, J., et al. 1998, *A&AS*, 127, 181, doi: [10.1051/aas:1998342](https://doi.org/10.1051/aas:1998342)
- Haschick, A. D., & Ho, P. T. P. 1983, *ApJ*, 267, 638, doi: [10.1086/160900](https://doi.org/10.1086/160900)
- Haschick, A. D., Menten, K. M., & Baan, W. A. 1990, *ApJ*, 354, 556, doi: [10.1086/168715](https://doi.org/10.1086/168715)
- Heise, H. M., Winther, F., & Lutz, H. 1981, *Journal of Molecular Spectroscopy*, 90, 531, doi: [10.1016/0022-2852\(81\)90145-4](https://doi.org/10.1016/0022-2852(81)90145-4)
- Herbst, E., & van Dishoeck, E. F. 2009, *ARA&A*, 47, 427, doi: [10.1146/annurev-astro-082708-101654](https://doi.org/10.1146/annurev-astro-082708-101654)
- Hernández-Hernández, V., Zapata, L., Kurtz, S., & Garay, G. 2014, *ApJ*, 786, 38, doi: [10.1088/0004-637X/786/1/38](https://doi.org/10.1088/0004-637X/786/1/38)
- Hirota, E., Sugisaki, R., Nielsen, C. J., & Sørensen, G. O. 1974, *Journal of Molecular Spectroscopy*, 49, 251, doi: [10.1016/0022-2852\(74\)90274-4](https://doi.org/10.1016/0022-2852(74)90274-4)
- Ho, P. T. P., Haschick, A. D., Vogel, S. N., & Wright, M. C. H. 1983, *ApJ*, 265, 295, doi: [10.1086/160675](https://doi.org/10.1086/160675)
- Ho, P. T. P., Moran, J. M., & Lo, K. Y. 2004, *ApJL*, 616, L1, doi: [10.1086/423245](https://doi.org/10.1086/423245)
- Hoare, M. G., Kurtz, S. E., Lizano, S., Keto, E., & Hofner, P. 2007, in *Protostars and Planets V*, ed. B. Reipurth, D. Jewitt, & K. Keil, 181, doi: [10.48550/arXiv.astro-ph/0603560](https://doi.org/10.48550/arXiv.astro-ph/0603560)
- Hoare, M. G., Purcell, C. R., Churchwell, E. B., et al. 2012, *PASP*, 124, 939, doi: [10.1086/668058](https://doi.org/10.1086/668058)
- Hofner, P., & Churchwell, E. 1996, *A&AS*, 120, 283
- Hunter, J. D. 2007, *Computing in Science and Engineering*, 9, 90, doi: [10.1109/MCSE.2007.55](https://doi.org/10.1109/MCSE.2007.55)
- Ilee, J. D., Cyganowski, C. J., Brogan, C. L., et al. 2018, *ApJL*, 869, L24, doi: [10.3847/2041-8213/aaeffc](https://doi.org/10.3847/2041-8213/aaeffc)
- Ilyushin, V., Kryvda, A., & Alekseev, E. 2009, *Journal of Molecular Spectroscopy*, 255, 32, doi: [10.1016/j.jms.2009.01.016](https://doi.org/10.1016/j.jms.2009.01.016)
- Ilyushin, V. V., Endres, C. P., Lewen, F., Schlemmer, S., & Drouin, B. J. 2013, *Journal of Molecular Spectroscopy*, 290, 31, doi: [10.1016/j.jms.2013.06.005](https://doi.org/10.1016/j.jms.2013.06.005)
- Immer, K., Galván-Madrid, R., König, C., Liu, H. B., & Menten, K. M. 2014, *A&A*, 572, A63, doi: [10.1051/0004-6361/201423780](https://doi.org/10.1051/0004-6361/201423780)
- Immer, K., Reid, M. J., Menten, K. M., Brunthaler, A., & Dame, T. M. 2013, *A&A*, 553, A117, doi: [10.1051/0004-6361/201220793](https://doi.org/10.1051/0004-6361/201220793)
- Jiménez-Serra, I., Báez-Rubio, A., Martín-Pintado, J., Zhang, Q., & Rivilla, V. M. 2020, *ApJL*, 897, L33, doi: [10.3847/2041-8213/aba050](https://doi.org/10.3847/2041-8213/aba050)
- Jiménez-Serra, I., Zhang, Q., Viti, S., Martín-Pintado, J., & de Wit, W. J. 2012, *ApJ*, 753, 34, doi: [10.1088/0004-637X/753/1/34](https://doi.org/10.1088/0004-637X/753/1/34)
- Johns, J. W. C., Nemes, L., Yamada, K. M. T., et al. 1992, *Journal of Molecular Spectroscopy*, 156, 501, doi: [10.1016/0022-2852\(92\)90249-N](https://doi.org/10.1016/0022-2852(92)90249-N)
- Keto, E., Zhang, Q., & Kurtz, S. 2008, *ApJ*, 672, 423, doi: [10.1086/522570](https://doi.org/10.1086/522570)
- Khan, S., Pandian, J. D., Lal, D. V., et al. 2022, *A&A*, 664, A140, doi: [10.1051/0004-6361/202140914](https://doi.org/10.1051/0004-6361/202140914)
- Klaassen, P. D., & Wilson, C. D. 2007, *ApJ*, 663, 1092, doi: [10.1086/518760](https://doi.org/10.1086/518760)
- Klaassen, P. D., Wilson, C. D., Keto, E. R., & Zhang, Q. 2009, *ApJ*, 703, 1308, doi: [10.1088/0004-637X/703/2/1308](https://doi.org/10.1088/0004-637X/703/2/1308)
- Klaassen, P. D., Wilson, C. D., Keto, E. R., et al. 2011, *A&A*, 530, A53, doi: [10.1051/0004-6361/201016371](https://doi.org/10.1051/0004-6361/201016371)
- Klapper, G., Surin, L., Lewen, F., et al. 2003, *ApJ*, 582, 262, doi: [10.1086/344615](https://doi.org/10.1086/344615)
- Klaus, T., Saleck, A. H., Belov, S. P., et al. 1996, *Journal of Molecular Spectroscopy*, 180, 197, doi: [10.1006/jmsp.1996.0243](https://doi.org/10.1006/jmsp.1996.0243)
- Kleiner, I., Lovas, F. J., & Godefroid, M. 1996, *Journal of Physical and Chemical Reference Data*, 25, 1113, doi: [10.1063/1.555983](https://doi.org/10.1063/1.555983)
- Kryvda, A. V., Gerasimov, V. G., Dyubko, S. F., Alekseev, E. A., & Motiyenko, R. A. 2009, *Journal of Molecular Spectroscopy*, 254, 28, doi: [10.1016/j.jms.2008.12.001](https://doi.org/10.1016/j.jms.2008.12.001)
- Kurtz, S., Cesaroni, R., Churchwell, E., Hofner, P., & Walmsley, C. M. 2000, in *Protostars and Planets IV*, ed. V. Mannings, A. P. Boss, & S. S. Russell, 299–326
- Kurtz, S., Churchwell, E., & Wood, D. O. S. 1994, *ApJS*, 91, 659, doi: [10.1086/191952](https://doi.org/10.1086/191952)
- Kurtz, S. E., Watson, A. M., Hofner, P., & Otte, B. 1999, *ApJ*, 514, 232, doi: [10.1086/306928](https://doi.org/10.1086/306928)
- Lapinov, A. V., Golubiatnikov, G. Y., Markov, V. N., & Guarnieri, A. 2007, *Astronomy Letters*, 33, 121, doi: [10.1134/S1063773707020065](https://doi.org/10.1134/S1063773707020065)
- Law, C. J., Zhang, Q., Öberg, K. I., et al. 2021, *ApJ*, 909, 214, doi: [10.3847/1538-4357/abdeb8](https://doi.org/10.3847/1538-4357/abdeb8)

- Law, C.-Y., Tan, J. C., Gorai, P., et al. 2022, *ApJ*, 939, 120, doi: [10.3847/1538-4357/ac90c7](https://doi.org/10.3847/1538-4357/ac90c7)
- Lee, J.-E., Kim, C.-H., Lee, S., et al. 2024, *ApJ*, 966, 119, doi: [10.3847/1538-4357/ad3106](https://doi.org/10.3847/1538-4357/ad3106)
- Lee, S. K., Ozeki, H., & Saito, S. 1995, *ApJS*, 98, 351, doi: [10.1086/192165](https://doi.org/10.1086/192165)
- Li, J., Wang, J., Zhu, Q., Zhang, J., & Li, D. 2015, *ApJ*, 802, 40, doi: [10.1088/0004-637X/802/1/40](https://doi.org/10.1088/0004-637X/802/1/40)
- Lin, Y., Liu, H. B., Li, D., et al. 2016, *ApJ*, 828, 32, doi: [10.3847/0004-637X/828/1/32](https://doi.org/10.3847/0004-637X/828/1/32)
- Liu, H. B., Jiménez-Serra, I., Ho, P. T. P., et al. 2012, *ApJ*, 756, 10, doi: [10.1088/0004-637X/756/1/10](https://doi.org/10.1088/0004-637X/756/1/10)
- Liu, H.-L., Liu, T., Evans, Neal J., I., et al. 2021, *MNRAS*, 505, 2801, doi: [10.1093/mnras/stab1352](https://doi.org/10.1093/mnras/stab1352)
- Liu, M., Tan, J. C., De Buizer, J. M., et al. 2019a, *ApJ*, 874, 16, doi: [10.3847/1538-4357/ab07b7](https://doi.org/10.3847/1538-4357/ab07b7)
- Liu, Y., Dipierro, G., Ragusa, E., et al. 2019b, *A&A*, 622, A75, doi: [10.1051/0004-6361/201834157](https://doi.org/10.1051/0004-6361/201834157)
- López-Sepulcre, A., Jaber, A. A., Mendoza, E., et al. 2015, *MNRAS*, 449, 2438, doi: [10.1093/mnras/stv377](https://doi.org/10.1093/mnras/stv377)
- Lu, X., Li, G.-X., Zhang, Q., & Lin, Y. 2022, *Nature Astronomy*, 6, 837, doi: [10.1038/s41550-022-01681-4](https://doi.org/10.1038/s41550-022-01681-4)
- Maeda, A., Medvedev, I. R., Winnewisser, M., et al. 2008, *ApJS*, 176, 543, doi: [10.1086/528684](https://doi.org/10.1086/528684)
- Maki, A. G., & Mellau, G. C. 2001, *Journal of Molecular Spectroscopy*, 206, 47, doi: [10.1006/jmsp.2000.8279](https://doi.org/10.1006/jmsp.2000.8279)
- Mallinson, P. D., & Fayt, A. 1976, *Molecular Physics*, 32, 473, doi: [10.1080/00268977600103231](https://doi.org/10.1080/00268977600103231)
- Margulès, L., Lewen, F., Winnewisser, G., Botschwina, P., & Müller, H. S. P. 2003, *Physical Chemistry Chemical Physics (Incorporating Faraday Transactions)*, 5, 2770, doi: [10.1039/B303260D](https://doi.org/10.1039/B303260D)
- Maud, L. T., Cesaroni, R., Kumar, M. S. N., et al. 2018, *A&A*, 620, A31, doi: [10.1051/0004-6361/201833908](https://doi.org/10.1051/0004-6361/201833908)
- McClure, M. K., Rocha, W. R. M., Pontoppidan, K. M., et al. 2023, *Nature Astronomy*, 7, 431, doi: [10.1038/s41550-022-01875-w](https://doi.org/10.1038/s41550-022-01875-w)
- McGuire, B. A., Brogan, C. L., Hunter, T. R., et al. 2018, *ApJL*, 863, L35, doi: [10.3847/2041-8213/aad7bb](https://doi.org/10.3847/2041-8213/aad7bb)
- McMullin, J. P., Waters, B., Schiebel, D., Young, W., & Golap, K. 2007, in *Astronomical Society of the Pacific Conference Series*, Vol. 376, *Astronomical Data Analysis Software and Systems XVI*, ed. R. A. Shaw, F. Hill, & D. J. Bell, 127
- Menaughton, D., & Bruget, D. N. 1993, *Journal of Molecular Spectroscopy*, 159, 340, doi: [10.1006/jmsp.1993.1132](https://doi.org/10.1006/jmsp.1993.1132)
- Mendoza, E., Carvajal, M., Merello, M., Bronfman, L., & Boechat-Roberty, H. M. 2023, *ApJ*, 953, 77, doi: [10.3847/1538-4357/ace048](https://doi.org/10.3847/1538-4357/ace048)
- Menten, K. M. 1991, *ApJL*, 380, L75, doi: [10.1086/186177](https://doi.org/10.1086/186177)
- Menten, K. M., Walmsley, C. M., Henkel, C., et al. 1986, *A&A*, 169, 271
- Messer, J. K., De Lucia, F. C., & Helminger, P. 1984, *Journal of Molecular Spectroscopy*, 105, 139, doi: [10.1016/0022-2852\(84\)90109-7](https://doi.org/10.1016/0022-2852(84)90109-7)
- Milam, S. N., Savage, C., Brewster, M. A., Ziurys, L. M., & Wyckoff, S. 2005, *ApJ*, 634, 1126, doi: [10.1086/497123](https://doi.org/10.1086/497123)
- Minh, Y. C., Liu, H. B., & Galvañ-Madrid, R. 2016, *ApJ*, 824, 99, doi: [10.3847/0004-637X/824/2/99](https://doi.org/10.3847/0004-637X/824/2/99)
- Mininni, C., Beltrán, M. T., Colzi, L., et al. 2023, *A&A*, 677, A15, doi: [10.1051/0004-6361/202245277](https://doi.org/10.1051/0004-6361/202245277)
- Molinari, S., Swinyard, B., Bally, J., et al. 2010, *PASP*, 122, 314, doi: [10.1086/651314](https://doi.org/10.1086/651314)
- Morales, E. F. E., Wyrowski, F., Schuller, F., & Menten, K. M. 2013, *A&A*, 560, A76, doi: [10.1051/0004-6361/201321626](https://doi.org/10.1051/0004-6361/201321626)
- Moscadelli, L., Rivilla, V. M., Cesaroni, R., et al. 2018, *A&A*, 616, A66, doi: [10.1051/0004-6361/201832680](https://doi.org/10.1051/0004-6361/201832680)
- Motiyenko, R. A., Tercero, B., Cernicharo, J., & Margulès, L. 2012, *A&A*, 548, A71, doi: [10.1051/0004-6361/201220033](https://doi.org/10.1051/0004-6361/201220033)
- Motte, F., Bontemps, S., & Louvet, F. 2018, *ARA&A*, 56, 41, doi: [10.1146/annurev-astro-091916-055235](https://doi.org/10.1146/annurev-astro-091916-055235)
- Motte, F., Bontemps, S., Csengeri, T., et al. 2022, *A&A*, 662, A8, doi: [10.1051/0004-6361/202141677](https://doi.org/10.1051/0004-6361/202141677)
- Müller, H. S. P., Belloche, A., Menten, K. M., Comito, C., & Schilke, P. 2008, *Journal of Molecular Spectroscopy*, 251, 319, doi: [10.1016/j.jms.2008.03.016](https://doi.org/10.1016/j.jms.2008.03.016)
- Müller, H. S. P., & Brünken, S. 2005, *Journal of Molecular Spectroscopy*, 232, 213, doi: [10.1016/j.jms.2005.04.010](https://doi.org/10.1016/j.jms.2005.04.010)
- Müller, H. S. P., Drouin, B. J., & Pearson, J. C. 2009, *A&A*, 506, 1487, doi: [10.1051/0004-6361/200912932](https://doi.org/10.1051/0004-6361/200912932)
- Müller, H. S. P., Farhoomand, J., Cohen, E. A., et al. 2000a, *Journal of Molecular Spectroscopy*, 201, 1, doi: [10.1006/jmsp.2000.8072](https://doi.org/10.1006/jmsp.2000.8072)
- Müller, H. S. P., Gendriesch, R., Lewen, F., & Winnewisser, G. 2000b, *Zeitschrift Naturforschung Teil A*, 55, 486, doi: [10.1515/zna-2000-0502](https://doi.org/10.1515/zna-2000-0502)
- Müller, H. S. P., Klaus, T., & Winnewisser, G. 2000c, *A&A*, 357, L65
- Müller, H. S. P., Kobayashi, K., Takahashi, K., Tomaru, K., & Matsushima, F. 2015, *Journal of Molecular Spectroscopy*, 310, 92, doi: [10.1016/j.jms.2014.12.002](https://doi.org/10.1016/j.jms.2014.12.002)
- Müller, H. S. P., Schlöder, F., Stutzki, J., & Winnewisser, G. 2005, *Journal of Molecular Structure*, 742, 215, doi: [10.1016/j.molstruc.2005.01.027](https://doi.org/10.1016/j.molstruc.2005.01.027)
- Müller, H. S. P., Thorwirth, S., Roth, D. A., & Winnewisser, G. 2001, *A&A*, 370, L49, doi: [10.1051/0004-6361:20010367](https://doi.org/10.1051/0004-6361:20010367)

- Müller, H. S. P., Gendriesch, R., Margulès, L., et al. 2000d, *Physical Chemistry Chemical Physics (Incorporating Faraday Transactions)*, 2, 3401, doi: [10.1039/B002819N](https://doi.org/10.1039/B002819N)
- Müller, H. S. P., Belloche, A., Xu, L.-H., et al. 2016, *A&A*, 587, A92, doi: [10.1051/0004-6361/201527470](https://doi.org/10.1051/0004-6361/201527470)
- Mürtz, M., Palm, P., Urban, W., & Maki, A. G. 2000, *Journal of Molecular Spectroscopy*, 204, 281, doi: [10.1006/jmsp.2000.8217](https://doi.org/10.1006/jmsp.2000.8217)
- Nazari, P., Tabone, B., van't Hoff, M. L. R., Jørgensen, J. K., & van Dishoeck, E. F. 2023, *ApJL*, 951, L38, doi: [10.3847/2041-8213/acdde4](https://doi.org/10.3847/2041-8213/acdde4)
- Nazari, P., Meijerhof, J. D., van Gelder, M. L., et al. 2022, *A&A*, 668, A109, doi: [10.1051/0004-6361/202243788](https://doi.org/10.1051/0004-6361/202243788)
- Niedenhoff, M., Winnewisser, G., Yamada, K. M. T., & Belov, S. P. 1995, *Journal of Molecular Spectroscopy*, 169, 224, doi: [10.1006/jmsp.1995.1018](https://doi.org/10.1006/jmsp.1995.1018)
- Padovani, M., Walmsley, C. M., Tafalla, M., Galli, D., & Müller, H. S. P. 2009, *A&A*, 505, 1199, doi: [10.1051/0004-6361/200912547](https://doi.org/10.1051/0004-6361/200912547)
- Pearson, E. F., Creswell, R. A., Winnewisser, M., & Winnewisser, G. 1976, *Zeitschrift Naturforschung Teil A*, 31, 1394, doi: [10.1515/zna-1976-1119](https://doi.org/10.1515/zna-1976-1119)
- Pearson, J. C., Brauer, C. S., & Drouin, B. J. 2008, *Journal of Molecular Spectroscopy*, 251, 394, doi: [10.1016/j.jms.2008.05.007](https://doi.org/10.1016/j.jms.2008.05.007)
- Pickett, H. M., Poynter, R. L., Cohen, E. A., et al. 1998, *JQSRT*, 60, 883, doi: [10.1016/S0022-4073\(98\)00091-0](https://doi.org/10.1016/S0022-4073(98)00091-0)
- Pineau des Forets, G., Roueff, E., Schilke, P., & Flower, D. R. 1993, *MNRAS*, 262, 915, doi: [10.1093/mnras/262.4.915](https://doi.org/10.1093/mnras/262.4.915)
- Plume, R., Jaffe, D. T., & Evans, Neal J., I. 1992, *ApJS*, 78, 505, doi: [10.1086/191636](https://doi.org/10.1086/191636)
- Price-Whelan, A. M., Sipőcz, B. M., Günther, H. M., et al. 2018, *AJ*, 156, 123, doi: [10.3847/1538-3881/aabc4f](https://doi.org/10.3847/1538-3881/aabc4f)
- Purser, S. J. D., Lumsden, S. L., Hoare, M. G., et al. 2016, *MNRAS*, 460, 1039, doi: [10.1093/mnras/stw1027](https://doi.org/10.1093/mnras/stw1027)
- Qin, S.-L., Huang, M., Wu, Y., Xue, R., & Chen, S. 2008, *ApJL*, 686, L21, doi: [10.1086/592785](https://doi.org/10.1086/592785)
- Quénard, D., Jiménez-Serra, I., Viti, S., Holdship, J., & Coutens, A. 2018, *MNRAS*, 474, 2796, doi: [10.1093/mnras/stx2960](https://doi.org/10.1093/mnras/stx2960)
- Rodgers, S. D., & Charnley, S. B. 2003, *ApJ*, 585, 355, doi: [10.1086/345497](https://doi.org/10.1086/345497)
- Sanhueza, P., Jackson, J. M., Foster, J. B., et al. 2012, *ApJ*, 756, 60, doi: [10.1088/0004-637X/756/1/60](https://doi.org/10.1088/0004-637X/756/1/60)
- Sanna, A., Kölligan, A., Moscadelli, L., et al. 2019, *A&A*, 623, A77, doi: [10.1051/0004-6361/201833411](https://doi.org/10.1051/0004-6361/201833411)
- Saupe, S., Wappelhorst, M. H., Meyer, B., Urban, W., & Maki, A. G. 1996, *Journal of Molecular Spectroscopy*, 175, 190, doi: [10.1006/jmsp.1996.0021](https://doi.org/10.1006/jmsp.1996.0021)
- Schmid-Burgk, J., Muders, D., Müller, H. S. P., & Brupbacher-Gatehouse, B. 2004, *A&A*, 419, 949, doi: [10.1051/0004-6361:20035589](https://doi.org/10.1051/0004-6361:20035589)
- Schuller, F., Menten, K. M., Contreras, Y., et al. 2009, *A&A*, 504, 415, doi: [10.1051/0004-6361/200811568](https://doi.org/10.1051/0004-6361/200811568)
- Scibelli, S., Shirley, Y., Vasyunin, A., & Launhardt, R. 2021, *MNRAS*, 504, 5754, doi: [10.1093/mnras/stab1151](https://doi.org/10.1093/mnras/stab1151)
- Sewilo, M., Churchwell, E., Kurtz, S., Goss, W. M., & Hofner, P. 2004, *ApJ*, 605, 285, doi: [10.1086/382268](https://doi.org/10.1086/382268)
- . 2008, *ApJ*, 681, 350, doi: [10.1086/588422](https://doi.org/10.1086/588422)
- . 2011, *ApJS*, 194, 44, doi: [10.1088/0067-0049/194/2/44](https://doi.org/10.1088/0067-0049/194/2/44)
- Sollins, P. K., Zhang, Q., Keto, E., & Ho, P. T. P. 2005a, *ApJ*, 631, 399, doi: [10.1086/432503](https://doi.org/10.1086/432503)
- . 2005b, *ApJL*, 624, L49, doi: [10.1086/430270](https://doi.org/10.1086/430270)
- Tan, J. C., Beltrán, M. T., Caselli, P., et al. 2014, in *Protostars and Planets VI*, ed. H. Beuther, R. S. Klessen, C. P. Dullemond, & T. Henning, 149–172, doi: [10.2458/azu_uapress.9780816531240-ch007](https://doi.org/10.2458/azu_uapress.9780816531240-ch007)
- Taquet, V., Wirström, E. S., & Charnley, S. B. 2016, *ApJ*, 821, 46, doi: [10.3847/0004-637X/821/1/46](https://doi.org/10.3847/0004-637X/821/1/46)
- Teague, R., & Foreman-Mackey, D. 2018, *Research Notes of the American Astronomical Society*, 2, 173, doi: [10.3847/2515-5172/aae265](https://doi.org/10.3847/2515-5172/aae265)
- Tercero, B., Cuadrado, S., López, A., et al. 2018, *A&A*, 620, L6, doi: [10.1051/0004-6361/201834417](https://doi.org/10.1051/0004-6361/201834417)
- Thorwirth, S., Mueller, H. S. P., & Winnewisser, G. 2001, *Physical Chemistry Chemical Physics (Incorporating Faraday Transactions)*, 3, 1236, doi: [10.1039/B009743H](https://doi.org/10.1039/B009743H)
- Thorwirth, S., Müller, H. S. P., Lewen, F., et al. 2003, *ApJL*, 585, L163, doi: [10.1086/374327](https://doi.org/10.1086/374327)
- Thorwirth, S., Müller, H. S. P., & Winnewisser, G. 2000, *Journal of Molecular Spectroscopy*, 204, 133, doi: [10.1006/jmsp.2000.8209](https://doi.org/10.1006/jmsp.2000.8209)
- Tiemann, E. 1974, *Journal of Physical and Chemical Reference Data*, 3, 259, doi: [10.1063/1.3253141](https://doi.org/10.1063/1.3253141)
- . 1982, *Journal of Molecular Spectroscopy*, 91, 60, doi: [10.1016/0022-2852\(82\)90030-3](https://doi.org/10.1016/0022-2852(82)90030-3)
- Tinti, F., Bizzocchi, L., Degli Esposti, C., & Dore, L. 2007, *ApJL*, 669, L113, doi: [10.1086/523850](https://doi.org/10.1086/523850)
- Tobin, J. J., van't Hoff, M. L. R., Leemker, M., et al. 2023, *Nature*, 615, 227, doi: [10.1038/s41586-022-05676-z](https://doi.org/10.1038/s41586-022-05676-z)
- Tolonen, A. M., Koivusaari, M., Paso, R., et al. 1993, *Journal of Molecular Spectroscopy*, 160, 554, doi: [10.1006/jmsp.1993.1201](https://doi.org/10.1006/jmsp.1993.1201)
- Towner, A. P. M., Ginsburg, A., Dell'Ova, P., et al. 2024, *ApJ*, 960, 48, doi: [10.3847/1538-4357/ad0786](https://doi.org/10.3847/1538-4357/ad0786)
- Tursun, K., Henkel, C., Esimbek, J., et al. 2022, *A&A*, 658, A34, doi: [10.1051/0004-6361/202141937](https://doi.org/10.1051/0004-6361/202141937)
- van der Velden, E. 2020, *The Journal of Open Source Software*, 5, 2004, doi: [10.21105/joss.02004](https://doi.org/10.21105/joss.02004)

- van der Walt, S., Colbert, S. C., & Varoquaux, G. 2011, *Computing in Science and Engineering*, 13, 22, doi: [10.1109/MCSE.2011.37](https://doi.org/10.1109/MCSE.2011.37)
- van Dishoeck, E. F., Kristensen, L. E., Mottram, J. C., et al. 2021, *A&A*, 648, A24, doi: [10.1051/0004-6361/202039084](https://doi.org/10.1051/0004-6361/202039084)
- van Gelder, M. L., Tabone, B., Tychniec, L., et al. 2020, *A&A*, 639, A87, doi: [10.1051/0004-6361/202037758](https://doi.org/10.1051/0004-6361/202037758)
- van Gelder, M. L., Nazari, P., Tabone, B., et al. 2022, *A&A*, 662, A67, doi: [10.1051/0004-6361/202142769](https://doi.org/10.1051/0004-6361/202142769)
- van 't Hoff, M. L. R., Bergin, E. A., Jørgensen, J. K., & Blake, G. A. 2020, *ApJL*, 897, L38, doi: [10.3847/2041-8213/ab9f97](https://doi.org/10.3847/2041-8213/ab9f97)
- Vanek, M. D., Jennings, D. A., Wells, J. S., & Maki, A. G. 1989, *Journal of Molecular Spectroscopy*, 138, 79, doi: [10.1016/0022-2852\(89\)90100-8](https://doi.org/10.1016/0022-2852(89)90100-8)
- van't Hoff, M. L. R., Harsono, D., van Gelder, M. L., et al. 2022, *ApJ*, 924, 5, doi: [10.3847/1538-4357/ac3080](https://doi.org/10.3847/1538-4357/ac3080)
- Vastel, C., Ceccarelli, C., Lefloch, B., & Bachiller, R. 2014, *ApJL*, 795, L2, doi: [10.1088/2041-8205/795/1/L2](https://doi.org/10.1088/2041-8205/795/1/L2)
- Virtanen, P., Gommers, R., Oliphant, T. E., et al. 2020, *Nature Methods*, doi: <https://doi.org/10.1038/s41592-019-0686-2>
- Visser, R., Kristensen, L. E., Bruderer, S., et al. 2012, *A&A*, 537, A55, doi: [10.1051/0004-6361/201117109](https://doi.org/10.1051/0004-6361/201117109)
- Walsh, A. J., Burton, M. G., Hyland, A. R., & Robinson, G. 1998, *MNRAS*, 301, 640, doi: [10.1046/j.1365-8711.1998.02014.x](https://doi.org/10.1046/j.1365-8711.1998.02014.x)
- Walsh, A. J., Macdonald, G. H., Alvey, N. D. S., Burton, M. G., & Lee, J. K. 2003, *A&A*, 410, 597, doi: [10.1051/0004-6361:20031191](https://doi.org/10.1051/0004-6361:20031191)
- Watson, C., Araya, E., Sewilo, M., et al. 2003, *ApJ*, 587, 714, doi: [10.1086/368286](https://doi.org/10.1086/368286)
- Westerhout, G. 1958, *BAN*, 14, 215
- Wilkins, O. H., Carroll, P. B., & Blake, G. A. 2022, *ApJ*, 924, 4, doi: [10.3847/1538-4357/ac3132](https://doi.org/10.3847/1538-4357/ac3132)
- Wilson, T. L., & Rood, R. 1994, *ARA&A*, 32, 191, doi: [10.1146/annurev.aa.32.090194.001203](https://doi.org/10.1146/annurev.aa.32.090194.001203)
- Winnewisser, M., Winnewisser, B. P., Stein, M., et al. 2002, *Journal of Molecular Spectroscopy*, 216, 259, doi: [10.1006/jmbsp.2002.8590](https://doi.org/10.1006/jmbsp.2002.8590)
- Wood, D. O. S., & Churchwell, E. 1989, *ApJS*, 69, 831, doi: [10.1086/191329](https://doi.org/10.1086/191329)
- Wyrowski, F., Schilke, P., Walmsley, C. M., & Menten, K. M. 1999, *ApJL*, 514, L43, doi: [10.1086/311934](https://doi.org/10.1086/311934)
- Xu, J.-L., & Wang, J.-J. 2013, *MNRAS*, 431, 2385, doi: [10.1093/mnras/stt331](https://doi.org/10.1093/mnras/stt331)
- Xu, L.-H., & Lovas, F. J. 1997, *Journal of Physical and Chemical Reference Data*, 26, 17, doi: [10.1063/1.556005](https://doi.org/10.1063/1.556005)
- Xu, L.-H., Fisher, J., Lees, R. M., et al. 2008, *Journal of Molecular Spectroscopy*, 251, 305, doi: [10.1016/j.jms.2008.03.017](https://doi.org/10.1016/j.jms.2008.03.017)
- Xue, C., Remijan, A. J., Brogan, C. L., et al. 2019, *ApJ*, 882, 118, doi: [10.3847/1538-4357/ab32e0](https://doi.org/10.3847/1538-4357/ab32e0)
- Yamada, K. M. T., & Creswell, R. A. 1986, *Journal of Molecular Spectroscopy*, 116, 384, doi: [10.1016/0022-2852\(86\)90135-9](https://doi.org/10.1016/0022-2852(86)90135-9)
- Yan, Y. T., Henkel, C., Kobayashi, C., et al. 2023, *A&A*, 670, A98, doi: [10.1051/0004-6361/202244584](https://doi.org/10.1051/0004-6361/202244584)
- Yu, H. Z., Zhang, J. S., Henkel, C., et al. 2020, *ApJ*, 899, 145, doi: [10.3847/1538-4357/aba8f1](https://doi.org/10.3847/1538-4357/aba8f1)
- Zapata, L. A., Schmid-Burgk, J., & Menten, K. M. 2011, *A&A*, 529, A24, doi: [10.1051/0004-6361/201014423](https://doi.org/10.1051/0004-6361/201014423)
- Zhang, C.-P., Wang, J.-J., Xu, J.-L., Wyrowski, F., & Menten, K. M. 2014, *ApJ*, 784, 107, doi: [10.1088/0004-637X/784/2/107](https://doi.org/10.1088/0004-637X/784/2/107)